2015-08-01

Design, Fabrication, and Optimization of Miniaturized Devices for Bioanalytical Applications

Suresh Kumar
Brigham Young University

www.manaraa.com

Design, Fabrication, and Optimization of Miniaturized Devices

for Bioanalytical Applications

Suresh Kumar

A dissertation submitted to the faculty of
Brigham Young University
in partial fulfillment of the requirements for the degree of

Doctor of Philosophy

Adam T. Woolley, Chair
Milton L. Lee
Paul B. Farnsworth
Aaron R. Hawkins
Jaron C. Hansen

Department of Chemistry and Biochemistry

Brigham Young University

August 2015

ABSTRACT

Design, Fabrication, and Optimization of Miniaturized Devices
for Bioanalytical Applications

Suresh Kumar
Department of Chemistry and Biochemistry, BYU
Doctor of Philosophy

My dissertation work integrates the techniques of microfabrication, micro/nanofluidics, and bioanalytical chemistry to develop miniaturized devices for healthcare applications. Semiconductor processing techniques including photolithography, physical and chemical vapor deposition, and wet etching are used to build these devices in silicon and polymeric materials. On-chip micro-/nanochannels, pumps, and valves are used to manipulate the flow of fluid in these devices. Analytical techniques such as size-based filtration, solid-phase extraction (SPE), sample enrichment, on-chip labeling, microchip electrophoresis (μCE), and laser induced fluorescence (LIF) are utilized to analyze biomolecules. Such miniaturized devices offer the advantages of rapid analysis, low cost, and lab-on-a-chip scale integration that can potentially be used for point-of-care applications.

The first project involves construction of sieving devices on a silicon substrate, which can separate sub-100-nm biostructures based on their size. Devices consist of an array of 200 parallel nanochannels with a height step in each channel, an injection reservoir, and a waste reservoir. Height steps are used to sieve the protein mixture based on size as the protein solution flows through channels via capillary action. Proteins smaller than the height step reach the end of the channels while larger proteins stop at the height step, resulting in separation. A process is optimized to fabricate 10-100 nm tall channels with improved reliability and shorter fabrication time. Furthermore, a protocol is developed to reduce the electrostatic interaction between proteins and channel walls, which allows the study of size-selective trapping of five proteins in this system. The effects of protein size and concentration on protein trapping behavior are evaluated. A model is also developed to predict the trapping behavior of different size proteins in these devices. Additionally, the influence of buffer ionic strength, which can change the effective cross-sectional area of nanochannels and trapping of proteins at height steps, is explored in nanochannels. The ionic strength inversely correlates with electric double layer thickness. Overall, this work lays a foundation for developing nanofluidic-based sieving systems with potential applications in lipoprotein fractionation, protein aggregate studies in biopharmaceuticals, and protein preconcentration.

The second project focuses on designing and developing a microfluidic-based platform for preterm birth (PTB) diagnosis. PTB is a pregnancy complication that involves delivery before 37 weeks of gestation, and causes many newborn deaths and illnesses worldwide. Several serum PTB biomarkers have recently been identified, including three peptides and six proteins. To provide rapid analysis of these PTB biomarkers, an integrated SPE and μCE device is assembled that provides sample enrichment, on-chip labeling, and separation. The integrated device is a multi-layer structure consisting of polydimethylsiloxane valves with a peristaltic pump, and a porous polymer monolith in a thermoplastic layer. The valves and pump are fabricated using soft

lithography to enable pressure-based sample actuation, as an alternative to electrokinetic operation. Porous monolithic columns are synthesized in the SPE unit using UV photopolymerization of a mixture consisting of monomer, cross-linker, photoinitiator, and various porogens. The hydrophobic surface and porous structure of the monolith allow both protein retention and easy flow. I have optimized the conditions for ferritin retention, on-chip labelling, elution, and µCE in a pressure-actuated device. Overall functionality of the integrated device in terms of pressure-controlled flow, protein retention/elution, and on-chip labelling and separation is demonstrated using a PTB biomarker (ferritin). Moreover, I have developed a µCE protocol to separate four PTB biomarkers, including three peptides and one protein. In the future, an immunoaffinity extraction unit will be integrated with SPE and µCE to enable rapid, on-chip analysis of PTB biomarkers. This integrated system can be used to analyze other disease biomarkers as well.

ACKNOWLEDGEMENTS

I would like to express my sincere gratitude to all who have helped me in my doctoral study. First, I would like to thank my PhD adviser Dr. Adam T. Woolley, for his motivational, thought provoking, and consistent advice that helped me sail through the ocean of PhD research. Dr. Woolley is a very cheerful and encouraging mentor and I will always be obliged to him for shaping my career. I would also like to express my gratitude to all my PhD committee members, which include Dr. Milton Lee, Dr. Aaron Hawkins, Dr. Paul Farnsworth and Dr. Jaron Hansen, for their valuable scientific ideas. I would also like to express my appreciation to all staff and faculty members in the Department of Chemistry and Biochemistry at Brigham Young University (BYU). I would also like to thank Mr. Jim Fraser at the Integrated Microfabrication Laboratory, BYU for his help in solving fabrication issues.

I am also very thankful to my family and friends who have been a constant source of inspiration and support through all the ups and downs in my life. I also enjoyed working with all my colleagues including Dr. Jie Xuan, Dr. Vishal Sahore, Dr. Chad Rogers, Dr. Radim Knob, Dr. Elizabeth Gates, Dr. Jayson Pagaduan, John Stout, Mukul Sonker, Rui Yang, John Jensen, Anna Nielsen, Riley Mills, Mike Beauchamp, Kaitlyn Brower, Taylor Welker, and others. A special thanks is given to Dr. Vishal Sahore who has constantly shared his experience and knowledge during my research, job hunting, and dissertation writing. Last, but not the least, I would like to thank the National Institutes of Health for the generous funding of this work.

TABLE OF CONTENTS

LIST OF FIGURES

LIST OF TABLES

1. INTRODUCTION

1.1 BIOMARKERS AND BIOANALYTICAL METHODS

Human disease is defined as disordered or abnormal functioning of cells, organs, or systems in the body.[1] Disease diagnosis at the right time is important so that an effective treatment can be provided. In old times, disease diagnosis mostly involved observation of abnormal physical symptoms such as body color, smell, temperature and locomotive movements.[2] This diagnostic method was generally non-specific and diagnosed diseases in late stages. Therefore, alternative approaches to diagnose diseases at an early stage have been investigated. Advancements in the fields of genomics, pathology and proteomics have enabled identification of many health- and disease-related biochemical entities at the molecular or cellular level.[3-4] Such biochemical entities are called biomarkers[5-6] and their absence, presence or concentration can indicate a normal or abnormal condition.[7-8] It is helpful to study the concentrations of biomarkers to predict individuals with a risk of developing a particular disease. In addition, the study of biomarkers should lead to better management and treatment of diseases.

Biomarkers can be in the form of peptides, proteins, carbohydrates, nucleic acids and metabolites.[9-11] There are many examples of biomarkers linked to human diseases. For example, aberrantly expressed microRNAs in pancreatic adenocarcinoma tissue can be found in the plasma as biomarkers for early detection of this malignancy.[12] Isolation and quantification of four microRNAs, miR-21, miR-210, miR-155, and miR-196a, in heparin treated blood can differentiate between patients and healthy controls. Among these, miR-155 has been identified as a candidate biomarker of early pancreatic neoplasia. Another example includes amyloid-β1–42 peptide, t-tau, and p-tau181p which are biomarkers of Alzheimer's disease (AD).[13] These three biomarkers are found altered in cerebrospinal fluid (CSF) when mild AD is present. In mild AD cases, amyloid-

β1–42 peptide has been found to decrease in CSF, whereas an increase in t-tau and p-tau181p is reported. Typically, definitive AD is diagnosed with an autopsy, but presymptomatic mild AD can only be diagnosed with biomarkers.[14-15] It is believed that full-blown AD develops over a 20 year period,[16] but it is difficult to diagnose it at an early stage without biomarkers that signal the onset of disease. Likewise, serum concentration levels of three peptides and six proteins (corticotropin-releasing factor, defensin, ferritin, lactoferrin, thrombin antithrombin complex, and tumor necrosis factor-α receptor type 1) are altered in preterm birth (PTB) cases.[17] Three specific peptides formed by breakdown of inter-alpha-trypsin inhibitor heavy chain 4 protein are significantly reduced in women several weeks prior to PTB.[17] A panel of these nine PTB biomarkers can be analyzed for early diagnosis of PTB so that an effective therapeutic intervention can be provided to delay the delivery. Moreover, lipoproteins help in the transportation and storage of cholesterol in the human body; and high cholesterol levels are correlated with the progression of cardiovascular diseases.[18] Ratios of low-density lipoprotein and high-density lipoprotein can be assessed to evaluate the risk of cardiovascular disease.[19-20] Furthermore, elevated levels of alpha-fetoprotein in serum are correlated to hepatocellular carcinoma.[21-22] Similarly, heat shock protein 90 is related to many cancers and its inhibition can be helpful in cancer therapeutics.[23-24]

An ideal biomarker should be easy to detect and quantify non-invasively with good specificity and sensitivity.[25] Although the use of a single biomarker as a disease indicator is convenient, it often results in low sensitivity. For instance, a single peptide (qlglpgppdvpdhaayhpf) can be used to diagnose PTB, but offers less than optimal sensitivity (65.0%). However, when this peptide is used in combination with other biomarkers, the sensitivity is increased to 86.5%, with little change in specificity.[17] Therefore, a panel of biomarkers in disease diagnosis can often improve the reliability of results. In most cases, biomarker concentration levels are in the μg/mL-

pg/mL range;[26] therefore, either a very sensitive method is required or biomarkers should be preconcentrated before analysis.

There are many methods such as liquid chromatography-mass spectrometry (LC-MS),[27] immunoassays,[28] and lab-on-a-chip (LOC)[29-30] technologies that can be used to analyze biomarkers. LC-MS is a very powerful technique used for initial identification of biomarkers. It uses liquid chromatography to separate complex analyte mixtures into individual components and mass spectrometry to distinguish analytes based on their mass-to-charge ratios. Advantages of LC-MS include the ability to analyze hundreds of analytes in complex biological fluids like serum, plasma and urine.[31] However, LC-MS is not a method of choice for routine biomarker analysis, as it lacks the potential for point-of-care diagnosis owing to instrument size and operational complexity. Moreover, LC-MS generates complex data and requires experienced personnel to perform the analysis.

Enzyme linked immunosorbent assay (ELISA)[32] is a plate-based immunoassay commonly used in clinical laboratories for analysis of protein biomarkers in solution. Briefly, the target molecule is immobilized on an adsorbent surface in a 96-well plate and complexed with an enzyme linked antibody. Enzyme reaction with a substrate produces measurable signal. In the past, radioimmunoassay was commonly used to estimate the concentration of target.[33] Later, it was replaced with colorimetric methods because radioactivity poses health risks. In a colorimetric assay, an enzyme, horseradish peroxidase or alkaline phosphatase, reacts with 5-aminosalicylic acid or phenolphthalein monophosphate, respectively, to produce a colored product.[34] However, other detection methods like fluorescence are also used.[35] ELISA can be performed in four formats: direct, indirect, sandwich, and competitive.[36] Sandwich ELISA is the most common format because it is robust and sensitive. In this assay, the target molecule is sandwiched between two

primary antibodies, one of which has an enzyme that reacts with a substrate to produce a colored signal. ELISA analysis requires expensive reagents like monoclonal antibodies, and is most cost effective if all wells in the assay plate are used.[37] Moreover, ELISA's sensitivity to peptides is low. Therefore, there is still a need for analytical techniques that can provide fast and sensitive analysis of a range of biomarkers at reasonable cost.

LOC is a rapidly growing application of microfluidics in bioanalytical research.[38-40] LOC systems use micro-to-nanoscale fabricated channels, and employ small volumes of fluids. All essential components required for an analysis are integrated on a small device. Such components can be of electrical, mechanical, optical or chemical origin.[41] The advantages of LOC systems include automation, portability, rapid analysis, and potential for point-of-care usage. Many processes such as sample preparation, chemical reaction, product isolation, fluid handling, analytical separation, and detection are performed with automation on a single chip.[42] LOC is a possible alternative to ELISA because it can prepare samples on-chip with short analysis times.

1.2 NANOFLUIDICS

1.2.1 Overview

Nanofluidics deals with manipulation and study of fluids confined in sub-100-nm structures.[43] Recently, nanofluidics has attracted significant attention in the study of ions, particles, and biostructures in small dimensions like nanochannels, nanopores, and nanopipets.[44] Nanofluidics is still in its infancy, but it is a rapidly growing research area due to novel nanoscale phenomena.[45] Developments in the microelectronic industry, especially in micro and nanofabrication, have further encouraged interest and progress in nanofluidics.[46] Nanofluidics has potential for application in various fields like electronics, mechanics, separation science, etc.[47-48]

For example in separation science, promising results in pre-concentration and separation of nucleic acids have been obtained using nanocapillaries with diameters of hundreds of nanometers.[49-50] Moreover, there are numerous biomolecules which have sizes in the sub-100-nm range, such as proteins, lipoproteins, nucleic acids, and viruses. These biostructures are often related to various human diseases. For example, hepatitis B virus causes liver disease,[51] and the concentration distribution of LDL/HDL is related to cardiovascular disease.[20] Therefore, it could be helpful to study these biomolecules using nanofluidics, which offers dimensions comparable to the sizes of these biostructures.

Nanofluidics exhibits many characteristics, which make it different from bulk fluidics; for example, nanofluidic channel dimensions (1-100 nm) are comparable to the sizes of many biostructures (proteins, nucleic acids, and lipoproteins) and the electric double layer (EDL) thickness (1-100 nm).[52] Such a close correlation in dimensions and EDL in nanochannels can significantly affect ion, particle and fluid transport. Two important nanofluidic characteristics useful in my studies are capillary action and EDL.

Similar to the microscale, the forces generated by the curvature of a liquid meniscus in a nanochannel produce capillary action. The meniscus velocity produced by capillary action in rectangular nanochannels is given in equation (1.1) below,[53]

$$\nu \approx \frac{d\gamma\cos\Phi}{4l\eta} \tag{1.1}$$

where ν is the meniscus velocity, d is the height of the rectangular channel, γ is the surface tension of the liquid, Φ is the dynamic contact angle between the liquid meniscus and the vapor phase, l is the distance between meniscus and the channel inlet, and η is the liquid viscosity. Capillary action is a spontaneous phenomenon that allows the filling of nanochannels and analyte transport, eliminating the need for external voltage or pressure controllers.

An EDL structure is formed when a surface is exposed to ionic species in solution. For example, silicon surfaces have weakly acidic silanol groups, which are negatively charged in basic conditions. This results in accumulation of some positively charged species at the silicon surface. These positively charged species form a fixed layer closer to the surface and a movable diffuse layer next to the fixed layer. These two layers constitute together the EDL, with a characteristic thickness given by the Debye length (κ^{-1}).[54] The thickness of the Debye length varies from 1 to 100 nm depending on the concentration of the ionic species in solution as given in equation (1.2) below,

$$\kappa^{-1} = [\varepsilon_r \varepsilon_0 RT/2F^2 C_0]^{1/2} \qquad (1.2)$$

where ε_r is the dielectric constant, ε_0 is the permittivity of free space, R is the gas constant, T is the absolute temperature in Kelvin, F is the Faraday constant, and C_0 is the molar concentration of the electrolyte. The effects of EDL become prominent in nanochannels due to comparable dimensions. For example, in nanochannels having at least one dimension in the 5-100 nm range, the EDL on opposite walls can overlap and affect the transport of analytes by changing the effective opening size of the nanochannel or ion concentration polarization.[55-56]

1.2.2 Materials and nanochannel fabrication methods

Many factors need to be considered in choosing a fabrication material for nanochannels, for example, cost; ease of fabrication; and surface, optical, and mechanical properties. To date, a wide range of materials has been explored for nanochannel fabrication including inorganic (silicon, glass and quartz) and organic [polydimethylsiloxane (PDMS), polymethylmethacrylate (PMMA), and polycarbonate (PC)].[52]

Among these materials, silicon is the most common substrate on which nanochannels are fabricated owing to well-developed fabrication techniques and reasonable cost. However, silicon

is not transparent to visible light, which makes visual observation of fluid impossible. Other than silicon, glass and quartz are also used to make nanochannels due to their optical clarity and electrical insulation.[57-58] Furthermore, the nanochannel wall material is also important. Nanochannel walls can be formed with silicon dioxide, silicon nitride, or other materials deposited using chemical or physical vapor deposition.[59-60] The nature of the wall material results in different surface properties like charge, electrical insulation, hydrophobicity/hydrophilicity, roughness, and biocompatibility.[52] Such properties are important as they affect the transport of fluids and particles through the nanochannels. Unlike silicon, organic materials such as PDMS, PMMA, and PC are less common for nanochannel fabrication, but they are increasingly being considered owing to low material and fabrication cost and optical transparency.[61]

Nanochannel fabrication is usually performed in a clean room facility because particles can block nanochannels and can cause problems in substrate bonding.[62] Nanochannel fabrication can be categorized as either top-down or bottom-up;[63] I will first describe top-down in the following paragraphs, followed by bottom-up. Top-down methods involve reducing large-scale patterns into small structures and can be divided into three categories: bulk/film nanomachining, surface nanomachining, and mold machining.

In bulk/film nanomachining, structures are created either by etching trenches in the bulk of a substrate or a film deposited on a substrate.[64] It uses standard photolithography to define structures on the substrate, followed by wet or dry etching. Reactive ion etching is a common dry etch method, and produces vertical sidewalls.[65] Moreover, anisotropic wet etching using aqueous KOH or tetramethylammonium hydroxide can produce smooth vertical walls;[66] but it requires the correct crystal oriented substrate.[67] Next, the prepared structures are sealed by bonding to another flat substrate. Thermal and anodic bonding processes are commonly used for enclosing

nanochannels,[68] but their effectiveness is affected by particle contamination. Bulk/film nanomachining can suffer from channel collapse while performing the bonding step,[63] but this can be avoided by proper selection of channel geometry, wafer thickness, substrate hardness, and adhesion surface energy.[62]

The second top-down fabrication technique uses sacrificial layers to define nanochannel structures;[69] the sacrificial layers are then dissolved to form hollow nanochannels. Briefly, surface nanomachining involves deposition of a bottom layer and sacrificial material.[70] After this, patterning of the sacrificial layer using UV photolithography and wet/dry etching occurs. Resulting structures are covered with a top capping layer (often silicon dioxide), and the top layer is patterned to access the sacrificial material during etching. Finally, the sacrificial material is etched and results in hollow nanochannels. Sacrificial materials commonly used are polysilicon, amorphous silicon, and metals.[71-73] This method has drawbacks in that part of the capping layer needs to be removed to access the sacrificial layer and etching of the sacrificial layer takes a long time (1-3 days). However, this process produces uniform height nanochannels, because the channel height is defined by the thickness of the sacrificial layer.[74]

In mold-machining or nanoimprint lithography, a master mold is prepared by either patterning of layers of photoresist using photolithography or electron beam lithography or using a focused ion beam to pattern Si directly.[75-76] The master mold is used to transfer features into a material.[77] The mold can be either directly pressed against a material like PMMA or a thin resist film coated on a Si substrate to duplicate mold features, which are transferred by heating the material close to its glass transition temperature.[78-79] Alternatively, a mixture of monomer and curing agent can be poured onto a mold, cured, and then peeled off.[76] Mold machining is a high

throughput technique with low fabrication cost, and capability of producing smooth and vertical sidewalls.

Bottom-up fabrication is a new approach that is being explored for nanochannel fabrication. In the bottom-up method, atoms and molecules are assembled to make nanostructures by atomic layer deposition, molecular self-assembly, sol-gel nanofabrication, or DNA-scaffolding.[80] This method has potential to make small structures (2-10 nm) with low reagent consumption and minimal requirement of semiconductor-processing instruments.[63, 81] On the other hand, challenges include control of assembly, surface preparation, and requirement of ultra-pure reagents.[80] Min et al.[82] used a ~1 nm wide graphene nanoribbon fabricated by a bottom-up approach to build a nanochannel in Si_3N_4, which was used for fast DNA sequencing.

1.2.3 Size-based separations in nanochannels

So far, much of the nanofluidics research has focused on fundamental studies,[45] because phenomena at the nanoscale are not yet well understood. However, many scientists have been successful in designing nanostructures to separate biomolecules based on their size, charge or length.[83] Size- and length-based separations are common because of their dimensional overlap with nanofluidic structures. Nanofluidics have been used to study nucleic acid separations in particular. Han et al.[50] fabricated nanofluidic channels consisting of alternating deep and shallow regions to separate long DNA. The molecules changed their conformations while passing through the thin and thick regions as an electric field was applied across the channel length. The mobility of long DNA molecules in the shallow regions was greater than short DNAs due to a favorable entropic contribution. This created electrophoretic mobility differences, and resulted in efficient separation of DNA molecules without the need of a gel matrix. In 2006, Fu et al.[84] published a study presenting Ogston-like sieving of rodlike DNA molecules in periodic nanofluidic filter

arrays. DNA molecules have been also fractionated by applying forward and reverse bias asymmetric voltage pulses across the nanochannel length.[85] There are few studies on separation of proteins in nanofluidic channels, as fabrication of nanochannel dimensions comparable to protein sizes (1-20 nm) is challenging and channels are susceptible to clogging. Zeng et al.[86] fabricated an ordered, 3D nanofluidic sieve in a microchannel using colloidal self-assembly, which allowed separation of a wide range of proteins (20-200 kDa) and dsDNA (0.05-50 kbp) by Ogston-like sieving and entropic traps, respectively. Inglis et al.[87] demonstrated the separation of R-phycoerythrin (240 kDa) and streptavidin (54 kDa) in silica-based nanochannels by concentration gradient focusing. All the studies described above used voltage to drive biomolecules through sieving channels. Moreover, the sieve size was not precisely controlled, especially for protein separation. In this dissertation, I describe fabrication of sieving nanochannels in which sieve openings in the 10-100 nm range can be defined accurately. Protein molecules are driven into nanochannels by capillary flow, which causes size-based separation at the constrictions in the nanochannels.

1.3 MICROFLUIDICS

1.3.1 Overview

Microfluidics deals with the study and manipulation of fluids in microfabricated structures with a few to hundreds of micrometer dimensions.[88] First, I present a brief history of microfluidic-based system developments. In the 1970s, the first microfabricated device in a silicon wafer was used for gas chromatography.[89] Despite the fact that the miniaturized gas chromatograph could separate simple compound mixtures in a few seconds, it did not get much attention from the separation science community until years later. In 1990, a liquid chromatograph was fabricated on a silicon wafer although it was not demonstrated for actual separations.[90] At that time, Manz et

al.[91] also coined the term micro total analysis system (μTAS), or a setup capable of performing all sample handling steps extremely close to the place of measurement. An early attempt at a μTAS in 1992 used microfabricated glass devices to perform sample injection through electroosmotic pumping and electrophoretic separation on a microchip.[92] The number of papers published on miniaturized devices abruptly increased in 1994 as many groups joined in microfluidic research.[93] Since then, microfluidics research has continued growing, and more complex processes such as sample extraction, filtration, derivatization, alternative separation, and detection schemes have been incorporated in miniaturized devices.

Microfluidic systems are the result of combining concepts from multiple disciplines like chemistry, physics, and engineering on the same platform. Microfluidics are used in both chemical and biological analysis, and offer many advantages. For example, very small quantities of sample and reagents are required; and device size is small, which reduces fabrication cost, offers portability for field applications, and reduces diffusion distances, resulting in better mixing.[94] Moreover, many laboratory processes can be integrated on a single device to provide complete analysis in a μTAS.[95] Integrated processes include sample preparation, fluid flow control through pumps and valves, sample mixers, and detection.[96-98] Fluid transport in microfluidic devices can be accomplished using either voltage or pressure.[99] The electrokinetic approach is more common because of simple operation, but it also suffers from inherent limitations including charge bias, bubble formation, and reliance on channel wall and buffer properties. Thus, pressure-based controllers have been developed that use external or on-chip pumps and valves.

1.3.2 Materials

Broadly, microfluidic device fabrication materials can be divided into three categories: inorganic, polymeric, and paper;[38] here, I will focus only on the first two. The initial microfluidic devices were fabricated in silicon due to the well-established methods for silicon processing. Glass was also used early on because of its similar surface chemistry to silicon. Later, many polymer-based materials were explored to make microfluidic devices. The selection of material is important in determining the cost as well as the operational performance of the device. Usually, three important factors including required function, scale of integration, and application are considered in choosing the device material. Some of the material properties like flexibility, air permeability, solvent compatibility, optical clarity, non-specific adsorption, and compatibility with fabrication methods are critical in selection of a material.

Many materials have been developed to make microfluidic devices at low cost, with simple fabrication, and good reliability. Silicon and glass are the main inorganic materials used in microfabrication of microfluidic devices. Due to the semiconductor properties of silicon, it allows integration of electrical circuitry in making a μTAS. However, the semiconducting nature of silicon makes electrokinetic operations problematic due to leakage of current. Moreover, silicon is not transparent to visible light, which makes fluid imaging and fluorescence detection challenging in all-silicon devices. Silicon has surface silanol groups (Si-OH) which allow tailoring of surface chemistry using silanes. Glass offers similar surface chemistry to silicon, transparency to visible light, and compatibility with biological samples. Silicon and glass are both gas impermeable and rather inflexible, so they cannot be used to make flow controllers like valves and pumps. However, they can be used in hybrid devices along with polymers to overcome some of these limitations.

Polymers are replacing silicon and glass as microfluidic device fabrication materials owing to their amenable properties. For example, polymers are usually optically transparent, moldable, inexpensive, and good for mass production. Polymer materials are divided into thermoplastic and elastomeric types. Thermoplastic polymers can be molded or embossed above their glass transition temperatures, and then retain patterns when cooled down; they offer the advantages of easy micromachining, impermeability to gases, and optical transparency.[100] Some commonly used thermoplastics include PMMA, cyclic olefin copolymer (COC), PC, and polystyrene (PS). PMMA is a common device fabrication material that has a low glass transition temperature (~105 ºC) which allows easy hot embossing and injection molding. Moreover, PMMA is optically clear, impermeable to gas and small molecules, and biocompatible.[101] COC offers a low glass transition temperature (~90 ºC), optical clarity, and compatibility with organic solvents;[102] however, COC's surface is hydrophobic and requires modification for protein analysis. Thermoplastics are relatively rigid and therefore not useful to make on-chip valves and pumps.

On the other hand, elastomers are flexible and capable of forming pneumatic valves and pumps, which make their use in integrated devices plausible. PDMS is the most common elastomeric polymer and is widely used for making microdevices.[94, 103] PDMS offers gas permeability, optical transparency, and rapid fabrication. The gas permeability of PDMS enables its use in making devices for cell analysis. Moreover, the flexibility of PDMS has been used to make pneumatic valves and membrane-based pumps to allow pressure-actuated fluid handling. PDMS-based microchannels are hydrophobic, and suffer from non-specific adsorption and bubble formation. However, there are methods such as oxygen plasma treatment and surface coatings to reduce hydrophobicity and non-specific adsorption in PDMS devices.[104]

13

1.3.3 Fabrication methods

Microfluidic devices are fabricated using a variety of methods including photolithography, wet/dry etching, laser ablation, micromachining, replica molding, hot embossing, and injection molding.[105-106] A fabrication method is selected based on cost, speed, material properties, critical dimensions, and instrument availability. Broadly, device fabrication can be divided into additive and subtractive methods. In additive methods, microstructures are created on the surface of the material, whereas subtractive methods involve formation of structures within the material.

Silicon and glass devices are mostly fabricated in a cleanroom facility using techniques from the microelectronics industry, such as photolithography, wet and dry etching, and thin film deposition. In photolithography, a mask pattern is transferred to a light-sensitive photoresist coated on a substrate by exposing selected areas to UV light. The exposed areas either become soluble or insoluble in resist developers based on the type of resist used, as shown in Figure 1.1. Features are created on the substrate by wet or dry etching of uncovered areas. Then, the patterned features are bonded to a flat substrate to form enclosed channels.
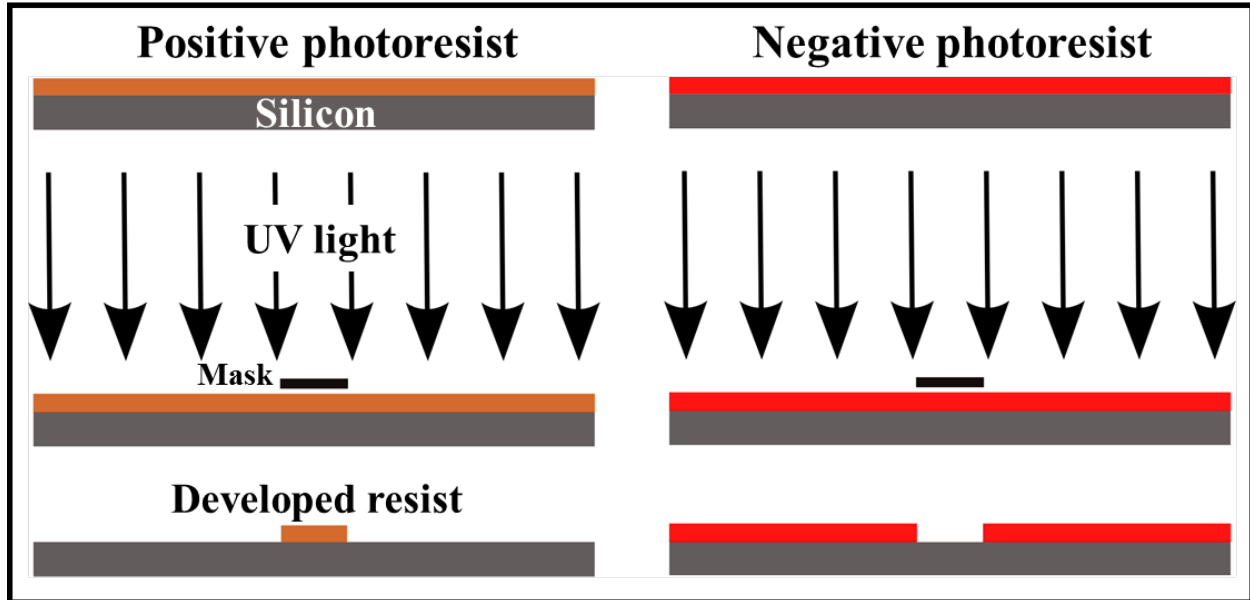
Figure 1.1 Schematic showing UV photolithography on a silicon wafer coated with (left) positive and (right) negative photoresist.

In other cases, structures formed on a substrate as described above or on a patterned photoresist layer can be used as a master mold to create features in polymers by soft lithography or hot embossing.[107] Casting elastomeric materials like PDMS by replica molding involves pouring a mixture of PDMS monomer and cross linker directly onto the master mold (see Figure 1.2). Next, the PDMS mixture is thermally cured to duplicate mold features into the polymer. The cured PDMS is peeled off and bonded reversibly or irreversibly to another PDMS, glass, thermoplastic or silicon substrate to form enclosed microchannels. Moreover, multiple layers of PDMS can be stacked or bonded to make complex 3D devices with multiple functions.
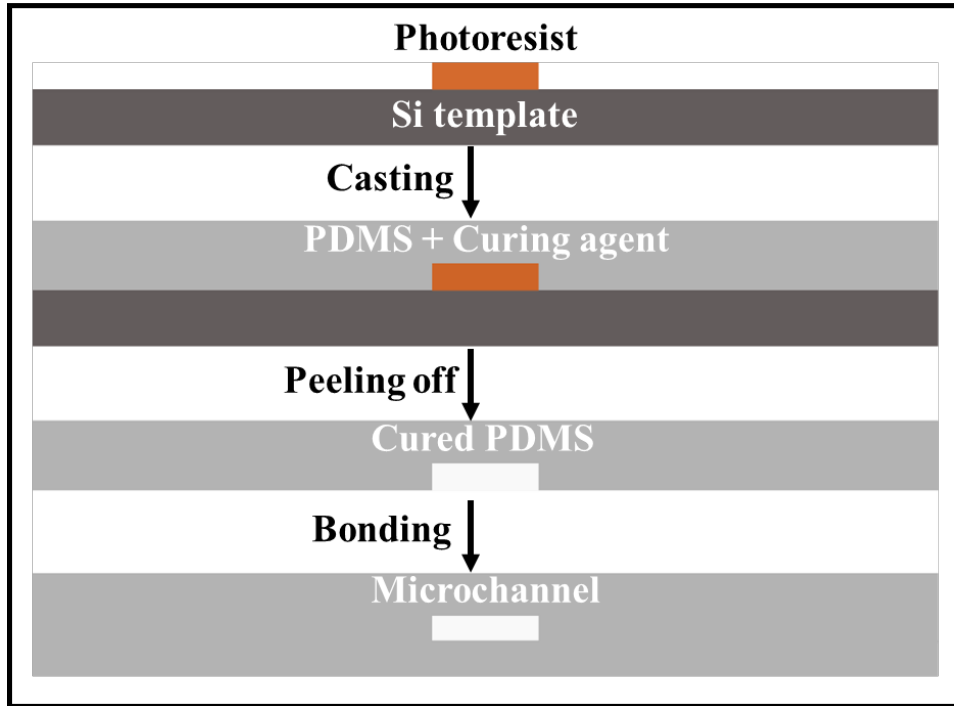
Figure 1.2 Schematic showing fabrication of a microchannel in PDMS by replica molding.

In hot embossing (see Figure 1.3), a flat thermoplastic material is pressed against a patterned substrate (silicon or metal), and the assembly is heated above the glass transition temperature of the polymer.[108] This results in transfer of substrate features into the polymer; then, the imprinted polymer is bonded to a flat substrate using heat, solvent or adhesives. Hot embossing is a straightforward and inexpensive method to make microdevices.
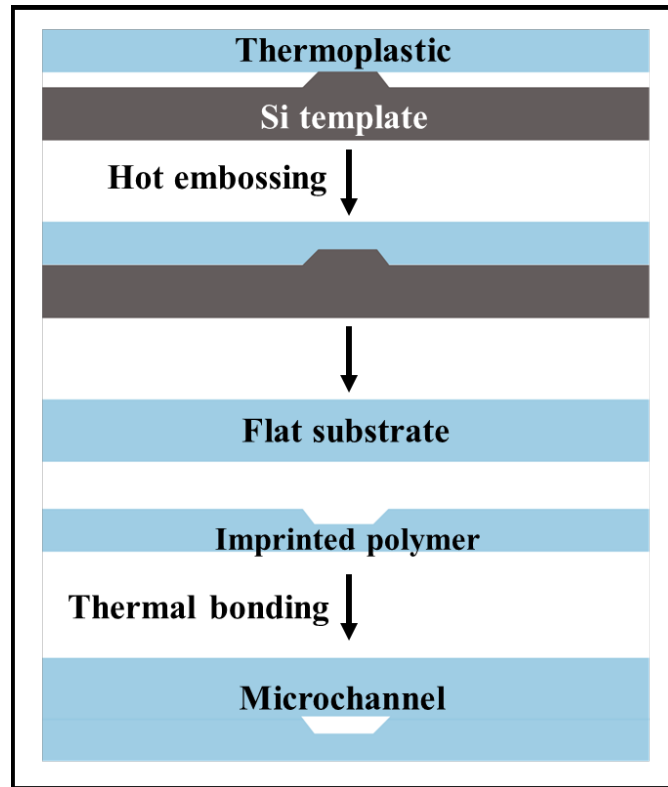
Figure 1.3 Schematic showing hot embossing and thermal bonding processes to form a microchannel in a thermoplastic polymer.

1.3.4 Pumps and valves

There is a wide range of mechanisms that can be used to manipulate fluid in microchannels; for example, capillary action, electroosmotic flow (EOF), vacuum, external pumps, membrane-actuated pumps, electrohydrodynamic pumps, and magnetohydrodynamic pumps.[38, 105] External pumps or vacuum have been used in many studies, but they require larger off-chip hardware, which is contrary to the goal of miniaturization. An electroosmotic pump (EOP) is a non-mechanical pump, driving fluid using EOF generated by the interaction of the electric field and EDL.[109] EOPs are easy to integrate on-chip and produce constant flow rates. Moreover, fluid velocity and direction can be manipulated by adjusting the voltage and polarity. However, EOPs can be only used for conductive liquids in narrow (<100 μm) channels, and surface adsorption, Joule heating

and bubble formation affect pump performance. In a membrane-actuated pump, liquid is displaced in pulses by sequential actuation of pneumatic valves placed in series, as shown in Figure 1.4.[110] Membrane-actuated pumps allow easy control over flow rate and direction by adjusting the valve actuation frequency and sequence, respectively. However, the downside is that membrane-actuated pumps require external connections and off-chip hardware.
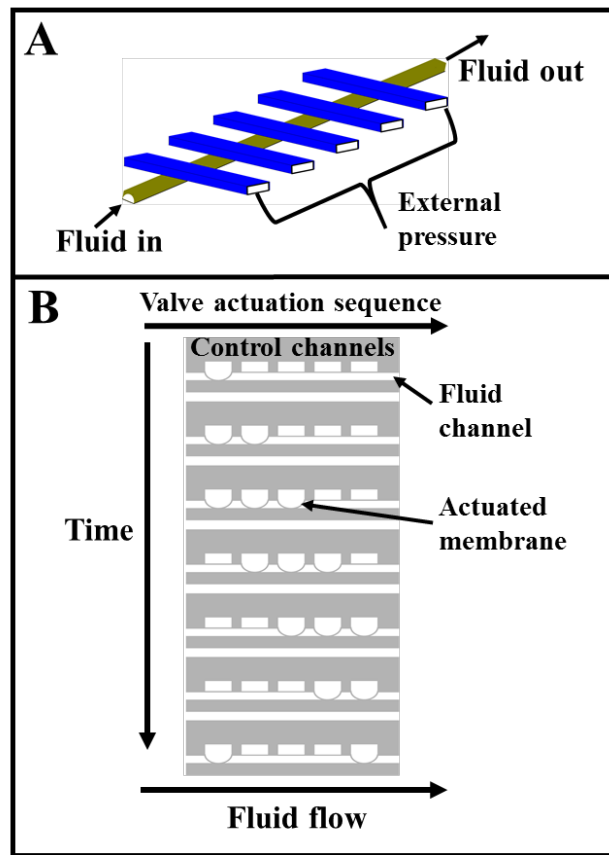
Figure 1.4 Schematic of a membrane-actuated peristaltic pump. (A) Top-view of a five-valve pump in the unactuated state. (B) Cross-sectional side-view of a five-valve pump showing the sequence of valve actuation over the course of time.

Furthermore, liquid flow through microchannels can be controlled or confined using on-chip valves. There are many types of microfluidic valves like pneumatic, piezoelectric, magnetic, shape-memory alloy, and check valves.[38, 111] PDMS is the most common material used for making

on-chip pneumatic valves owing to its elastic nature.[112] Pneumatic valves are widely used due to easy integration and simple actuation mechanism.[113] However, they require external pneumatic controllers like solenoids for their operation.

1.3.5 Microchip electrophoresis

Microchip electrophoresis (μCE) is a miniaturized version of capillary electrophoresis, offering several advantages such as lower reagent consumption, speed, and ability of integration with other processes on-chip.[114-115] Capillary and μCE separate analytes based on their migration in an electric field. Analytes acquire a velocity in an electric field based on equation (1.3),

$$v = \mu_e E \tag{1.3}$$

where v is the migration velocity, μ_e is the electrophoretic mobility, and E is the applied electric field. An ionic analyte in solution reaches a steady state velocity when the accelerating force (equation 1.4) is balanced with the frictional force (equation 1.5),

$$F_a = qE \tag{1.4}$$

$$F_f = 6\pi\eta r v \tag{1.5}$$

where q is the analyte charge, η is the viscosity, and r is the hydrodynamic radius of the analyte. Under steady state, combining equations (1.3), (1.4), and (1.5),

$$\mu_e = q/6\pi\eta r \tag{1.6}$$

indicating that at constant solution viscosity the electrophoretic mobility depends on analyte charge and radius. According to equation (1.6), smaller molecules or ones with higher charge move faster than larger molecules or ones with lower charge, which results in separation.

Movement of analyte is not only governed by electrophoretic mobility but also by EOF, or the movement of bulk fluid under an electric field. Typically, the surfaces of microchannels and capillaries carry a negative charge, and to counter-balance this charge, positive ions from the solution align on the surface and form an EDL. Under an applied voltage, the cations near the channel wall move towards the cathode and carry the water of hydration with them. This results in bulk flow towards the cathode, called EOF. The electroosmotic mobility (μ_{eo}) is given in equation (1.7) below,

$$\mu_{eo} = \frac{\varepsilon\zeta}{4\pi\eta} \tag{1.7}$$

where ε is the dielectric constant, and ζ is the zeta potential. The electroosmotic mobility is inversely proportional to the viscosity of the medium and directly proportional to the zeta potential. Thus, EOF can be reduced by coating the capillary wall to decrease the zeta potential and increase the surface viscosity. The apparent mobility (μ_{app}) of an analyte is a combination of the electrophoretic and electroosmotic mobilities as shown in equation (1.8).

$$\mu_{app} = \mu_{ep} + \mu_{eo} \tag{1.8}$$

Combining equation (1.3) and (1.8), the apparent migration velocity (v_{app}) of an analyte is given by equation (1.9).

$$v_{app} = \mu_{app}E \tag{1.9}$$

As a result of typical EOF, neutral analytes move in the same direction and with the same velocity as the EOF. The mobility of cations is increased due to EOF in the same direction, while the mobility of anions is reduced due to opposing EOF.

In μCE, device operation involves three steps: sample injection, electrophoretic separation, and detection. Sample injection is generally performed by electrokinetic flow.[116] The most common electrokinetic injection modes are floated, pinched and gated injections.[98, 117] Pinched injection allows loading of small volumes of samples defined by the intersection geometry. Cross-shaped or double-T-shaped geometries are common and shown in Figure 1.5.[115] Briefly, voltage is applied between reservoirs 1 and 2 while keeping reservoirs 3 and 4 at ground. For separation, voltages are reconfigured to pinch a small sample plug at the channel intersection for separation by applying high voltage at reservoir 4; small pull back voltages on reservoirs 1 and 2; and ground voltage at reservoir 3. Pinched is the most common type of injection, but requires injection times that can be as long as the separation times (10-150 s). Pinched injection has been further refined using narrow channels at the intersection for improved resolution.[118] All electrokinetic injection methods have the drawback of sample mobility bias caused by the injection voltage. Hence, the least charged and largest molecules are under-injected compared to the most charged and smallest molecules.
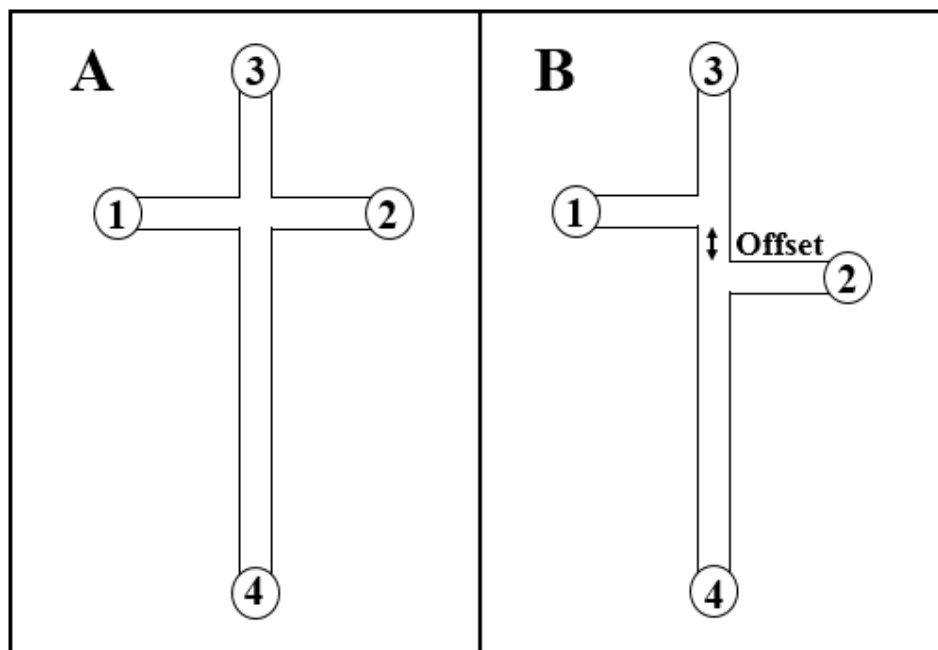
Figure 1.5 Sample injection geometries in µCE. (A) Cross-shape and, (B) double T-shape. Reservoirs are 1: sample, 2: sample waste, 3: running buffer, 4: separation waste.

1.3.6 Detection

In µCE, various detection modes have been used such as optical, electrochemical, and mass spectrometry.[38, 105] Optical methods are the most common because they provide detection limits comparable to mass spectrometry and can be carried out with the simplest device designs. Among optical methods, fluorescence, chemiluminescence and UV absorbance are popular.[119] Laser-induced fluorescence (LIF) is widely used owing to its detection limits. However, a drawback of LIF is that, in most cases, it requires derivatization of analytes with dyes such as fluorescein. Figure 1.6 shows a schematic of an LIF detection setup. LIF systems include a laser, focusing and wavelength selection optics, a photomultiplier tube (PMT) or charged-coupled device (CCD) to record fluorescence, and other hardware including a microscope, computer, etc. Chemiluminescence does not require an external light source because it utilizes light emitted from

a chemical reaction between molecules. UV absorbance is label-free and used in conventional electrophoresis, but its detection limits are far higher (µg/mL) than for LIF or chemiluminescence.
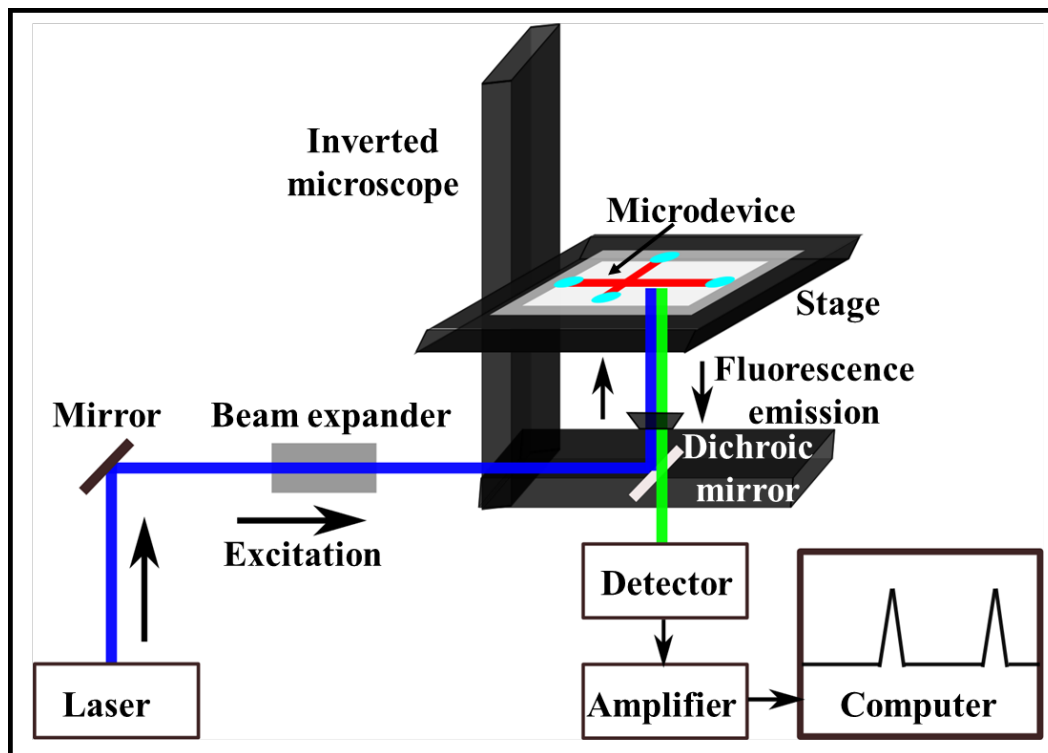
Figure 1.6 Schematic showing an LIF detection system.

1.4 SAMPLE PREPARATION

Good sample preparation is at the heart of any chemical analysis. For example, sample preparation can involve filtration, purification, preconcentration and derivatization.[38] These benchtop methods can be time consuming, solvent-intensive, and sample-inefficient. Microfluidics offers the potential of integrating sample preparation procedures on a single device.[99, 120-122] Such integration allows automation, rapid analysis, and small sample and reagent consumption.

1.4.1 Extraction and purification

Liquid-liquid and solid phase extraction (SPE) are common techniques used to remove desired analyte from the sample matrix. Liquid-liquid extraction involves transfer of analyte from one solvent to another based on solubility and is widely used to prepare food and environmental samples.[123] Drawbacks of liquid-liquid extraction are the use of large quantities of solvents and inefficient analyte transfer with a single extraction. On the other hand, in SPE, analyte is adsorbed on a solid support.[124] The availability of a wide variety of adsorbents makes SPE a versatile method. Analyte is adsorbed based on four types of interactions: hydrophobic (non-polar), hydrophilic (polar), ionic, or ligand-based (immunoaffinity).[125] Figure 1.7 shows the sequence of events performed in SPE. In general, SPE involves conditioning of the support with a weak eluent to activate surface functional groups. Next, sample is loaded onto the adsorbent, and unretained material is washed away. Finally, retained analyte is eluted. SPE adsorbents are prepared by packing surface-functionalized silica particles, in-situ UV photopolymerization of monolithic structures, and fabrication of porous membranes.[126-129] Silica beads have silanol groups on their surfaces which can be bonded to alkyl or aryl groups using silane chemistry. Butyl, octyl, and octadecyl are commonly used alkyl chains bonded to silica particles to extract non-polar to moderately polar analytes. Monolithic structures have gained interest in microfluidics because they are prepared in-situ, hence avoiding the difficulty of packing. Moreover, their surface areas and through pore sizes can be tuned by adjusting the porogens in the monolith solution.
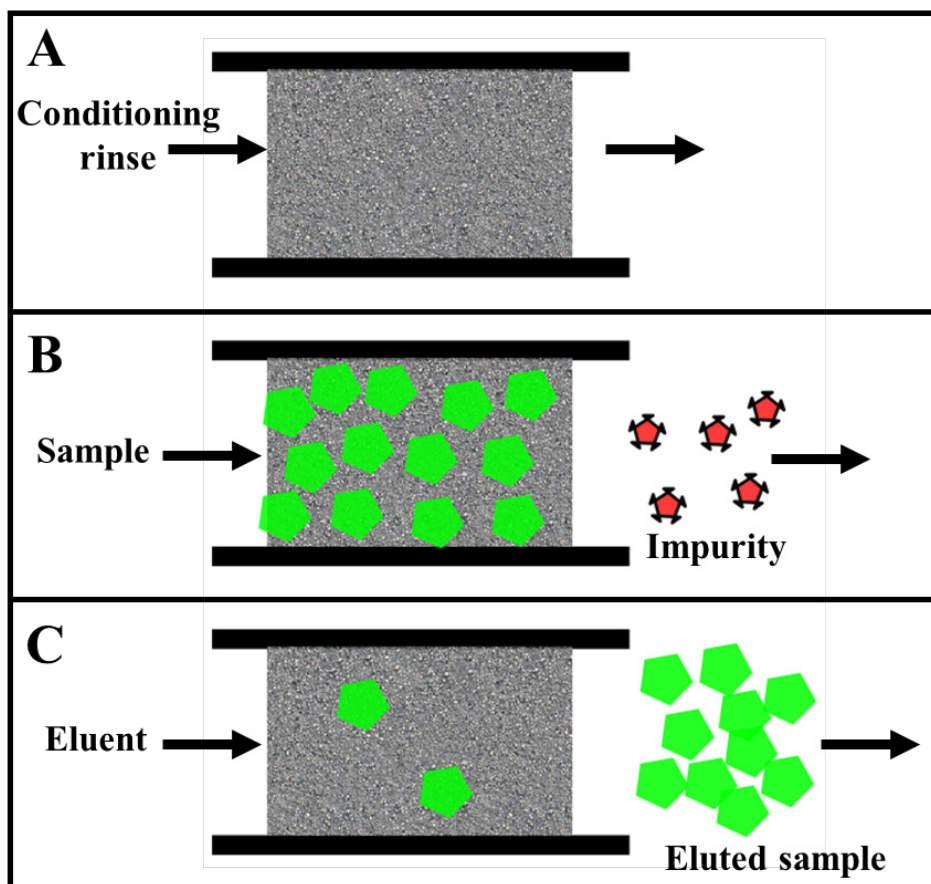
Figure 1.7 Schematic showing various steps in SPE. (A) Solid-support conditioning. (B) Sample loading. (C) Sample elution.

1.4.2 Preconcentration

Another important procedure in sample preparation is preconcentration, in which an analyte of interest is concentrated before introducing it into an analytical instrument.[130] For example, biomarkers in their native matrix are usually in the µg/mL-pg/mL range,[17, 26] so to improve their detection, they are often preconcentrated. The common methods of on-chip sample preconcentration are SPE and filtration, in which analyte solution is passed through a porous structure or a membrane, which results in surface interaction-based and size-based retention,

respectively.[131] Next, the analytes are eluted in concentrated form and analyzed. Preconcentration on monoliths and packed columns follows the same principles as SPE.

1.4.3 On-chip fluorescent labeling

LIF provides the lowest limits of detection in microfluidics, but requires labeling of analytes in most cases. Fluorescent labeling involves reaction between a functional group and a reactive dye. There are many functional groups like amines, thiols, and carboxylic acids for which fluorescent dyes are available commercially. Proteins are mostly labeled on primary amine groups available on lysine residues and the N-terminus. For labeling, a mixture of protein and dye is incubated at room temperature for 1 to 24 hours; faster labeling is advantageous as it saves time and can be used in on-chip analysis. After incubation, unreacted dye is filtered off, commonly using mass cutoff filters in an ultracentrifuge. This process is time consuming, and high protein concentrations (1-5 mg/mL) are required for labeling, which often results in sample waste. These drawbacks of conventional labeling can be addressed by labeling samples on-chip. On-chip labeling is faster and uses smaller quantities of reagents. Moreover, prepared sample is used immediately so photobleaching of dye during storage is not an issue. On-chip labeling also produces the possibility of integrating sample preparation and separation techniques on-chip for automation. On-chip labeling can be performed by flowing dye solution over adsorbed molecules in SPE columns. After rinsing the unreacted dye, labeled molecules are eluted.

1.5 DISSERTATION OVERVIEW

Biomarker analysis provides an excellent opportunity to diagnose diseases at an early stage, such that effective treatment can be initiated. However, existing analysis methods are expensive, time consuming, require experienced personnel, or are inconvenient for point-of-care applications.

Microfluidic and nanofluidic devices open up a new frontier and provide an opportunity to address the existing challenges in biomarker analysis. Nanofluidic structures are comparable to biomolecular sizes and, therefore, can be used to analyze molecules based on their size differences. Microfluidics can provide a complete automated analysis tool by integrating multiple processes such as on-chip sample enrichment, labeling, separation, and detection on a single platform. This dissertation focuses on developing new miniaturized devices for biomarker analysis. Chapters 2 and 3 develop a novel method for protein sieving using a size-based nanofluidic approach. Chapters 4, 5, and 6 focus on developing microfluidic-based devices that integrate SPE and μCE to provide PTB biomarker analysis. A brief overview of Chapters 2-6 in this dissertation is provided below.

In Chapter 2, I present the fabrication of an array of planar nanochannels with at least one dimension below 100 nm using thin-film microfabrication techniques. These nanochannels contain height steps where sub-hundred-nm particles are trapped size-selectively. I studied size-dependent fractionation of five proteins in five different height step devices. I evaluated the effects of protein size and concentration on trapping at the height steps, and helped in developing a mathematical model to predict trapping behavior. I also showed that altered buffer ionic strength influences the trapping behavior of proteins at height steps.

In Chapter 3, I fabricated single-height and height-step nanochannels with SiO_2 and Ta_2O_5 on the channel surface. I studied the effect of heat-treatment on protein signal at nanochannel exits. A heat-treatment protocol was developed to decrease the number of surface silanol groups in SiO_2 channels, which resulted in increased protein signal at the nanochannel exits. A similar effect was observed with Ta_2O_5 channels. This heat treatment reduced protein adsorption and improved signal at the channel exits.

In Chapter 4, I evaluated off-chip labeling of preterm birth biomarkers using capillary and microchip electrophoresis. An off-chip labeling protocol was developed for labeling PTB peptides. Additionally, time- and dye-dependent labeling of ferritin (Fer) was studied. A protocol for microchip electrophoresis was developed to separate four PTB biomarkers including three peptides and one protein.

In Chapter 5, I present fabrication processes for making on-chip solid phase extraction and separation modules, and their subsequent integration. On-chip pneumatic valves and a peristaltic pump were used to provide pressure-actuated fluid flow. Monolithic columns were fabricated to perform on-chip SPE and labeling.

In Chapter 6, I demonstrate operational aspects of the devices fabricated in Chapter 5. Channel dimensions were modified to improve valve actuation and flow rates. An SPE module was developed by individually studying Fer and dye retention and elution, three- and five-valve pumps, and Fer enrichment. On-chip labeling of Fer was also performed with labelled Fer separated by μCE, after sample injection and plug capture using microfabricated valves and pump.

In Chapter 7, I present my conclusions from these studies and describe possible expansions of the reported work.

1.6 REFERENCES

1.   Wang, X., Role of clinical bioinformatics in the development of network-based Biomarkers. *J. Clin. Bioinforma.* **2011,** *1*, 28.

2.   Berger, D., A brief history of medical diagnosis and the birth of the clinical laboratory. Part 1—Ancient times through the 19th century. *Med. Lab. Obs.* **1999,** *31*, 28-30.

3.   Emilia, E.; Neelakantan, P., Biomarkers in the Dentin-Pulp Complex: Role in Health and Disease. *J. Clin. Pediatr. Dent.* **2015,** *39*, 94-99.

4.   Ludwig, J. A.; Weinstein, J. N., Biomarkers in Cancer Staging, Prognosis and Treatment Selection. *Nat. Rev. Cancer* **2005,** *5*, 845-856.

5.   Diamandis, E. P.; Yousef, G. M., Human tissue kallikrein gene family: a rich source of novel disease biomarkers. *Expert Rev. Mol. Diagn.* **2001,** *1*, 182-90.

6.   Huang, J. T. J.; Leweke, F. M.; Oxley, D.; Wang, L.; Harris, N.; Koethe, D.; Gerth, C. W.; Nolden, B. M.; Gross, S.; Schreiber, D.; Reed, B.; Bahn, S., Disease Biomarkers in Cerebrospinal Fluid of Patients with First-Onset Psychosis. *PLoS Med.* **2006,** *3*, e428.

7.   Kutt, H., Biochemical and Genetic Factors Regulating Dilantin Metabolism in Man. *Annal. NY. Acad. Sci.* **1971,** *179*, 704-722.

8.   Müller-Oerlinghausen, B.; Berghöfer, A.; Bauer, M., Bipolar disorder. *Lancet* **2002,** *359*, 241-247.

9.   Gilad, S.; Meiri, E.; Yogev, Y.; Benjamin, S.; Lebanony, D.; Yerushalmi, N.; Benjamin, H.; Kushnir, M.; Cholakh, H.; Melamed, N.; Bentwich, Z.; Hod, M.; Goren, Y.; Chajut, A., Serum MicroRNAs Are Promising Novel Biomarkers. *PLoS One* **2008,** *3*, e3148.

10.   Kharitonov, S. A.; Barnes, P. J., Biomarkers of some pulmonary diseases in exhaled breath. *Biomarkers* **2002,** *7*, 1-32.

11.   Packer, N. H.; von der Lieth, C. W.; Aoki-Kinoshita, K. F.; Lebrilla, C. B.; Paulson, J. C.; Raman, R.; Rudd, P.; Sasisekharan, R.; Taniguchi, N.; York, W. S., Frontiers in glycomics: Bioinformatics and biomarkers in disease An NIH White Paper prepared from discussions by the focus groups at a workshop on the NIH campus, Bethesda MD (September 11–13, 2006). *Proteomics* **2008,** *8*, 8-20.

12.   Wang, J.; Chen, J.; Chang, P.; LeBlanc, A.; Li, D.; Abbruzzesse, J. L.; Frazier, M. L.; Killary, A. M.; Sen, S., MicroRNAs in Plasma of Pancreatic Ductal Adenocarcinoma Patients as Novel Blood-Based Biomarkers of Disease. *Cancer Prev, Res.* **2009,** *2*, 807-813.

13.   Shaw, L. M.; Vanderstichele, H.; Knapik-Czajka, M.; Clark, C. M.; Aisen, P. S.; Petersen, R. C.; Blennow, K.; Soares, H.; Simon, A.; Lewczuk, P.; Dean, R.; Siemers, E.; Potter, W.; Lee, V. M. Y.; Trojanowski, J. Q., Cerebrospinal fluid biomarker signature in Alzheimer's disease neuroimaging initiative subjects. *Ann. Neurol.* **2009,** *65*, 403-413.

14.   Skovronsky, D. M.; Lee, V. M.-Y.; Trojanowski, J. Q., Neurodegenerative Disease: New Concepts of Pathogenesis and Their Therapeutic Implications. *Annu. Rev. Pathol.-Mech.* **2006,** *1*, 151-170.

15.   Forman, M. S.; Trojanowski, J. Q.; Lee, V. M. Y., Neurodegenerative diseases: a decade of discoveries paves the way for therapeutic breakthroughs. *Nat. Med.* **2004,** *10*, 1055-1063.

16.   Shaw, L. M.; Korecka, M.; Clark, C. M.; Lee, V. M. Y.; Trojanowski, J. Q., Biomarkers of neurodegeneration for diagnosis and monitoring therapeutics. *Nat. Rev. Drug Discov.* **2007,** *6*, 295-303.

17.   Esplin, M. S.; Merrell, K.; Goldenberg, R.; Lai, Y.; Iams, J. D.; Mercer, B.; Spong, C. Y.; Miodovnik, M.; Simhan, H. N.; van Dorsten, P.; Dombrowski, M., Proteomic identification of

serum peptides predicting subsequent spontaneous preterm birth. *Am. J. Obstet. Gynecol.* **2011,** *204*, 391.e1-8.

18.   Judith, K. O., Relationship between baseline risk factors and coronary heart disease and total mortality in the Multiple Risk Factor Intervention Trial. *Prev. Med.* **1986,** *15*, 254-273.

19.   Manninen, V.; Tenkanen, L.; Koskinen, P.; Huttunen, J.; Mänttäri, M.; Heinonen, O.; Frick, M., Joint effects of serum triglyceride and LDL cholesterol and HDL cholesterol concentrations on coronary heart disease risk in the Helsinki Heart Study. Implications for treatment. *Circulation* **1992,** *85*, 37-45.

20.   Warnick, G. R.; McNamara, J. R.; Boggess, C. N.; Clendenen, F.; Williams, P. T.; Landolt, C. C., Polyacrylamide gradient gel electrophoresis of lipoprotein subclasses. *Clin. Lab. Med.* **2006,** *26*, 803-846.

21.   Johnson, P. J., The role of serum alpha-fetoprotein estimation in the diagnosis and management of hepatocellular carcinoma. *Clin. Liver Dis.* **2001,** *5*, 145-159.

22.   Farinati, F.; Marino, D.; De Giorgio, M.; Baldan, A.; Cantarini, M.; Cursaro, C.; Rapaccini, G.; Del Poggio, P.; Di Nolfo, M. A.; Benvegnù, L., Diagnostic and Prognostic Role of α-Fetoprotein in Hepatocellular Carcinoma: Both or Neither? *Am. J. Gastroenterol.* **2006,** *101*, 524-532.

23.   Isaacs, J. S.; Xu, W.; Neckers, L., Heat shock protein 90 as a molecular target for cancer therapeutics. *Cancer cell* **2003,** *3*, 213-217.

24.   Neckers, L., Heat shock protein 90: the cancer chaperone. In *Heat Shock Proteins in Cancer*, Springer: **2007**; pp 231-252.

25.   Morrow, D. A.; de Lemos, J. A.; Sabatine, M. S.; Antman, E. M., The search for a biomarker of cardiac ischemia. *Clin. Chem.* **2003,** *49*, 537-539.

26.   Polanski, M.; Anderson, N. L., A list of candidate cancer biomarkers for targeted proteomics. *Biomark. Insights* **2006,** *1*, 1.

27.   Kelleher, N. L., Peer reviewed: Top-down proteomics. *Anal. Chem.* **2004,** *76*, 196 A-203 A.

28.   Bigbee, W. L.; Gopalakrishnan, V.; Weissfeld, J. L.; Wilson, D. O.; Dacic, S.; Lokshin, A. E.; Siegfried, J. M., A multiplexed serum biomarker immunoassay panel discriminates clinical lung cancer patients from high-risk individuals found to be cancer-free by CT screening. *J. Thorac. Oncol.* **2012,** *7*, 698.

29.   Christodoulides, N.; Floriano, P. N.; Miller, C. S.; Ebersole, J. L.; Mohanty, S.; Dharshan, P.; Griffin, M.; Lennart, A.; Ballard, K. L. M.; King, C. P., Lab-on-a-chip methods for point-of-care measurements of salivary biomarkers of periodontitis. *Ann. NY. Acad. Sci.* **2007,** *1098*, 411-428.

30.   Mohammed, M.-I.; Desmulliez, M. P., Lab-on-a-chip based immunosensor principles and technologies for the detection of cardiac biomarkers: a review. *Lab Chip* **2011,** *11*, 569-595.

31.   Theodoridis, G.; Gika, H. G.; Wilson, I. D., LC-MS-based methodology for global metabolite profiling in metabonomics/metabolomics. *T. Anal. Chem.* **2008,** *27*, 251-260.

32.   Hornbeck, P., Enzyme-Linked Immunosorbent Assays. In *Current Protocols in Immunology*, John Wiley & Sons, Inc.: **2001**.

33.   Goldsmith, S. J., Radioimmunoassay: Review of basic principles. *Semin. Nucl. Med.* **1975,** *5*, 125-152.

34.   Blake, C.; Gould, B. J., Use of enzymes in immunoassay techniques. A review. *Analyst* **1984,** *109*, 533-547.

35.   Torrance, L.; Jones, R. A. C., Increased sensitivity of detection of plant viruses obtained by using a fluorogenic substrate in enzyme-linked immunosorbent assay. *Ann. Appl. Biol.* **1982,** *101*, 501-509.

36.   Paulie, S.; Perlmann, H.; Perlmann, P., Enzyme-linked Immunosorbent Assay. In *eLS*, John Wiley & Sons, Ltd: **2001**.

37.   Sato, K.; Hibara, A.; Tokeshi, M.; Hisamoto, H.; Kitamori, T., Integration of chemical and biochemical analysis systems into a glass microchip. *Anal. Sci.* **2003,** *19*, 15-22.

38.   Nge, P. N.; Rogers, C. I.; Woolley, A. T., Advances in microfluidic materials, functions, integration, and applications. *Chem. Rev.* **2013,** *113*, 2550-2583.

39.   Haeberle, S.; Mark, D.; von Stetten, F.; Zengerle, R., Microfluidic Platforms for Lab-On-A-Chip Applications. In *Microsystems and Nanotechnology*, Zhou, Z.; Wang, Z.; Lin, L., Eds. Springer Berlin Heidelberg: **2012**; pp 853-895.

40.   Nguyen, N.-T.; Shaegh, S. A. M.; Kashaninejad, N.; Phan, D.-T., Design, fabrication and characterization of drug delivery systems based on lab-on-a-chip technology. *Adv. Drug Deliver. Rev.* **2013,** *65*, 1403-1419.

41.   Kovarik, M. L.; Ornoff, D. M.; Melvin, A. T.; Dobes, N. C.; Wang, Y.; Dickinson, A. J.; Gach, P. C.; Shah, P. K.; Allbritton, N. L., Micro Total Analysis Systems: Fundamental Advances and Applications in the Laboratory, Clinic, and Field. *Anal. Chem.* **2013,** *85*, 451-472.

42.   Ríos, Á.; Zougagh, M.; Avila, M., Miniaturization through lab-on-a-chip: Utopia or reality for routine laboratories? A review. *Anal. Chim. Acta* **2012,** *740*, 1-11.

43.   Schoch, R. B.; Han, J.; Renaud, P., Transport phenomena in nanofluidics. *Rev. Mod. Phys.* **2008,** *80*, 839-883.

44.   Haywood, D. G.; Saha-Shah, A.; Baker, L. A.; Jacobson, S. C., Fundamental Studies of Nanofluidics: Nanopores, Nanochannels, and Nanopipets. *Anal. Chem.* **2015,** *87*, 172-187.

45.   Napoli, M.; Eijkel, J.; Pennathur, S., Nanofluidic technology for biomolecule applications: a critical review. *Lab Chip* **2010,** *10*, 957-985.

46.   Zhou, K.; Perry, J. M.; Jacobson, S. C., Transport and Sensing in Nanofluidic Devices. *Annu. Rev. Anal. Chem.* **2011,** *4*, 321-341.

47.   Eijkel, J. C.; Van Den Berg, A., Nanofluidics: what is it and what can we expect from it? *Microfluid. Nanofluid.* **2005,** *1*, 249-267.

48.   Prakash, S.; Piruska, A.; Gatimu, E. N.; Bohn, P. W.; Sweedler, J. V.; Shannon, M. A., Nanofluidics: Systems and Applications. *IEEE Sens. J.* **2008,** *8*, 441-450.

49.   Wang, Y.-C.; Stevens, A. L.; Han, J., Million-fold Preconcentration of Proteins and Peptides by Nanofluidic Filter. *Anal. Chem.* **2005,** *77*, 4293-4299.

50.   Han, J.; Craighead, H. G., Separation of Long DNA Molecules in a Microfabricated Entropic Trap Array. *Science* **2000,** *288*, 1026-1029.

51.   Perrillo, R.; Tamburro, C.; Regenstein, F.; Balart, L.; Bodenheimer, H.; Silva, M.; Schiff, E.; Bodicky, C.; Miller, B.; Denham, C.; Brodeur, C.; Roach, K.; Albrecht, J., Low-dose, titratable interferon alfa in decompensated liver disease caused by chronic infection with hepatitis B virus. *Gastroenterology* **1995,** *109*, 908-916.

52.   Duan, C.; Wang, W.; Xie, Q., Review article: Fabrication of nanofluidic devices. *Biomicrofluidics* **2013,** *7*, 026501.

53.   Han, A.; Mondin, G.; Hegelbach, N. G.; de Rooij, N. F.; Staufer, U., Filling kinetics of liquids in nanochannels as narrow as 27 nm by capillary force. *J. Colloid Interf. Sci.* **2006,** *293*, 151-157.

54.   Bohinc, K.; Kralj-Iglič, V.; Iglič, A., Thickness of electrical double layer. Effect of ion size. *Electrochim. Acta* **2001,** *46*, 3033-3040.

55.   Pu, Q.; Yun, J.; Temkin, H.; Liu, S., Ion-enrichment and ion-depletion effect of nanochannel structures. *Nano Lett.* **2004,** *4*, 1099-1103.

56.   Gillespie, D.; Pennathur, S., Separation of Ions in Nanofluidic Channels with Combined Pressure-Driven and Electro-Osmotic Flow. *Anal. Chem.* **2013,** *85*, 2991-2998.

57.   Matsumoto, K.; Kawakami, T.; Nakao, M.; Hatamura, Y.; Kitamori, T.; Sawada, T. In *Nano-channel on quartz-chip laboratory using single molecular detectable thermal lens microscope*, MEMS 98. Proceedings., The Eleventh Annual International Workshop, IEEE: **1998**; pp 127-130.

58.   Mao, P.; Han, J., Fabrication and characterization of 20 nm planar nanofluidic channels by glass–glass and glass–silicon bonding. *Lab Chip* **2005,** *5*, 837-844.

59.   Park, J.-H.; Sudarshan, T., *Chemical vapor deposition*. ASM international: **2001**; Vol. 2.

60.   Mahan, J. E., *Physical vapor deposition of thin films*. Wiley-VCH: **2000**; Vol. 1.

61.   Chantiwas, R.; Park, S.; Soper, S. A.; Kim, B. C.; Takayama, S.; Sunkara, V.; Hwang, H.; Cho, Y.-K., Flexible fabrication and applications of polymer nanochannels and nanoslits. *Chem. Soc. Rev.* **2011,** *40*, 3677-3702.

62.   Perry, J. L.; Kandlikar, S. G., Review of fabrication of nanochannels for single phase liquid flow. *Microfluid. Nanofluid.* **2006,** *2*, 185-193.

63.   Mijatovic, D.; Eijkel, J.; Van Den Berg, A., Technologies for nanofluidic systems: top-down vs. bottom-up—a review. *Lab Chip* **2005,** *5*, 492-500.

64.   Kovacs, G. T.; Maluf, N. I.; Petersen, K. E., Bulk micromachining of silicon. *P. IEEE* **1998,** *86*, 1536-1551.

65.   Jansen, H.; de Boer, M.; Legtenberg, R.; Elwenspoek, M., The black silicon method: a universal method for determining the parameter setting of a fluorine-based reactive ion etcher in deep silicon trench etching with profile control. *J. Micromech. Microeng.* **1995,** *5*, 115.

66.   Haneveld, J.; Jansen, H.; Berenschot, E.; Tas, N.; Elwenspoek, M., Wet anisotropic etching for fluidic 1D nanochannels. *J. Micromech. Microeng.* **2003,** *13*, S62.

67.   Chien, F. S.-S.; Wu, C.; Chou, Y.; Chen, T.; Gwo, S.; Hsieh, W.-F., Nanomachining of (110)-oriented silicon by scanning probe lithography and anisotropic wet etching. *Appl. Phys. Lett.* **1999,** *75*, 2429-2431.

68.   Xia, D.; Yan, J.; Hou, S., Fabrication of Nanofluidic Biochips with Nanochannels for Applications in DNA Analysis. *Small* **2012,** *8*, 2787-2801.

69.   Bustillo, J. M.; Howe, R. T.; Muller, R. S., Surface micromachining for microelectromechanical systems. *Pr. Inst. Electr. Elect.* **1998,** *86*, 1552-1574.

70.   Hamblin, M. N.; Xuan, J.; Maynes, D.; Tolley, H. D.; Belnap, D. M.; Woolley, A. T.; Lee, M. L.; Hawkins, A. R., Selective trapping and concentration of nanoparticles and viruses in dual-height nanofluidic channels. *Lab Chip* **2010,** *10*, 173-178.

71.   Sparreboom, W.; Eijkel, J. C.; Bomer, J.; van den Berg, A., Rapid sacrificial layer etching for the fabrication of nanochannels with integrated metal electrodes. *Lab Chip* **2008,** *8*, 402-407.

72.   Stern, M. B.; Geis, M. W.; Curtin, J. E., Nanochannel fabrication for chemical sensors. *J. Vac. Sci. Technol. B* **1997,** *15*, 2887-2891.

73.   Turner, S. W.; Perez, A. M.; Lopez, A.; Craighead, H. G., Monolithic nanofluid sieving structures for DNA manipulation. *J. Vac. Sci. Technol. B* **1998,** *16*, 3835-3840.

74.   Tas, N.; Berenschot, J.; Mela, P.; Jansen, H.; Elwenspoek, M.; Van den Berg, A., 2D-confined nanochannels fabricated by conventional micromachining. *Nano Lett.* **2002,** *2*, 1031-1032.

75.   Chou, S. Y.; Krauss, P. R.; Renstrom, P. J., Nanoimprint lithography. *J. Vac. Sci. Technol. B* **1996,** *14*, 4129-4133.

76.   Guo, L. J., Nanoimprint lithography: methods and material requirements. *Adv. Mater.* **2007,** *19*, 495.

77.   Khang, D.-Y.; Kang, H.; Kim, T.-I.; Lee, H. H., Low-pressure nanoimprint lithography. *Nano Lett.* **2004,** *4*, 633-637.

78.   Thamdrup, L. H.; Klukowska, A.; Kristensen, A., Stretching DNA in polymer nanochannels fabricated by thermal imprint in PMMA. *Nanotechnology* **2008,** *19*, 125301.

79.   Cho, Y.; Park, J.; Park, H.; Cheng, X.; Kim, B.; Han, A., Fabrication of high-aspect-ratio polymer nanochannels using a novel Si nanoimprint mold and solvent-assisted sealing. *Microfluid. Nanofluid.* **2010,** *9*, 163-170.

80.   Biswas, A.; Bayer, I. S.; Biris, A. S.; Wang, T.; Dervishi, E.; Faupel, F., Advances in top–down and bottom–up surface nanofabrication: Techniques, applications and future prospects. *Adv. Colloid Interfac.* **2012,** *170*, 2-27.

81.   van den Berg, A.; Craighead, H. G.; Yang, P., From microfluidic applications to nanofluidic phenomena. *Chem. Soc. Rev.* **2010,** *39*, 899-900.

82.   Min, S. K.; Kim, W. Y.; Cho, Y.; Kim, K. S., Fast DNA sequencing with a graphene-based nanochannel device. *Nat. Nanotechnol.* **2011,** *6*, 162-165.

83.   Xuan, J.; Lee, M. L., Size separation of biomolecules and bioparticles using micro/nanofabricated structures. *Anal. Method.* **2014,** *6*, 27-37.

37

84.   Fu, J.; Yoo, J.; Han, J., Molecular Sieving in Periodic Free-Energy Landscapes Created by Patterned Nanofilter Arrays. *Phys. Rev. Lett.* **2006,** *97*, 018103.

85.   Gupta, C.; Liao, W.-C.; Gallego-Perez, D.; Castro, C. E.; Lee, L. J., DNA translocation through short nanofluidic channels under asymmetric pulsed electric field. *Biomicrofluidics* **2014,** *8*, 024114.

86.   Zeng, Y.; Harrison, D. J., Self-assembled colloidal arrays as three-dimensional nanofluidic sieves for separation of biomolecules on microchips. *Anal. Chem.* **2007,** *79*, 2289-2295.

87.   Inglis, D. W.; Goldys, E. M.; Calander, N. P., Simultaneous Concentration and Separation of Proteins in a Nanochannel. *Angew. Chem. Int. Ed.* **2011,** *50*, 7546-7550.

88.   Whitesides, G. M., The origins and the future of microfluidics. *Nature* **2006,** *442*, 368-373.

89.   Terry, S. C.; Jerman, J. H.; Angell, J. B., A gas chromatographic air analyzer fabricated on a silicon wafer. *IEEE Trans. Electron Devices* **1979,** *26*, 1880-1886.

90.   Manz, A.; Miyahara, Y.; Miura, J.; Watanabe, Y.; Miyagi, H.; Sato, K., Design of an open-tubular column liquid chromatograph using silicon chip technology. *Sensor. Actuat. B-Chem.* **1990,** *1*, 249-255.

91.   Manz, A.; Graber, N.; Widmer, H. M., Miniaturized total chemical analysis systems: a novel concept for chemical sensing. *Sensor. Actuat. B-Chem.* **1990,** *1*, 244-248.

92.   Harrison, D. J.; Manz, A.; Fan, Z.; Luedi, H.; Widmer, H. M., Capillary electrophoresis and sample injection systems integrated on a planar glass chip. *Anal. Chem.* **1992,** *64*, 1926-1932.

93.   Reyes, D. R.; Iossifidis, D.; Auroux, P.-A.; Manz, A., Micro total analysis systems. 1. Introduction, theory, and technology. *Anal. Chem.* **2002,** *74*, 2623-2636.

94.   Tang, S. K.; Whitesides, G. M., *Optofluidics: Fundamentals, Devices and Applications*. McGraw-Hill: **2009**.

95.   Khandurina, J.; Guttman, A., Bioanalysis in microfluidic devices. *J. Chromatogr. A* **2002,** *943*, 159-183.

96.   Beebe, D. J.; Mensing, G. A.; Walker, G. M., Physics and applications of microfluidics in biology. *Annu. Rev. Biomed. Eng.* **2002,** *4*, 261-286.

97.   Lee, C.-Y.; Chang, C.-L.; Wang, Y.-N.; Fu, L.-M., Microfluidic mixing: a review. *Int. J. Mol. Sci.* **2011,** *12*, 3263-3287.

98.   Lacher, N. A.; Garrison, K. E.; Martin, R. S.; Lunte, S. M., Microchip capillary electrophoresis/ electrochemistry. *Electrophoresis* **2001,** *22*, 2526-2536.

99.   Weigl, B. H.; Bardell, R. L.; Cabrera, C. R., Lab-on-a-chip for drug development. *Adv. Drug Deliver. Rev.* **2003,** *55*, 349-377.

100.   Boone, T. D.; Fan, Z. H.; Hooper, H. H.; Ricco, A. J.; Tan, H.; Williams, S. J., Peer Reviewed: Plastic Advances Microfluidic Devices. *Anal. Chem.* **2002,** *74*, 78 A-86 A.

101.   Chen, Y.; Zhang, L.; Chen, G., Fabrication, modification, and application of poly (methyl methacrylate) microfluidic chips. *Electrophoresis* **2008,** *29*, 1801-1814.

102.   Nunes, P. S.; Ohlsson, P. D.; Ordeig, O.; Kutter, J. P., Cyclic olefin polymers: emerging materials for lab-on-a-chip applications. *Microfluid. Nanofluid.* **2010,** *9*, 145-161.

103.   McDonald, J. C.; Whitesides, G. M., Poly (dimethylsiloxane) as a material for fabricating microfluidic devices. *Accounts Chem. Res.* **2002,** *35*, 491-499.

104.   Zhou, J.; Ellis, A. V.; Voelcker, N. H., Recent developments in PDMS surface modification for microfluidic devices. *Electrophoresis* **2010,** *31*, 2-16.

105.   Fiorini, G. S.; Chiu, D. T., Disposable microfluidic devices: fabrication, function, and application. *Biotechniques* **2005,** *38*, 429-446.

106.   Anderson, J. R.; Chiu, D. T.; Wu, H.; Schueller, O.; Whitesides, G. M., Fabrication of microfluidic systems in poly (dimethylsiloxane). *Electrophoresis* **2000,** *21*, 27-40.

107.   Comina, G.; Suska, A.; Filippini, D., PDMS lab-on-a-chip fabrication using 3D printed templates. *Lab Chip* **2013,** *14*, 424-430.

108.   Kelly, R. T.; Woolley, A. T., Thermal bonding of polymeric capillary electrophoresis microdevices in water. *Anal. Chem.* **2003,** *75*, 1941-1945.

109.   Takamura, Y.; Onoda, H.; Inokuchi, H.; Adachi, S.; Oki, A.; Horiike, Y., Low-voltage electroosmosis pump for stand-alone microfluidics devices. *Electrophoresis* **2003,** *24*, 185-192.

110.   Melin, J.; Quake, S. R., Microfluidic large-scale integration: the evolution of design rules for biological automation. *Annu. Rev. Biophys. Biomol. Struct.* **2007,** *36*, 213-231.

111.   Nguyen, N.-T.; Wereley, S. T., *Fundamentals and Applications of Microfluidics*. Ist ed.; Artech house: Massachusetts, **2002**.

112.   Hosokawa, K.; Maeda, R., A pneumatically-actuated three-way microvalve fabricated with polydimethylsiloxane using the membrane transfer technique. *J. Micromech. Microeng.* **2000,** *10*, 415.

113.   Grover, W. H.; Skelley, A. M.; Liu, C. N.; Lagally, E. T.; Mathies, R. A., Monolithic membrane valves and diaphragm pumps for practical large-scale integration into glass microfluidic devices. *Sensor. Actuat. B-Chem.* **2003,** *89*, 315-323.

114.   Xu, Y., Tutorial: capillary electrophoresis. *Chem. Educ.* **1996,** *1*, 1-14.

115.   Dolník, V.; Liu, S.; Jovanovich, S., Capillary electrophoresis on microchip. *Electrophoresis* **2000,** *21*, 41-54.

116.   Karlinsey, J. M., Sample introduction techniques for microchip electrophoresis: A review. *Anal. Chim. Acta* **2012,** *725*, 1-13.

117.   Hupert, M. L.; Guy, W. J.; Llopis, S. D.; Shadpour, H.; Rani, S.; Nikitopoulos, D. E.; Soper, S. A., Evaluation of micromilled metal mold masters for the replication of microchip electrophoresis devices. *Microfluid. Nanofluid.* **2007,** *3*, 1-11.

118.   Zhang, C.-X.; Manz, A., Narrow sample channel injectors for capillary electrophoresis on microchips. *Anal. Chem.* **2001,** *73*, 2656-2662.

119.   Götz, S.; Karst, U., Recent developments in optical detection methods for microchip separations. *Anal. Bioanal. Chem.* **2007,** *387*, 183-192.

120.   Fair, R. B., Digital microfluidics: is a true lab-on-a-chip possible? *Microfluid. Nanofluid.* **2007,** *3*, 245-281.

121.   Govindarajan, A.; Ramachandran, S.; Vigil, G.; Yager, P.; Böhringer, K., A low cost point-of-care viscous sample preparation device for molecular diagnosis in the developing world; an example of microfluidic origami. *Lab Chip* **2012,** *12*, 174-181.

122.   Erickson, D.; Li, D., Integrated microfluidic devices. *Anal. Chim. Acta* **2004,** *507*, 11-26.

123.   Vazquez-Roig, P.; Picó, Y., Pressurized liquid extraction of organic contaminants in environmental and food samples. *T. Anal. Chem.* **2015,** *(doi:10.1016/j.trac.2015.04.014)*.

124.   Poole, C. F., New trends in solid-phase extraction. *T. Anal. Chem.* **2003,** *22*, 362-373.

125.   Żwir-Ferenc, A.; Biziuk, M., Solid phase extraction technique–trends, opportunities and applications. *Pol. J. Environ. Stud.* **2006,** *15*, 677-690.

126.   Broyles, B. S.; Jacobson, S. C.; Ramsey, J. M., Sample filtration, concentration, and separation integrated on microfluidic devices. *Anal. Chem.* **2003,** *75*, 2761-2767.

127.   Foote, R. S.; Khandurina, J.; Jacobson, S. C.; Ramsey, J. M., Preconcentration of proteins on microfluidic devices using porous silica membranes. *Anal. Chem.* **2005,** *77*, 57-63.

128.   Bhattacharyya, A.; Klapperich, C. M., Thermoplastic microfluidic device for on-chip purification of nucleic acids for disposable diagnostics. *Anal. Chem.* **2006,** *78*, 788-792.

129.   Ramsey, J. D.; Collins, G. E., Integrated microfluidic device for solid-phase extraction coupled to micellar electrokinetic chromatography separation. *Anal. Chem.* **2005,** *77*, 6664-6670.

130.   Giordano, B. C.; Burgi, D. S.; Hart, S. J.; Terray, A., On-line sample pre-concentration in microfluidic devices: A review. *Anal. Chim. Acta* **2012,** *718*, 11-24.

131.   Sueyoshi, K.; Kitagawa, F.; Otsuka, K., Recent progress of online sample preconcentration techniques in microchip electrophoresis. *J. Sep. Sci.* **2008,** *31*, 2650-2666.

2. THIN-FILM MICROFABRICATED NANOFLUIDIC ARRAYS FOR SIZE-SELECTIVE PROTEIN FRACTIONATION*

2.1 INTRODUCTION

Various biostructures in the sub-hundred nanometer range are associated with human diseases.[1-3] For example, hepatitis B virus causes liver disease,[4] and lipoprotein size and concentration distribution is linked with cardiovascular disease.[5] High density lipoprotein (HDL) and low density lipoprotein (LDL), with diameters in the 5 to 25 nm size range, are important in cardiovascular risk assessment. Additionally, aggregation in pharmaceutical protein formulations is a major issue that can render a formulation physically unstable.[6] Therefore, size-selective fractionation and distribution studies of these molecules or particles are an important analytical research area.

There are several techniques available to separate biomolecules based on size; for example, size exclusion chromatography (SEC), field flow fractionation (FFF), membrane filtration, ultracentrifugation, and electrophoresis. However, these techniques all have limitations. SEC can reproducibly separate molecules based on size but requires a >10% difference in molecular weight for adequate resolution.[7] FFF can separate molecules and particles in the size range of 1 nm to 50 μm based on their interaction with an external applied field.[8] However, FFF requires a complex setup and experienced personnel. Membrane filtration fractionates based on a single cutoff size but suffers from sample loss, fouling, and pore clogging.[9] Ultracentrifugation, which separates molecules based on size or density, is slow (>24 h) and energy intensive.[10-11] Gradient gel electrophoresis can separate biomolecules with high resolution based on electrophoretic mobility, but this technique is time consuming (~18 h) and requires skilled personnel.[12] Thus, improved

methods for size fractionation of biostructures, especially in the 5-100 nm size range, are needed to overcome the disadvantages of current approaches.

Nanofluidics studies the behavior and manipulation of fluids confined in 1-100 nm dimensions.[13] In these small size scales, fluids exhibit phenomena different from those at macroscale or even microscale levels due to overlap of these dimensions with molecular sizes and the electric double layer (EDL) formed on channel walls. Nanofluidics is a growing field of research because various biostructures including proteins, nucleic acids, and viruses have sizes comparable to nanofluidic dimensions. Ongoing developments in micro and nanofabrication, including nanoimprint lithography, sacrificial approaches, etching, and bonding methods, have furthered the field of nanofluidics by enabling the fabrication of controlled nanostructures.[14] Nanochannels smaller than 5 nm in width have been made by using focused ion beam milling.[15] There are many fields such as biophysics and separation science where nanofluidics is now being evaluated,[16] for example in pre-concentration and separation of proteins and nucleic acids,[17-18] and single molecule DNA sequencing.[19] There are several challenges in making nanoscale devices, such as the fabrication costs imposed by high-resolution methods like focused ion beam milling and e-beam lithography; and issues with precision in channel dimensions, particularly after bonding steps. These challenges are especially problematic for fabricating nanochannels with dimensions below 30 nm.

An EDL is formed on surfaces when in contact with ionic solution, and it becomes prominent when critical dimensions drop below 100 nm.[20-22] The EDL thickness can range from sub-nm to 100 nm and correlates inversely with buffer ionic strength. In my sieving system, the EDL formed on the channel walls can extend deep into the channel and change the effective height

of a nanochannel. This altered cross-sectional area can influence the transport of charged biostructures through nanochannels depending on their interaction with the EDL.

Here, I have developed a nanofluidic-based sieving system that provides size separation of structures such as proteins in the ~10 nm diameter range. This system consists of an array of 200 parallel nanochannels having height steps from 100 nm down to 15-30 nm. These readily adjustable heights can be achieved using widely available, standard thin-film micromachining methods. Capillary action draws solutions through the nanochannels, with larger molecules being trapped at the height steps while smaller molecules reach the ends of the nanochannels. I have evaluated this system with five model proteins whose sizes approximate those of HDL and LDL. I have measured the effects of protein diameter and nanochannel step height on trapping behavior of proteins. Additionally, the influence of protein concentration on trapping was studied. These data provide an understanding of the correlation between protein size and height step, information that I have compared to a predictive model of size-based nanosieving. This chapter also includes a study on buffer ionic strength effects on trapping behavior of proteins in nanochannels. This new system offers advantages over current nanoscale fractionation methods in terms of device size and simplicity, reduction of reagent volumes, and assay speed.

2.2 EXPERIMENTAL

2.2.1 Materials and reagents

As shown in Table 2.1, five proteins of different diameters from 3.5-17 nm[23-26] were obtained from Sigma-Aldrich, St. Louis, MO. Each protein was labeled with fluorescein isothiocyanate (FITC, Invitrogen, Eugene, OR) for fluorescence detection. A 4 mg/mL stock solution of FITC was prepared in dimethyl sulfoxide (DMSO, Sigma-Aldrich), and stock solutions

of 2-3 mg/mL of each protein were prepared in 100 mM bicarbonate buffer at pH 9. Then, 20 µL of FITC stock solution was added to 250 µL of protein stock solution and incubated in the dark for 24 h at room temperature. Next, excess dye was removed from the protein solution using centrifugal membrane filters (Millipore, Billerica, MA) with mass cutoffs of 10 kDa (Mb), 30 kDa (Hb), and 100 kDa (Fer, Ct, and Tg). Protein solutions were rinsed multiple times with 10 mM bicarbonate buffer (pH 8.3) in an Eppendorf microcentrifuge (Hauppauge, NY) at 10,000 rpm for 6-8 min until a clear filtrate was obtained. Finally, bicarbonate buffer was replaced with 100 mM Tris-HCl buffer (pH 8.3) containing 2 mM sodium azide to make up the final volume of protein stock solution. The final stock concentration of each protein was measured using a Nanodrop spectrophotometer (ND-1000, Wilmington, DE). Subsequently, 1.0, 0.5, 0.1, and 0.05 mg/mL solutions of each protein were prepared volumetrically from the stock solution in 100 mM Tris-HCl buffer (pH 8.3), containing 1 mM sodium dodecyl sulfate (SDS, Shelton Scientific, Peosta, IA) and 0.12% v/v Triton X-100 (Sigma-Aldrich) as surfactants. I also prepared 0.5 mg/mL solutions of Tg and Ct in 1.0, 10.0, 50.0, and 100.0 mM Tris-HCl buffer (pH 8.3), containing 1 mM SDS and 0.12% v/v Triton-X-100 as surfactants. All solutions were stored at 4 ºC and vortexed before use to make a uniform solution.

Table 2.1 Proteins of different sizes used in nanosieving experiments.

Protein	Abbreviation	Molecular weight (kDa)	Diameter (nm)
Myoglobin	Mb	17	3.5
Hemoglobin	Hb	64.5	5.5
Catalase	Ct	247.5	10-11
Ferritin	Fer	450	11-12
Thyroglobulin	Tg	669	17

2.2.2 Device layout and fabrication

Device design and fabrication are adapted from Hamblin et al.[27] Briefly, devices are fabricated on a 4" Si wafer using UV photolithography, thin metal film deposition, plasma enhanced chemical vapor deposition (PECVD), and wet and dry etching. Each 4" Si wafer produces 49 devices; each device has dimensions of 1 cm^2 and consists of 200 parallel nanochannels with height steps. These nanochannels are connected to an injection and waste reservoir for solution loading and solvent evaporation, respectively, as shown in Figure 2.1. Figure 2.1A shows a top view photograph of a completed device. Figure 2.1B-C shows zoom photomicrographs of nanochannels, reservoirs, and the height steps. Figure 2.1D-F shows schematically the relatively simple operational principles of these nanosieving devices.
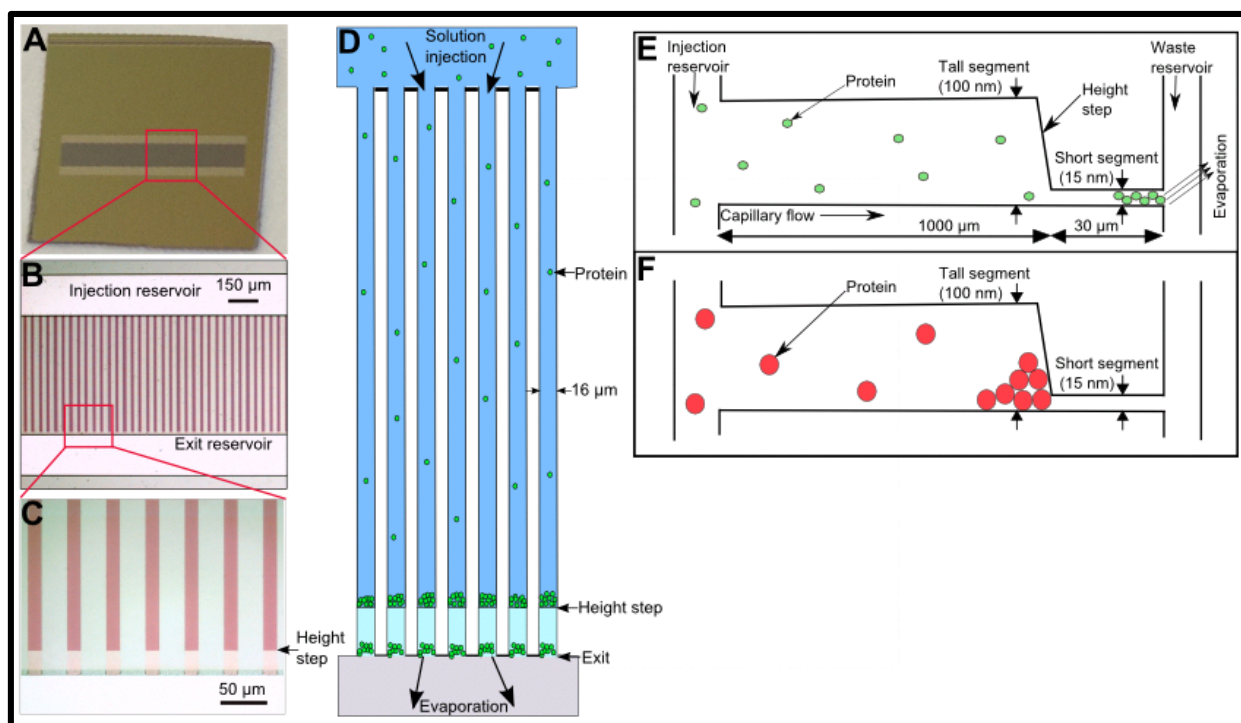
Figure 2.1 Overview of device design and operation. (A) Top view photograph of a nanodevice having 1 cm² dimensions. (B) Magnified photo of channels. (C) Zoom view photo showing height steps and exit reservoir. (D) Top view schematic showing operation of device including solution injection, flow and trapping of protein in nanochannels. (E-F) Side view schematics; channel lengths are not drawn to scale. (E) A ~10 nm protein passes through a 100-15 nm height step and accumulates at the exit. (F) A ~17 nm protein traps at a 100-15 nm height step.

The device fabrication scheme is shown in Figure 2.2. The following steps are involved in the fabrication of height step nanodevices. A ~100 nm layer of silicon dioxide is deposited on a clean 4" Si <100> wafer (Nova Electronic Materials, Flower Mound, TX) using PECVD; then, a layer of Al is deposited using e-beam evaporation with the thickness equal to the intended height of the shorter segment (Figure 2.2A). A ~15 nm thick Cr protecting layer is next deposited via e-beam evaporation as shown in Figure 2.2B. Photoresist (AZ nLOF 2020, AZ Electronic Materials, Branchburg, NJ) is then spun and patterned using photolithography, followed by Cr removal using chrome mask etchant (OMG Cyantek, Fremont, CA) in preparation for the second layer of Al to

48

be deposited to make the taller nanochannel segments (Figure 2.2C). A second layer of Al is deposited; the sum of the thicknesses of the first and second depositions is equal to the height of the taller nanochannel segments (Figure 2.2D). After a Cr protective layer is deposited, Al is lifted off by dissolving the photoresist in N-methyl-2-pyrrolidone (Spectrum, New Brunswick, NJ) at 90 $^\circ$C and then the Cr is again removed using chrome mask etchant. AZ 3330 photoresist is next spun on the wafer and patterned to cover the core nanochannel lines as shown in Figure 2.2E. Exposed Al is etched in Al etchant (Type A, Transene, Danvers, MA) at 50 $^\circ$C until Al is removed (~2 min), followed by photoresist stripping with acetone and 2-propanol (Figure 2.2F). A 4 µm thick capping layer of SiO_2 is next deposited using PECVD to cover the core lines as illustrated in Figure 2.2G. AZ 3330 photoresist is spun on the substrate and patterned to define injection and waste reservoirs (Figure 2.2H). Next, exposed oxide is etched completely down to the Si wafer in buffered oxide etchant (BOE, Transene) to open the channel ends into the reservoirs (Figure 2.2I). Finally, Al core lines are etched in aqua regia at 130 $^\circ$C overnight to remove the sacrificial cores and open up the nanochannels, which are then soaked in deionized water for 4-6 h (Figure 2.2J). I made five sets of devices, having a height step from 100 nm down to either 15, 18, 19.5, 22 or 29 nm; all other channel dimensions (length and widths) were held constant.
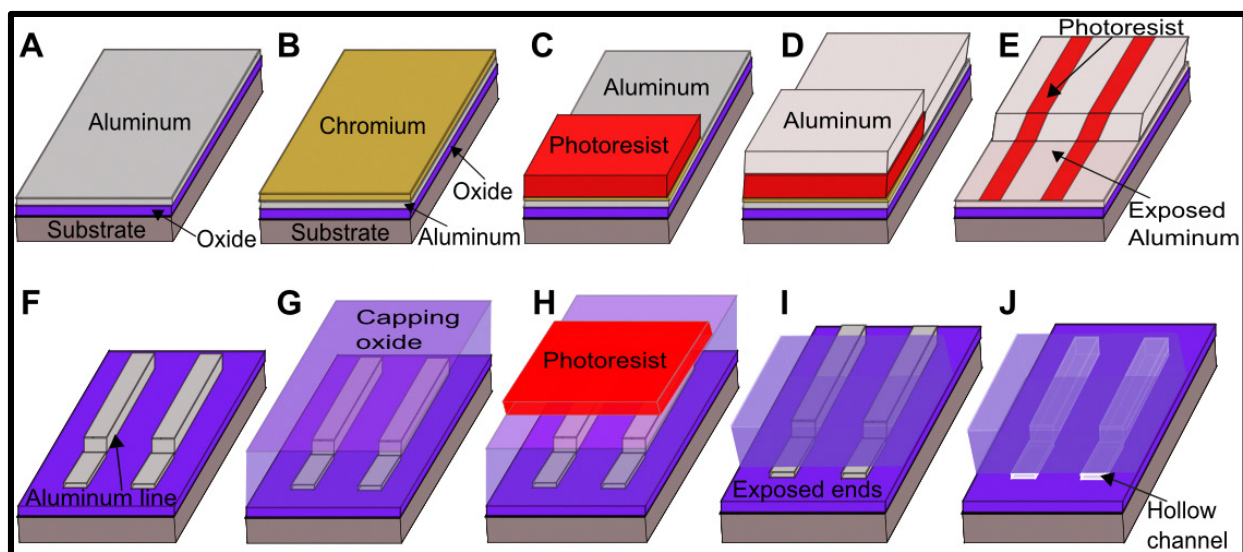
Figure 2.2 Fabrication of dual height nanochannels. (A) A ~100 nm thick oxide layer is deposited on a 4" Si wafer followed by an Al layer. (B) A ~15 nm thick Cr protective layer is deposited. (C) Photoresist is coated and patterned using photolithography and the exposed Cr is removed. (D) A second Al layer is deposited to make the tall segment. (E) After depositing a 15 nm Cr protective layer, Al is lifted off and Cr is removed. Then photoresist is coated and patterned. (F) Exposed Al is removed followed by photoresist stripping. (G) A capping layer of ~4 μm thick oxide is deposited to cover core lines. (H) Photoresist is coated and patterned. (I) Exposed oxide is etched to open the ends. (J) Aluminum lines are etched using aqua regia, and the hollow channels are then filled with water.

I made two important modifications to the previous fabrication method[27] to increase reliability and reproducibility, enabling capillary flow in channels with height steps as small as 15 nm. First, I used a ~15 nm Cr layer to protect the Al layers from the photoresist developer (AZ300 MIF, AZ Electronic Materials) as shown in Figure 2.2B. AZ300 developer slowly etches Al, resulting in inconsistent height steps, as well as discontinuities in <20 nm height channels. Secondly, the short segment length and tall segment height were both decreased to ~30 μm and 100 nm, respectively, to reduce the hydraulic resistance difference between these segments. These improvements enabled fabrication of devices with short segment heights down to 15 nm that

sustained capillary flow without any bubble formation. This smaller height range is especially important because it opens the possibility of separating proteins. In addition, I streamlined several fabrication steps, such as overnight water and Nanostrip (OMG Cyantek) treatment of nanochannels, which shortened the fabrication time by ~50%. Step heights were confirmed using atomic force microscopy (AFM) for all five device types as shown in Figures 2.3 and 2.4. Prior to trapping experiments, all devices were baked at 110 ºC, 170 ºC, and then 250 ºC, for 15 min at each temperature. This helped to remove any water that had condensed on the channel surfaces during storage and also aided in preventing bubble formation during capillary flow. Additionally, the high temperature bake decreased the number of free surface silanol groups, which could interact with proteins and cause adsorption.[28] My scalable, thin-film fabrication approach provides for batch processing of ~50 chips per 10-cm-diameter wafer, such that individual devices are considered to be single use and disposable. However, I note that a Nanostrip soak after trapping experiments could potentially be implemented to clean out and reuse devices.
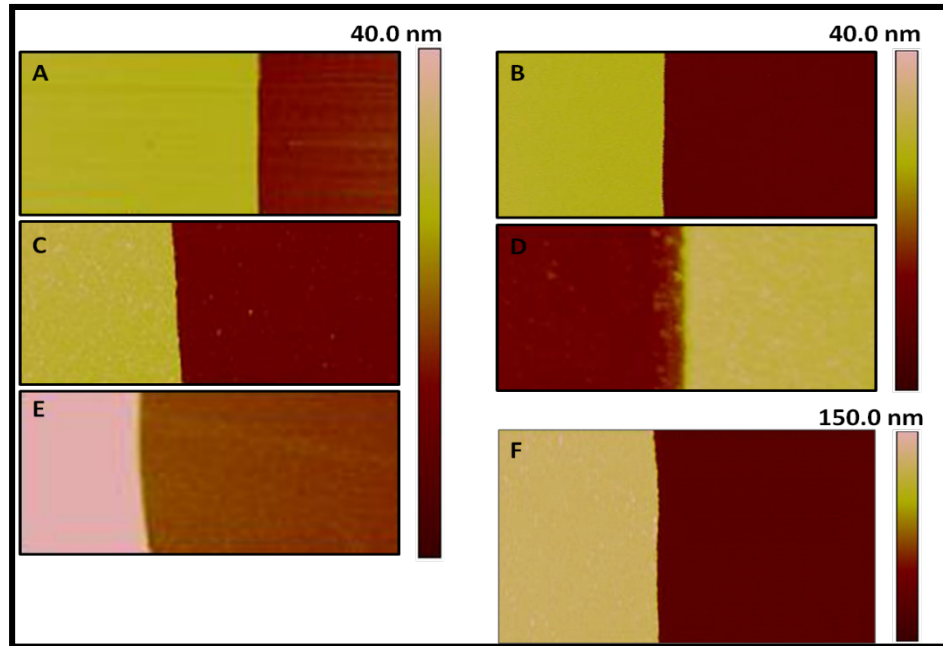
Figure 2.3 AFM measurement of height steps. (A) 15 nm, (B) 18 nm, (C) 19.5 nm, (D) 22 nm, (E) 29 nm, and (F) 100 nm.
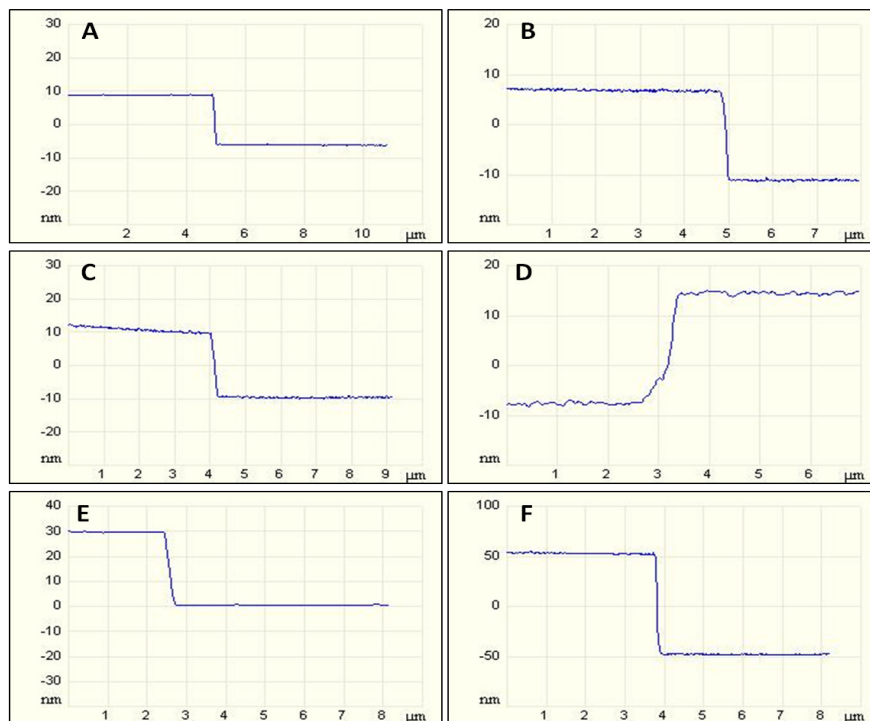
Figure 2.4 Traces of individual height measurements obtained from the corresponding AFM images in Figure 2.3. (A) 15.3 nm, (B) 17.9 nm, (C) 19.6 nm, (D) 21.6 nm, (E) 29.3 nm, and (F) 100.0 nm.

52

2.2.3 Device operation

Nanochannels with height steps can be used to separate proteins based on their size as illustrated schematically in Figure 2.1D-F. I studied the trapping behavior of five different size proteins in five different sets of devices to understand the height step and protein size correlation. Each device design was used to test four different concentrations (0.05, 0.1, 0.5, and 1.0 mg/mL) of each protein, and each concentration was run on three different devices from the same wafer to assess reproducibility. For each experiment, 400-500 nL of protein solution was loaded into the injection reservoir using a 5 µL syringe (Hamilton, Reno, NV), which caused filling of the nanochannels due to capillary action. Some protein was trapped at the height step, while protein that made it through the step accumulated at the exit. Solvent evaporation occurred from the channel ends after capillary flow maintained some additional flow. Each trapping experiment was run for 1.5 min. I also studied the trapping of Tg and Ct in 100-22 nm devices and Tg in 100-29 nm devices under different buffer ionic strengths (1, 10, 50, and 100 mM). The experimental setup used to record fluorescence signal included an upright Axio Scope.A1 microscope (Zeiss, Thornwood, NY) fitted with a 625 mW blue LED light source (470 nm center wavelength, MBLED, Thorlabs, Newton, NJ). A brightline filter cube (FITC-LP01-Clinical-OMF, Semrock, Rochester, NY) consisting of a longpass dichroic mirror with a cutoff wavelength of 515 nm was used to separate excitation and emission signals. Fluorescence was detected using a Photometrics CoolSNAP HQ2 (Tucson, AZ) cooled CCD camera at 1.67 Hz with a 600 ms exposure time. The entire detection system was controlled using Micromanager 1.3, an open source, free plug-in to ImageJ.

2.2.4 Data analysis

Statistical data analysis was performed on each fluorescence image. I measured the average fluorescence intensity by drawing the same size region of interest around the fluorescence signal at the height step and the nanochannel exit, using ImageJ software. For each image, background-subtracted intensity measurements were made on nine nanochannels. The same size region of interest was used for all nine channels in an image. The region of interest width was kept constant at 30 pixels (~20 μm), while the region of interest length was set to encompass the longest fluorescence signal in each image (25 to 40 pixels). Then the ratio of fluorescence intensity at the height step (trapped, T) divided by the sum of the signals from the height step and exit (total, t) was measured (T/t) for each channel. From the triplicate data sets for each concentration, an average T/t ratio and pooled standard deviation were calculated. Triplicate data analysis also helped in assessing the reproducibility between devices obtained from the same wafer.

2.3 RESULTS AND DISCUSSION

The effect of protein size and concentration on trapping behavior was explored using five different size proteins and five different height step devices. This correlation study provides useful insight into the trapping behavior of biomolecules in the 5-20 nm size range at the nanosize openings, and can serve as a guide to devise nanofluidic devices for separating two or more proteins of different sizes.

2.3.1 Trapping patterns of different proteins in devices with the same height step

The five proteins are trapped with different ratios in devices with the same height step due to their different sizes and shapes. Figure 2.5 shows representative fluorescence images of the five proteins after loading at 0.1 mg/mL in devices with height steps from 100-15 nm. Figure 2.5A

shows that the smallest protein (Mb) traversed the entire length of the nanochannels with minimal stoppage at the height step and significant accumulation at the exit. Figure 2.5B shows that Hb also largely passed through the height step, although a small proportion of the total Hb was trapped. Increasing amounts of Ct and Fer were trapped at the height step, and decreasing amounts passed through to the exit for these larger proteins as seen in Figure 2.5C-D. Finally, the largest protein (Tg) was almost completely trapped at the height step as shown in Figure 2.5E, with very little passing through to the exit. Overall, trapping at the 15 nm height step increased as the size of protein increased, even though the height step was larger than the protein diameter for all except Tg.
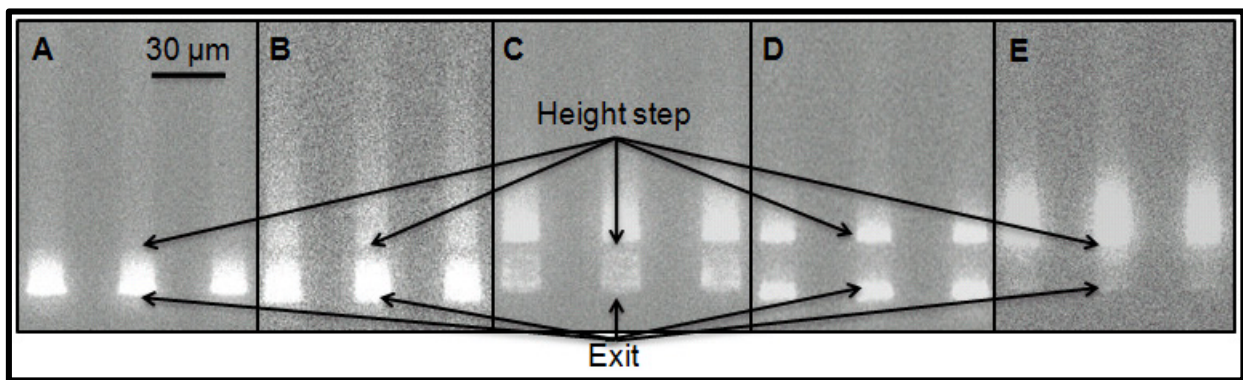
Figure 2.5 Images showing protein trapping at a height step of 100-15 nm as protein diameter increases from (A-E). All protein concentrations are 0.1 mg/mL. (A) Mb, (B) Hb, (C) Ct, (D) Fer, and (E) Tg.

2.3.2 Trapping patterns of the same protein in devices with different height steps

I also investigated the effect of changing the height step on trapping behavior of a given protein. Figure 2.6 shows fluorescence images taken for trapping of Tg (0.1 mg/mL) in five different height step devices. In the 15 nm step devices (Figure 2.6A), Tg was almost completely stopped at the height step. In devices with 18 nm and 19.5 nm steps, some Tg reached the ends of the channels while some was trapped at the height steps as shown in Figure 2.6B-C. In

nanochannels with 22 nm and 29 nm height steps (Figure 2.6D-E), Tg largely passed through to the end of the channels. A clear change in trapping behavior is observed as the height step goes from smaller than the protein diameter to considerably larger than the diameter.
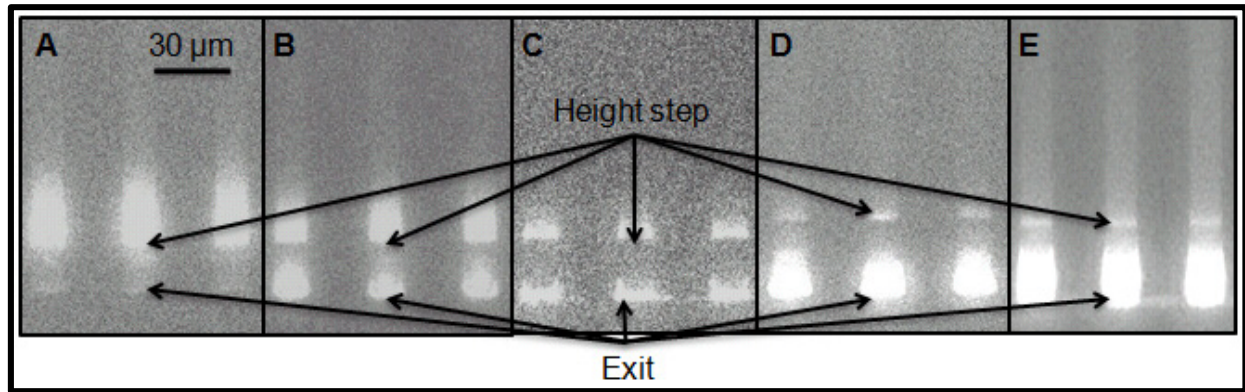
Figure 2.6 Images showing a change in trapping pattern of Tg as height step is increased. (A) 15 nm, (B) 18 nm, (C) 19.5 nm, (D) 22 nm, and (E) 29 nm.

2.3.3 T/t ratio as a function of protein concentration

Average T/t ratios obtained for all five proteins in five height step devices were plotted as a function of protein concentration as shown in Figure 2.7. These data show that trapping behavior of the proteins was largely independent of concentration, except in a few instances for Hb, Ct and Tg, usually at the highest concentration (1 mg/mL). This could be a function of a particular protein's propensity to stick to itself or to the channel surface. Alternatively, concentration-dependent trapping could also possibly be explained by the "keystone effect" (Figure 2.8), wherein a group of particles acts as a single larger particle that can block the passage of individual particles.[29-30] The formation of a "keystone" will depend on various factors such as protein size, concentration, and interactions with the walls or other proteins. Although the overall effect of concentration on the T/t ratio was relatively modest, to avoid this complicating factor, it may be best to operate devices at or below concentrations of 0.5 mg/mL. Alternatively, my colleague has

previously shown that clogging at height steps can be addressed by applying an oscillating voltage along the channels.[30]
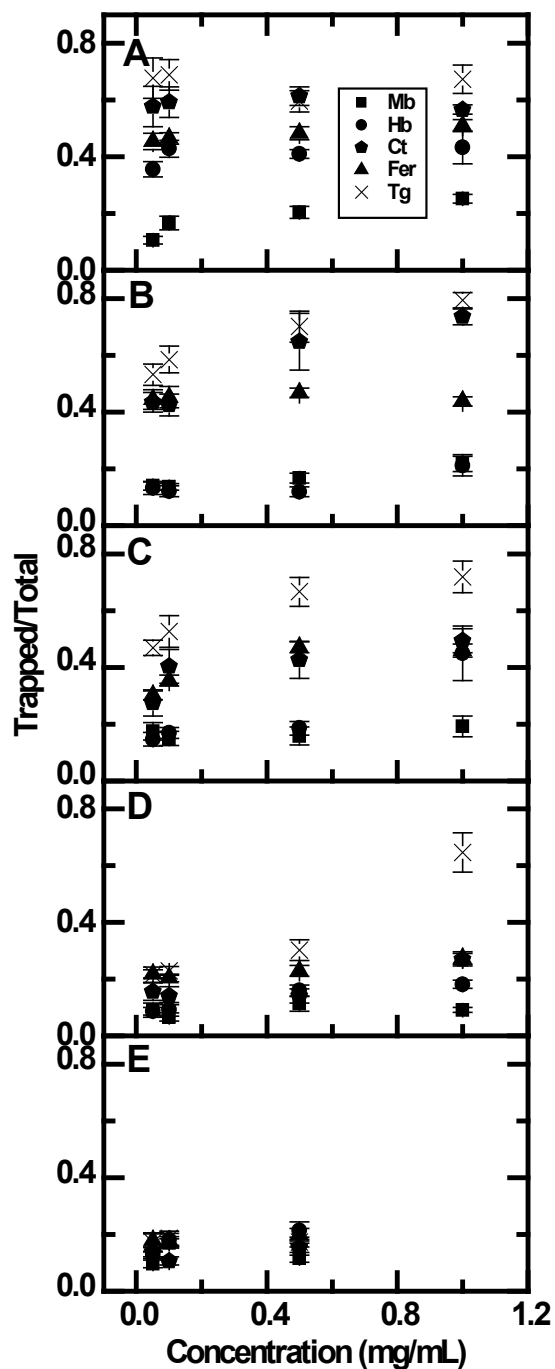
Figure 2.7 Plots of variation of trapped/total ratio with protein concentration in (A) 100-15 nm, (B) 100-18 nm, (C) 100-19.5 nm, (D) 100-22 nm, and (E) 100-29 nm devices. 1 mg/mL data are not shown in (E) because the length of the plug of fluorescent material that accumulated at the exit extended back beyond the height step. The error bars indicate plus or minus one standard deviation of the mean.
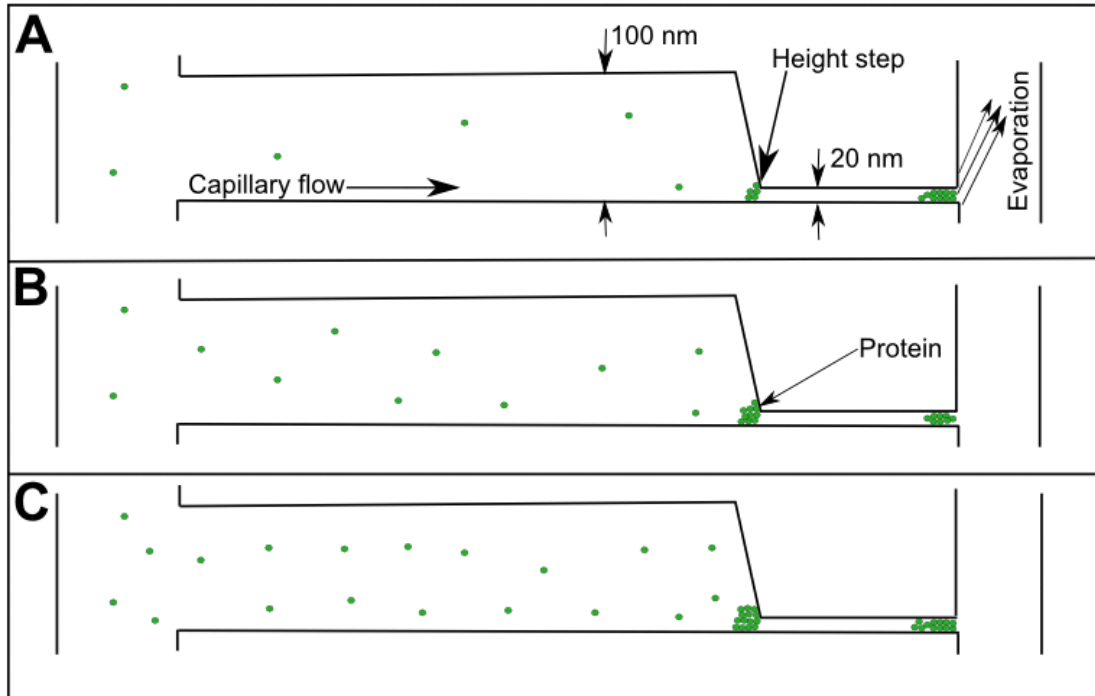
Figure 2.8 Schematic showing concentration dependent trapping of a protein smaller than a height step. (A) At low concentration, most proteins pass. (B) At medium concentration, some proteins stop and some pass. (C) At high concentration, more proteins are trapped.

2.3.4 T/t ratio versus protein size

The T/t ratio for different step heights was plotted against protein size as shown in Figure 2.9. Figure 2.9A shows that the T/t ratio followed a general upward trend as protein size increased from 3.5 nm to 17 nm in 100-15 nm devices. In Figure 2.9B, the smaller proteins (Mb and Hb) show a low T/t ratio for 100-18 nm height steps, and higher T/t ratios were observed for Ct, Fer and Tg. Figure 2.9C shows a similar trend to Figure 2.9B for trapping as a function of protein size. In Figure 2.9D the T/t ratio is low for all data points except for 1 mg/mL Tg. Finally, Figure 2.9E shows a T/t ratio that is independent of protein size in 100-29 nm devices, as approximately the same (low) T/t ratio was obtained for all protein sizes and concentrations. Importantly, a clear protein size dependent change in trapping is observed as the height step is altered. This height step

and protein size correlation demonstrates that size-specific protein trapping can be accomplished in these nanofluidic systems. Moreover, this correlation study provides valuable information for developing and evaluating a model to predict the trapping of proteins at different height steps as described below.
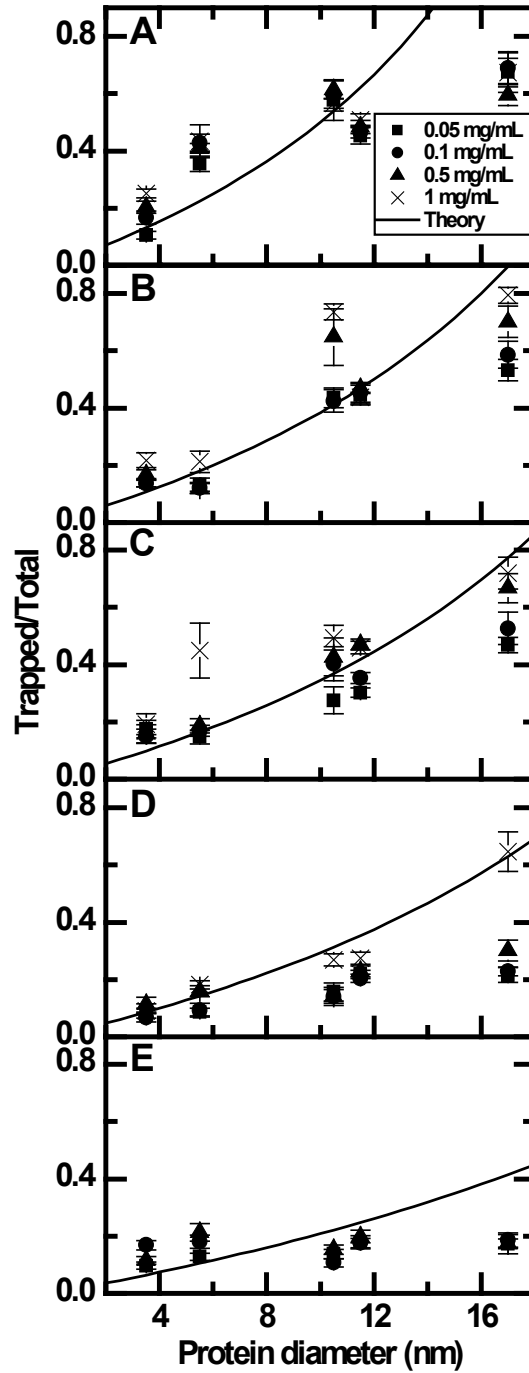
Figure 2.9 Plots of variation of trapped/total ratio with protein diameter in (A) 100-15 nm, (B) 100-18 nm, (C) 100-19.5 nm, (D) 100-22 nm, and (E) 100-29 nm devices. The solid lines plot the predicted T/t ratio as a function of protein diameter, as derived in equation (2.11). The error bars indicate plus or minus one standard deviation of the mean.

2.3.5 Trapping model

A model was derived to predict the trapping of a rigid spherical particle at a nanoscale height step, leveraging an earlier study by Giddings et al.[31] on the equilibrium distribution of rigid spheres in a porous network. An equilibrium partition constant, K, across both sides of an opening for a rigid spherical particle approaching a gap between two parallel plates can be given as

$$K = \frac{A_{available}}{A_{pore}} \tag{2.1}$$

where $A_{available}$ is the area available to the particle inside the pore, and A_{pore} is the overall area of the pore. For a slit opening and a spherical particle,

$$A_{pore} = WH \tag{2.2}$$

where W is the slit opening width and H is the height of the slit.

$$A_{available} = W(H - D) \tag{2.3}$$

where D is the particle diameter. Substituting (2.3) and (2.2) into (2.1) yields

$$K = 1 - \frac{D}{H} \tag{2.4}$$

These equations apply to a slit geometry; however, my devices have a step, rather than a slit geometry (a slit has a step from both the top and bottom surfaces). For the step model A_{pore} is further reduced because the bottom wall constrains the lower position of the particle on either side of the height step (see Figure 2.1E-F), effectively reducing the pore height by the radius of the particle. Therefore, the effective area of the pore for a step geometry is given by

$$A_{pore} = (H - D/2)W \tag{2.5}$$

Combining equations (2.1), (2.3) and (2.5) yields the partition constant for a nanochannel with a height step,

$$K = \frac{H - D}{H - D/2} \tag{2.6}$$

Now, the particle partitioning at the nanoscale opening can be viewed having an entropic energy barrier (E_b) given as

$$E_b = -k_B T \ln(K) \tag{2.7}$$

where k_B is the Boltzmann constant and T is the temperature in Kelvin.

The probability for a particle to pass the barrier (P_p) can be given as

$$P_p = \frac{\text{Passed particles}}{\text{Total particles}} = e^{\frac{-E_b}{k_B T}} \tag{2.8}$$

Substituting equation (2.7) into equation (2.8) yields

$$K = \frac{\text{Passed particles}}{\text{Total particles}} \tag{2.9}$$

The trapped particles (T) are given by

$$T = 1 - \text{Passed particles} \tag{2.10}$$

Finally, substituting equations (2.6) and (2.10) into equation (2.9) yields

$$\frac{T}{t} = \frac{D/2}{H - D/2} \tag{2.11}$$

Equation (2.11) gives a theoretical prediction of the correlation between the fraction of trapped particles and particle size (for a given step height). This model can be used to predict the trapping of spherical particles in my nanosieving devices if H and D are known, as they are for these devices

and proteins. Moreover, the measured T/t ratio can be used to determine D for an unknown nanostructure for a given height step. I plotted equation (2.11) along with my experimental data in Figure 2.9. This model fits quite well with the results obtained in my nanosieving systems for smaller height steps (15-20 nm), with somewhat greater deviations at larger height steps (22 and 29 nm). There are several possible reasons for the observed differences between theoretical and experimental data. The proteins used in these experiments are not exactly spherical and are somewhat deformable compared to rigid spheres. There is also some interaction among protein molecules, and between proteins and the channel walls, which could affect protein trapping. Finally, unlike with Giddings' theory, in our experiments the proteins have a directional velocity component towards the nanosieve opening due to capillary flow, which should increase the chance of a protein passing through the opening, compared to diffusion alone. I also note that flow eddies that might form at the height steps are not a significant source of protein trapping at height steps in my devices.

2.3.6 Buffer ionic strength effect on protein trapping

Altered trapping behavior of proteins in nanosieving devices was observed when buffer ionic strength was changed, resulting in a modified EDL thickness. The EDL is inversely related to the ionic strength and influences the effective cross-sectional area of a channel. In Figure 2.10, the trapping results for Tg in different buffer ionic strengths in 100-22 nm height step channels are shown. Almost all Tg was trapped at the 22 nm height step for 1 and 10 mM ionic strength (Figure 2.10A-B). At 50 mM ionic strength, Tg equally distributed at the height step and exit (Figure 2.10C). However, Figure 2.10D shows that most of the Tg passed through the 22 nm height step on increasing the ionic strength to 100 mM. Overall, the amount of Tg passing through the height step increased as buffer ionic strength was changed from 1 to 100 mM. Similarly, Ct and Tg were

tested in height step devices and average T/t fluorescence ratios were plotted as a function of buffer ionic strength (Figure 2.11). A decrease in T/t ratios was observed as the buffer ionic strength was increased, resulting from the reduced EDL thickness. Figure 2.11B shows that the T/t ratio for Tg in a 100-29 nm device decreased compared to in the 100-22 nm device in Figure 2.11A. In Figure 2.11A, the Tg size is only 23% smaller than the 22 nm height step; therefore, Tg was trapped even at the highest buffer ionic strength. On the other hand, in Figure 2.11B, the Tg size is 41% smaller than the 29 nm height step, and most of Tg passed to the exit on increasing buffer ionic strength above 50 mM, although a slight increase in T/t ratio was observed when ionic strength was changed from 50 to 100 mM. This unexpected behavior could result from variability in nanochannel height. Furthermore, Ct showed lower T/t ratios in Figure 2.11C than Tg in Figure 2.11A because the 22 nm height step is more than double the diameter of Ct. In summary, protein flow through a height step in a nanochannel is dependent on buffer ionic strength. Buffer ionic strength effects on protein trapping can be avoided by using high buffer ionic strengths, as EDL thickness decreases below 1 nm above 100 mM ionic strength.
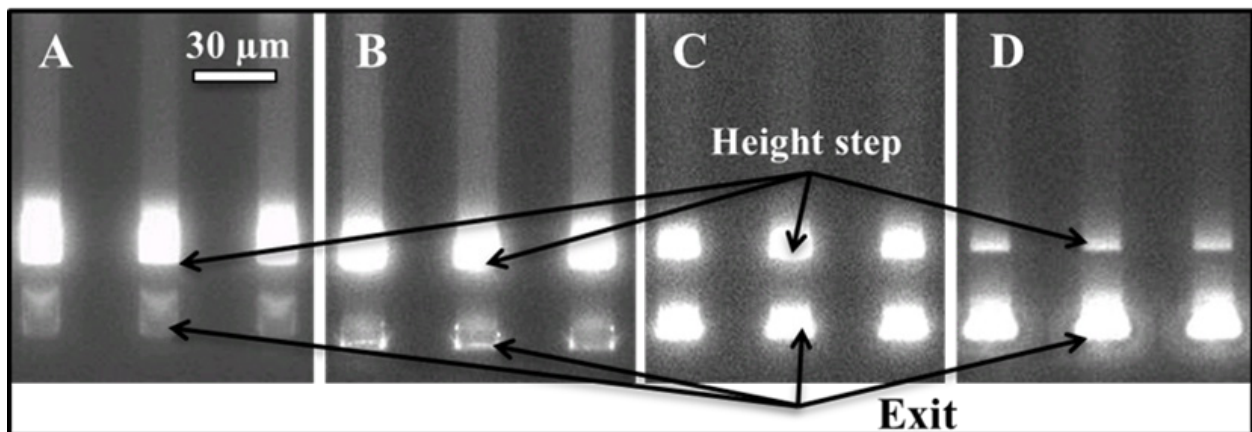
Figure 2.10 Fluorescence images showing the trapping of 0.5 mg/mL Tg in (A) 1 mM, (B) 10 mM, (C) 50 mM, and (D) 100 mM ionic strength buffer, in 100-22 nm height step devices.
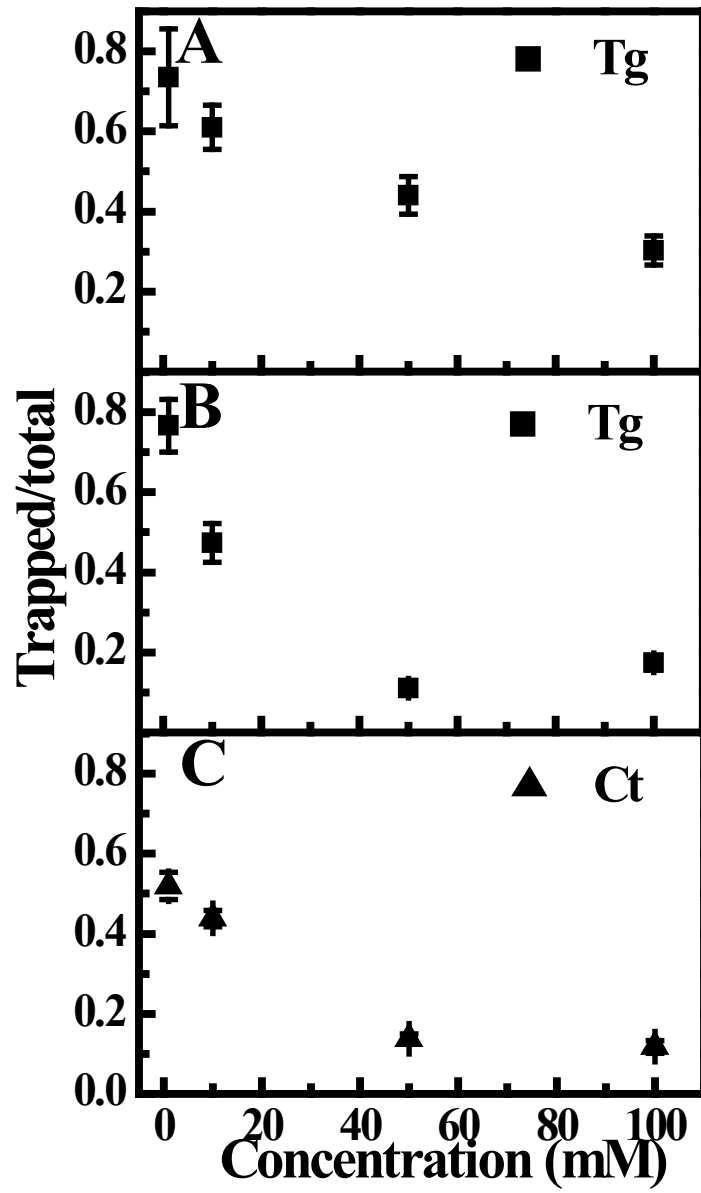
Figure 2.11 Plots of variation of T/t ratios with buffer ionic strength. (A) Tg trapping in 100-22 nm height step devices. (B) Tg trapping in 100-29 nm height step devices. (C) Ct trapping in 100-22 nm height step devices.

2.4 REFERENCES

1.   Vinayavekhin, N.; Homan, E. A.; Saghatelian, A., Exploring disease through metabolomics. *ACS Chem. Biol.* **2009,** *5*, 91-103.

2.   Vlahou, A.; Fountoulakis, M., Proteomic approaches in the search for disease biomarkers. *J. Chromatogr. B* **2005,** *814*, 11-19.

3.   Hoorn, E. J.; Pisitkun, T.; Zietse, R.; Gross, P.; Frokiaer, J.; Wang, N. S.; Gonzales, P. A.; Star, R. A.; Knepper, M. A., Prospects for urinary proteomics: Exosomes as a source of urinary biomarkers. *Nephrology* **2005,** *10*, 283-290.

4.   Perrillo, R.; Tamburro, C.; Regenstein, F.; Balart, L.; Bodenheimer, H.; Silva, M.; Schiff, E.; Bodicky, C.; Miller, B.; Denham, C., Low-dose, titratable interferon alfa in decompensated liver disease caused by chronic infection with hepatitis B virus. *Gastroenterology* **1995,** *109*, 908-916.

5.   Levine, G. N.; Keaney Jr, J. F.; Vita, J. A., Cholesterol reduction in cardiovascular disease—clinical benefits and possible mechanisms. *New Engl. J. Med.* **1995,** *332*, 512-521.

6.   Filipe, V.; Hawe, A.; Jiskoot, W., Critical evaluation of Nanoparticle Tracking Analysis (NTA) by NanoSight for the measurement of nanoparticles and protein aggregates. *Pharm. Res.* **2010,** *27*, 796-810.

7.   Skoog, D. A.; Holler, F. J.; Crouch, S. R., *Principles of Instrumental Analysis*. 6th ed.; Thomson Brooks/Cole: Belmont, CA, **2007**.

8.   Baalousha, M.; Stolpe, B.; Lead, J., Flow field-flow fractionation for the analysis and characterization of natural colloids and manufactured nanoparticles in environmental systems: a critical review. *J. Chromatogr. A* **2011,** *1218*, 4078-4103.

9.   Ersahin, M. E.; Ozgun, H.; Dereli, R. K.; Ozturk, I.; Roest, K.; van Lier, J. B., A review on dynamic membrane filtration: materials, applications and future perspectives. *Bioresource Technol.* **2012,** *122*, 196-206.

10.   Edelstein, C.; Pfaffinger, D.; Scanu, A. M., Advantages and limitations of density gradient ultracentrifugation in the fractionation of human serum lipoproteins: role of salts and sucrose. *J. Lipid Res.* **1984,** *25*, 630-637.

11.   Krauss, R. M.; Burke, D. J., Identification of multiple subclasses of plasma low density lipoproteins in normal humans. *J. Lipid Res.* **1982,** *23*, 97-104.

12.   Warnick, G. R.; McNamara, J. R.; Boggess, C. N.; Clendenen, F.; Williams, P. T.; Landolt, C. C., Polyacrylamide gradient gel electrophoresis of lipoprotein subclasses. *Clin. Lab. Med.* **2006,** *26*, 803-846.

13.   Prakash, S.; Piruska, A.; Gatimu, E. N.; Bohn, P. W.; Sweedler, J. V.; Shannon, M., Nanofluidics: systems and applications. *IEEE Sens. J.* **2008,** *8*, 441-450.

14.   Duan, C.; Wang, W.; Xie, Q., Review article: Fabrication of nanofluidic devices. *Biomicrofluidics* **2013,** *7*, 026501.

15.   Menard, L. D.; Ramsey, J. M., Fabrication of sub-5 nm nanochannels in insulating substrates using focused ion beam milling. *Nano Lett.* **2010,** *11*, 512-517.

16.   Eijkel, J. C.; Van Den Berg, A., Nanofluidics: what is it and what can we expect from it? *Microfluid. Nanofluid.* **2005,** *1*, 249-267.

17.   Han, J.; Craighead, H. G., Separation of long DNA molecules in a microfabricated entropic trap array. *Science* **2000,** *288*, 1026-1029.

18.   Wang, Y.-C.; Stevens, A. L.; Han, J., Million-fold Preconcentration of Proteins and Peptides by Nanofluidic Filter. *Anal. Chem.* **2005,** *77*, 4293-4299.

19.   Tegenfeldt, J. O.; Prinz, C.; Cao, H.; Chou, S.; Reisner, W. W.; Riehn, R.; Wang, Y. M.; Cox, E. C.; Sturm, J. C.; Silberzan, P., The dynamics of genomic-length DNA molecules in 100-nm channels. *PNAS* **2004,** *101*, 10979-10983.

20.   Schoch, R. B.; Han, J.; Renaud, P., Transport phenomena in nanofluidics. *Rev. Mod. Phys.* **2008,** *80*, 839.

21.   Chen, X.; Guo, Z.; Yang, G.-M.; Li, J.; Li, M.-Q.; Liu, J.-H.; Huang, X.-J., Electrical nanogap devices for biosensing. *Mater. Today* **2010,** *13*, 28-41.

22.   Pu, Q.; Yun, J.; Temkin, H.; Liu, S., Ion-enrichment and ion-depletion effect of nanochannel structures. *Nano Lett.* **2004,** *4*, 1099-1103.

23.   Papadopoulos, S.; Jürgens, K. D.; Gros, G., Protein diffusion in living skeletal muscle fibers: dependence on protein size, fiber type, and contraction. *Biophys. J.* **2000,** *79*, 2084-2094.

24.   Stewart, M.; Laker, M.; Dyer, R.; Game, F.; Mitcheson, J.; Winocour, P.; Alberti, K., Lipoprotein compositional abnormalities and insulin resistance in type II diabetic patients with mild hyperlipidemia. *Arterioscl. Throm. Vas. Biol.* **1993,** *13*, 1046-1052.

25.   Bruns, R. R.; Palade, G. E., Studies on blood capillaries II. Transport of ferritin molecules across the wall of muscle capillaries. *J. Cell Biol.* **1968,** *37*, 277-299.

26.   Kahook, M. Y.; Liu, L.; Ruzycki, P.; Mandava, N.; Carpenter, J. F.; Petrash, J. M.; Ammar, D. A., High-molecular-weight aggregates in repackaged bevacizumab. *Retina* **2010,** *30*, 887-892.

27.   Hamblin, M. N.; Xuan, J.; Maynes, D.; Tolley, H. D.; Belnap, D. M.; Woolley, A. T.; Lee, M. L.; Hawkins, A. R., Selective trapping and concentration of nanoparticles and viruses in dual-height nanofluidic channels. *Lab Chip* **2010,** *10*, 173-178.

28.   Bergna, H. E.; Roberts, W. O., *Colloidal silica: fundamentals and applications*. CRC Press: **2005**; Vol. 131, p 944.

29.   Pumera, M., Microchip-based electrochromatography: designs and applications. *Talanta* **2005,** *66*, 1048-1062.

30.   Xuan, J.; Hamblin, M. N.; Stout, J. M.; Tolley, H. D.; Maynes, R. D.; Woolley, A. T.; Hawkins, A. R.; Lee, M. L., Surfactant addition and alternating current electrophoretic oscillation during size fractionation of nanoparticles in channels with two or three different height segments. *J. Chromatogr. A* **2011,** *1218*, 9102-9110.

31.   Giddings, J. C.; Kucera, E.; Russell, C. P.; Myers, M. N., Statistical theory for the equilibrium distribution of rigid molecules in inert porous networks. Exclusion chromatography. *J. Phys. Chem.* **1968,** *72*, 4397-4408.

3. INCREASING PROTEIN SIGNAL USING HEAT-TREATED THIN-FILM MICROFABRICATED NANOCHANNELS

3.1 INTRODUCTION

Proteins are biological macromolecules involved in many physiological functions, and are formed by the bio-polymerization of amino acids.[1] Amino acids define the biological, physical and chemical properties of proteins.[2-3] For example, protein surface charges are the result of amino acid functional groups. In protein analysis, adsorption on surfaces is a common problem. Protein adsorption in nanofluidics leads to loss of analyte for detection, changes in surface properties, and potentially blockage at the channel entrance through the "keystone effect" described in Section 2.3.3,[4] all of which result in lower protein signal. There are four fundamental mechanisms of protein interaction with surfaces: ionic or electrostatic interaction, hydrogen bonding, hydrophobic interaction, and charge-transfer or donor/acceptor interactions.[5] Electrostatic interaction of charged amino acid residues in proteins[6-7] can cause adsorption and create problems in protein analysis.

In Chapter 2, silica-based nanochannels were used to study the correlation between protein size and ability to pass through channel constrictions. Silica surfaces have silanol (Si–OH) groups on the surface (4.6 groups/nm^2)[8] which are weakly acidic (pKa 4.5).[9] At pH values above 4, these silanol groups are deprotonated to silanoate groups (Si–O$^-$). This negatively charged silica surface can interact electrostatically with positively charged (basic) proteins which results in their adsorption.[10-11] On a silica surface, adjacent silanol groups can fuse together through a dehydration reaction to form siloxane (Si-O-Si) bridges, resulting in a reduced surface density of silanol groups. Temperature plays an important role in the conversion of surface silanol groups to siloxanes.[8] The number of surface silanol groups can be reduced to half or none by heating under vacuum to 400

ºC or 1200 ºC, respectively. However, silanol groups reform when a silica surface contacts moisture or aqueous solution. Silanol groups also render silica surfaces hydrophilic, which is important in the filling of nanochannels by capillary action. Therefore, partial elimination of silanol groups can minimize protein adsorption while maintaining surface hydrophilicity.

Electrostatic adsorption of proteins can be reduced by acid/base treatment or surface coating. For example, a silica surface can be rendered completely charge free by decreasing the solution pH below 2. However, in my method, low pH is not desirable because fluorescence on the labeled proteins is quenched. There are additional procedures available which can be used to reduce protein adsorption, such as dynamic or permanent surface coating.[12-13] Poly(ethylene glycol) is an example of a coating polymer used to minimized protein adsorption on oxide surfaces.[11] For my size-based analysis of proteins in nanochannels, the use of buffer additives can alter the protein structure, which could change trapping behavior at nanochannel height steps, block nanochannels, or decrease experimental reproducibility.

Protein adsorption remains a problem for nanofluidic systems, because current methods to reduce non-specific adsorption are complicated or lack reproducibility. In this chapter, a new method to reduce protein adsorption by heating devices with nanochannels to 250 ºC is described. This method removes surface-adsorbed water molecules and reduces the surface silanol group density through dehydration to siloxane bridges. This concept is first studied with hemoglobin in heat-treated and untreated 100-15 nm height step devices. The reduction in protein adsorption is observed through an increase in the intensity of protein signal at channel exits. Because Ta_2O_5 has similar surface chemistry to silica,[14-15] nanochannels made in Ta_2O_5 are also tested for the effects of heat treatment on protein signal.

3.2 MATERIALS

Hemoglobin (Hb) and catalase (Ct) from Sigma-Aldrich (St. Louis, MO), see Table 2.1, were labeled with fluorescein isothiocyanate (FITC, Invitrogen, Eugene, OR) and processed as described in Chapter 2.2.1. The final stock concentration of processed protein solution was measured using a Nanodrop spectrophotometer (ND-1000, Wilmington, DE), and solutions were stored at 4 °C until used. Before experiments, each protein solution was vortexed and volumetrically diluted to 0.5 mg/mL in 100 mM Tris-HCl buffer (pH 8.3), containing 1 mM sodium dodecyl sulfate (Shelton Scientific, Peosta, IA) and 0.12% v/v Triton X-100 (Sigma-Aldrich) as surfactants.

3.3 EXPERIMENTAL

3.3.1 Single-height Ta_2O_5 and SiO_2 nanochannel fabrication

The 100 nm tall nanochannels were fabricated to study the effect of heat treatment on protein signal. The fabrication recipe was adapted from the one described in Section 2.2.2, and involved use of UV photolithography, thin metal film deposition, plasma enhanced chemical vapor deposition (PECVD), and wet and dry etching to make single-height nanochannel devices on a 4" Si wafer. SiO_2 and Ta_2O_5 were used to form the nanochannel walls. Figure 3.1 shows single-height Ta_2O_5 nanochannel fabrication steps. A ~100 nm layer of Ta_2O_5 was sputtered on a clean 4" Si <100> wafer (Nova Electronic Materials, Flower Mound, TX) using a Denton sputtering system (Denton Vacuum, Moorestown, NJ); then, a ~100 nm layer of Al was deposited using e-beam evaporation to define the nanochannel height (Figure 3.1A). Photoresist (AZ 3330, AZ Electronic Materials, Branchburg, NJ) was spun on to make a uniform layer on Al (Figure 3.1B). Photoresist was patterned using UV photolithography to define the nanochannel core lines (Figure 3.1C). Exposed Al was etched in Al etchant (Type A, Transene, Danvers, MA) at 50 °C until Al was

removed (~2 min), and then photoresist was dissolved in acetone and 2-propanol (Figure 3.1D). Al core lines were covered with ~500 nm of sputtered Ta_2O_5 to form the side walls and tops of the nanochannels (Figure 3.1E). A 3-µm-thick capping layer of SiO_2 was next deposited on the Ta_2O_5 using PECVD, followed by evaporation of ~300-nm-thick Cr and patterning of AZ 3330 photoresist to define injection and exit reservoirs as illustrated in Figure 3.1F. Exposed Cr was removed using Cr etchant (OMG Cyantek, Fremont, CA), and the uncovered SiO_2/Ta_2O_5 layer was anisotropically etched down to Si in a CF_4/O_2 plasma using a Trion RIE/ICP etcher (Trion Technology, Clearwater, FL). This resulted in exposure of channel ends in the reservoirs (Figure 3.1G). After that, the remaining Cr was removed using Cr etchant. Al core lines were etched in aqua regia at 130 ºC overnight to remove the sacrificial cores and open up the nanochannels, which were then soaked in deionized water for 4-6 h (Figure 3.1H). Finally, the hollow nanochannels were treated with Nanostrip (OMG Cyantek) overnight at 90 ºC, followed by an overnight soak in deionized water. Then, devices were removed from the water and baked at 80 and 120 ºC for 10 min each, and stored in a Petri dish. SiO_2 nanochannels were also fabricated, largely following the same procedure but with the following changes. First, the Ta_2O_5 layers in Figure 3.1 were replaced with PECVD-deposited SiO_2; also, Cr deposition and removal steps were omitted in Figure 3.1F-G. Finally, the SiO_2 layer was etched isotropically in buffered oxide etchant (Transene) to make injection and waste reservoirs in Figure 3.1G. I also fabricated 100-15 nm height-step channels as described in Chapter 2.2.2 for use in preliminary experiments.
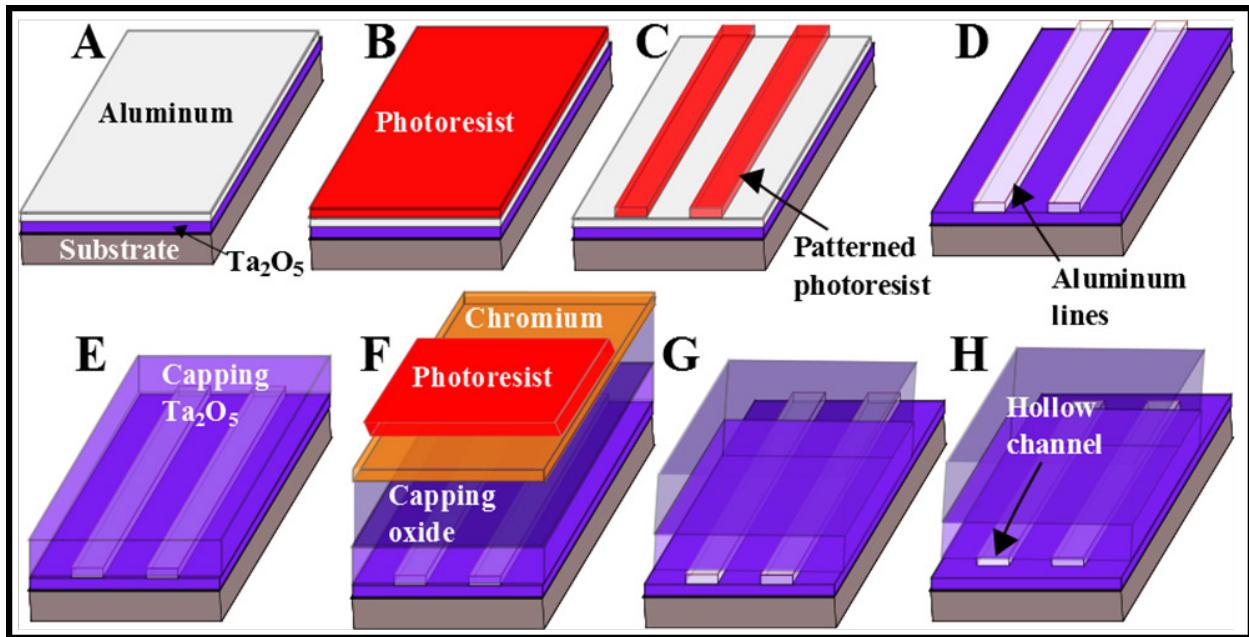
Figure 3.1 Fabrication scheme for single-height Ta_2O_5 nanochannels. (A) 100 nm of Ta_2O_5 is sputtered on a Si wafer and then 100 nm of Al is evaporated. (B) Photoresist is spun on. (C) Photoresist is patterned using photolithography. (D) Al is etched, followed by resist stripping. (E) 500 nm of Ta_2O_5 is sputtered. (F) 3 μm of SiO_2 is deposited, followed by evaporation of 300 nm of Cr. Then, photoresist is patterned. (G) Exposed Cr is etched, and next the deprotected SiO_2 is etched in a plasma. Then, photoresist and Cr are removed. (H) Al cores are etched in aqua regia, and empty channels are treated with Nanostrip.

3.3.2 Device operation and data analysis

Devices are baked on a hot plate at 130 and 210 °C for 30 min at each temperature and then at 250 °C for 30 to 60 min before use. Device operation is described in Chapter 2.2.3. Briefly, protein solution loaded in the injection reservoir flows into the nanochannels due to capillary action, and further flow is maintained by solvent evaporation from the channel ends. In this chapter, single-height nanochannels are used; therefore, proteins only accumulate at the channel exit in these devices. The performance of untreated and heat-treated SiO_2 and Ta_2O_5 nanochannels is evaluated in terms of the increase in protein signal at the channel exit. Each trapping experiment

involves loading of 500 nL of a 0.5 mg/mL solution of Hb or Ct into the injection reservoir using a 5 µL syringe (Hamilton, Reno, NV), and recording 60 s of CCD data of protein accumulation at the exit of eleven nanochannels. The hardware and software setup used in these experiments is the same as described in Chapter 2.2.3. Trapping experiments are performed in both heat-treated and untreated devices. The "measure hyperstack" free plug-in to ImageJ software (National Institutes of Health, Bethesda, MD) is used to measure the fluorescence intensity of accumulated protein at the channel exit from 0 to 60 s. For each video recording, a box (40×90 pixels^2) is drawn at the end of nine channels to encompass a region of interest showing maximum fluorescence signal to measure the average fluorescence intensity. For each experiment, the average fluorescence intensity and standard deviation from nine channels are calculated over 60 s to assess variability among nanochannels on the same device.

3.4 RESULTS AND DISCUSSION

Figure 3.2 shows initial data obtained on trapping behavior of Hb in untreated and heat-treated 100-15 nm height-step devices. A weak fluorescent signal at the exit of untreated channels was obtained 90 s after injection of Hb solution. On the other hand, a ~6x increase in Hb fluorescent signal at the exit was observed when nanosieving devices were treated with heat before use as described in Chapter 2.2.2. I hypothesized that this high-temperature bake helped in removing adsorbed water molecules from the surface and decreased the number of silanol groups. This observation led me to further explore the effect of heat treatment on protein signal at the exit of single-height SiO_2 and Ta_2O_5 nanochannels.
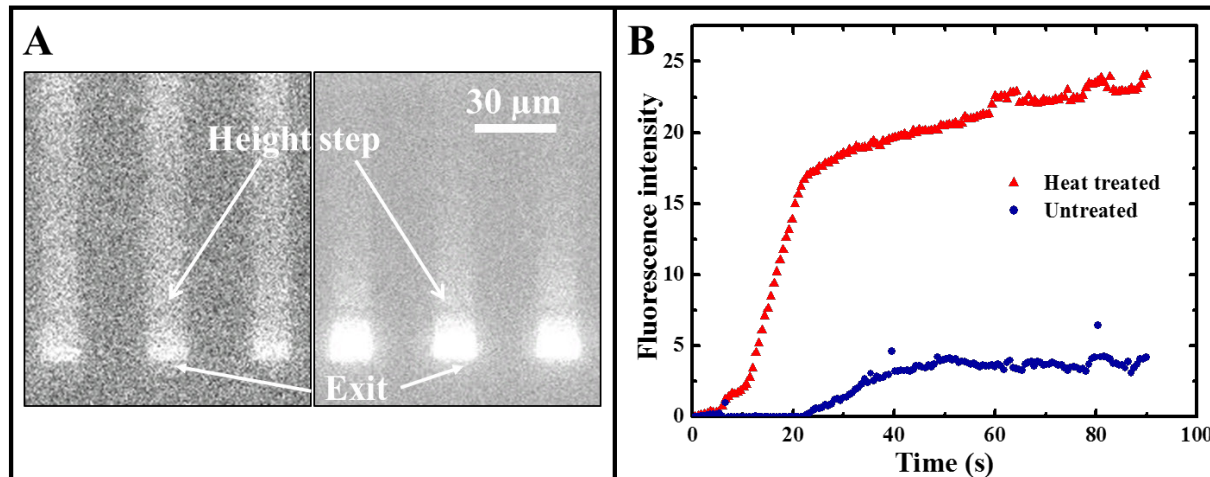
Figure 3.2 Preliminary data showing increase in Hb fluorescence signal at the exit in 100-15 nm height-step nanochannels on heat treatment. (A) Images showing the accumulation of 0.05 mg/mL Hb at the nanochannel exit in (left) untreated, and (right) heat-treated devices. (B) Plot of fluorescence intensity at the exit over time for the nanochannels in (A).

3.4.1 Increase in protein signal with heat treatment of single-height nanochannels

The effect of heat treatment of SiO_2 and Ta_2O_5 nanochannels on protein signal was evaluated using two proteins of different sizes, Hb and Ct. Multiple 100-nm-tall Ta_2O_5 and SiO_2 nanochannels were tested, and an increase in Hb and Ct accumulation at the channel exits was observed after heat treatment, as shown in Figure 3.3. The total amount of each protein reaching the exit of the nanochannel was greater after heat treatment of nanochannels before use, as shown by the increase in the fluorescence signal. More protein was observed at the SiO_2 channel exits than at the Ta_2O_5 channel exits. I attribute this to the fact that the reservoirs in SiO_2 devices were wet etched isotropically, which resulted in channels with larger openings and exits that both allowed more protein to enter into the channels and resulted in increased evaporation from the channel exits.
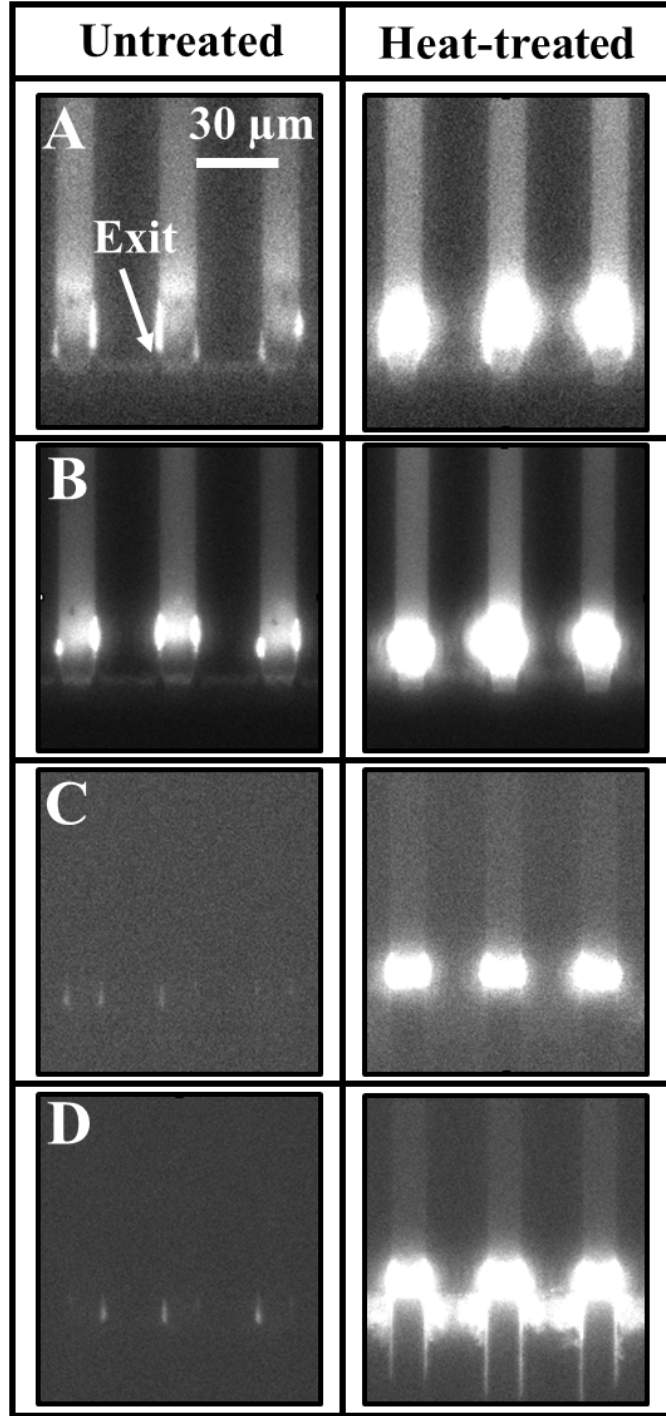
Figure 3.3 Fluorescence images of accumulated Hb and Ct at the exit in 100-nm-tall SiO_2 and Ta_2O_5 channels. (Left) untreated and (right) heat-treated channels. (A) Hb and (B) Ct in SiO_2 channels. (C) Hb and (D) Ct in Ta_2O_5 channels.

The Ta$_2$O$_5$ devices showed a consistent increase in protein signal at the exit after heat treatment of nanochannels over eight devices tested. However, the increase in protein signal after heat treatment was not always observed in SiO$_2$ devices, as shown in Figure 3.4. In this figure, Ct fluorescence signal was not much different at the exit of untreated and heat-treated nanochannels. Table 3.1 further shows that the increase in fluorescence signal in heat-treated SiO$_2$ devices was not significant compared to the signal in untreated SiO$_2$ devices. These results from SiO$_2$ devices could be attributed to irregularities in the composition of SiO$_2$ deposited using PECVD over time. Environmental factors such as humidity may be another reason for the behavior seen in SiO$_2$ chips.
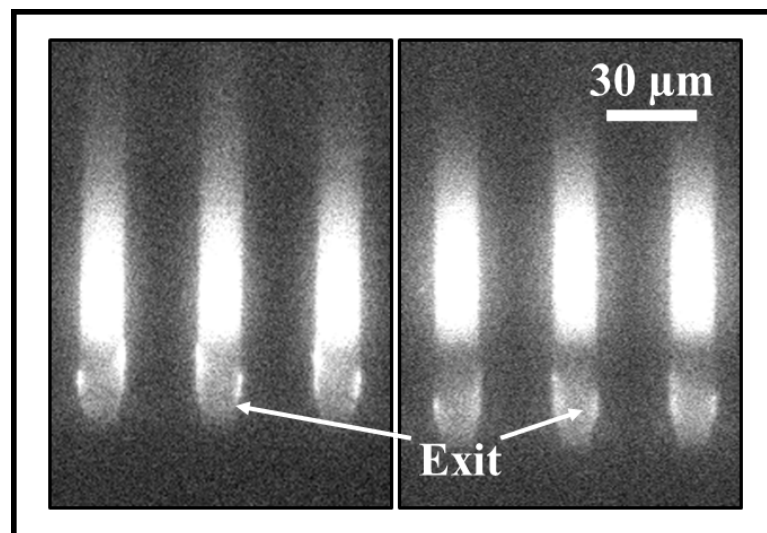
Figure 3.4 Images showing accumulation of 0.2 mg/mL Ct at the exit of channels in (left) untreated and (right) heat-treated SiO$_2$ devices.

Table 3.1 Average and standard deviation of fluorescence of Hb and Ct at the exit of seven nanochannels in untreated and heat-treated SiO_2 devices.

Protein	Concentration (mg/mL)	Average fluorescence signal	
		Untreated	Heat-treated
Hb	0.4	33±2	38±6
Ct	0.4	47±3	48±2
Ct	0.2	31±2	29±1

Figure 3.5 shows average fluorescence intensity measurements of Hb and Ct at the exits of untreated and heat-treated SiO_2 and Ta_2O_5 channels as a function of time. Heat-treated SiO_2 devices showed 3.2x and 2.5x greater signal at the exit for Hb and Ct, respectively. In contrast, heat treatment of Ta_2O_5 devices increased the Hb and Ct signal at the channel exits by 24x and 63x, respectively. Small fluctuations in fluorescence intensity in Figure 3.5 were caused by evaporation of solvent in the injection reservoir, which retracted the meniscus in the channel and stopped the accumulation of proteins at the exit. Protein accumulation at the exit was recovered after replenishing the solution in the injection reservoir, seen as an increase in intensity after the marked dips in Figure 3.5.

Both SiO_2 and Ta_2O_5 surfaces have –OH functional groups that can lose a proton in basic conditions and provide a negatively charged surface. Proteins typically have charges distributed on their surfaces, which can interact both with other protein molecules and channel surfaces. These combined interactions could cause sticking of proteins along the nanochannels, as well as at the channel entrance, both of which would decrease protein signal at the channel exits. When devices were heated before use, the surface –OH groups condensed to form Si–O–Si or Ta–O–Ta bridges,

80

reducing the surface charge density. This reduction in surface charge should result in decreased electrostatic interaction between proteins and the dry channel surfaces, leading to more protein signal at the channel exits, as observed. This effect would occur only when protein hits a dry channel surface because silanol groups reform on contact with aqueous solutions.
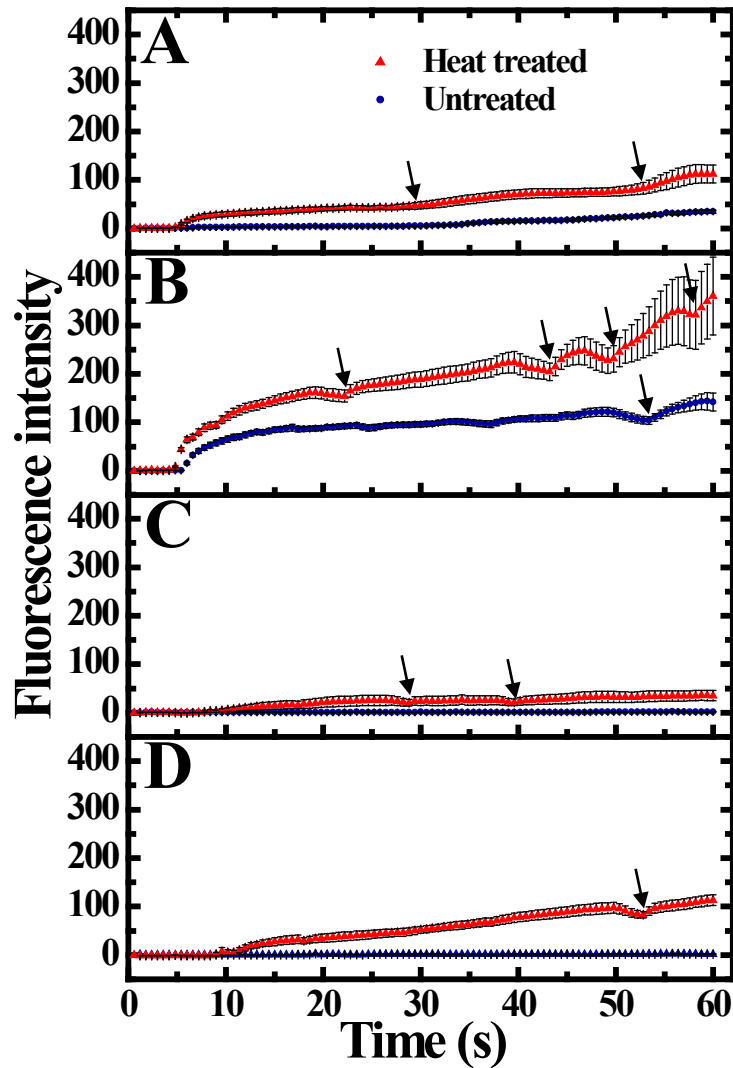
Figure 3.5 Plots of fluorescent intensity at the exit over time for untreated and heat-treated channels in Figure 3.3. (A) Hb and (B) Ct in SiO2 channels. (C) Hb and (D) Ct in Ta2O5 channels. Arrows mark times where solution was added into injection reservoirs.

3.5 REFERENCES

1.   Creighton, T. E., *Proteins: Structures and Molecular Properties*. 2nd ed.; **1993**.

2.   Gutteridge, A.; Thornton, J. M., Understanding nature's catalytic toolkit. *Trends Biochem. Sci.* **2005,** *30*, 622-9.

3.   Alberts, B.; Johnson, A.; Lewis, J.; Raff, M.; Roberts, K.; Walter, P., *Molecular Biology of the Cell-The Shape and Structure of Proteins*. 4th ed.; Garland Science: New York, **2002**.

4.   Pumera, M., Microchip-based electrochromatography: designs and applications. *Talanta* **2005,** *66*, 1048-1062.

5.   Kim, J.-H.; Yoon, J.-Y., Protein adsorption on polymer particles. *Enc. Surf. Coll. Sci.* **2002,** *1*, 4373-4381.

6.   Dee, K. C.; Puleo, D. A.; Bizios, R., An Introduction to Tissue-Biomaterial Interactions. 1st ed.; John Wiley & Sons: New Jersey, **2002**; pp 1-50.

7.   Ellingsen, J. E., A study on the mechanism of protein adsorption to TiO_2. *Biomaterials* **1991,** *12*, 593-596.

8.   Zhuravlev, L. T., The surface chemistry of amorphous silica. Zhuravlev model. *Colloids Surf. A* **2000,** *173*, 1-38.

9.   O'Reilly, J. P.; Butts, C. P.; I'Anso, I. A.; Shaw, A. M., Interfacial pH at an Isolated Silica−Water Surface. *J. Am. Chem. Soc.* **2005,** *127*, 1632-1633.

10.   Rimola, A.; Costa, D.; Sodupe, M.; Lambert, J.-F.; Ugliengo, P., Silica Surface Features and Their Role in the Adsorption of Biomolecules: Computational Modeling and Experiments. *Chem. Rev.* **2013,** *113*, 4216-4313.

11.   Kenausis, G. L.; Vörös, J.; Elbert, D. L.; Huang, N.; Hofer, R.; Ruiz-Taylor, L.; Textor, M.; Hubbell, J. A.; Spencer, N. D., Poly(l-lysine)-g-Poly(ethylene glycol) Layers on Metal Oxide

Surfaces: Attachment Mechanism and Effects of Polymer Architecture on Resistance to Protein Adsorption. *J. Phys. Chem. B* **2000,** *104*, 3298-3309.

12.   Liu, J.; Lee, M. L., Permanent surface modification of polymeric capillary electrophoresis microchips for protein and peptide analysis. *Electrophoresis* **2006,** *27*, 3533-3546.

13.   Roach, L. S.; Song, H.; Ismagilov, R. F., Controlling Nonspecific Protein Adsorption in a Plug-Based Microfluidic System by Controlling Interfacial Chemistry Using Fluorous-Phase Surfactants. *Anal. Chem.* **2005,** *77*, 785-796.

14.   Miyazaki, T.; Kim, H.-M.; Kokubo, T.; Ohtsuki, C.; Kato, H.; Nakamura, T., Mechanism of bonelike apatite formation on bioactive tantalum metal in a simulated body fluid. *Biomaterials* **2002,** *23*, 827-832.

15.   Kokubo, T.; Kim, H.-M.; Kawashita, M., Novel bioactive materials with different mechanical properties. *Biomaterials* **2003,** *24*, 2161-2175.

4. ASSESSMENT OF OFF-CHIP FLUORESCENT LABELING OF PRETERM BIRTH BIOMARKERS AND SEPARATION USING CAPILLARY AND MICROCHIP ELECTROPHORESIS

4.1 INTRODUCTION

Analytical chemistry involves separation, identification and quantification of chemical analytes of natural and artificial origin.[1] Biomolecules such as proteins, peptides, nucleic acids and carbohydrates are examples of chemical analytes of natural origin. Many biomolecules have been identified whose concentrations can be correlated with health issues. Such biomolecules are called biomarkers.[2-3] For example, there are many cancer biomarkers; carcinoembryonic antigen is used to screen for colon cancer; and α-fetoprotein, beta human chorionic gonadotropin and lactate dehydrogenase are monitored in germ cell tumors.[4] In addition, neutrophil gelatinase associated lipocalin, kidney injury molecule-1, monocyte chemotactic peptide, netrin-1, and interleukin-18 are recently found biomarkers for acute kidney injury.[5]

I am interested in preterm birth (PTB), a pregnancy complication that involves delivery before 37 weeks of gestation.[6] Many neonatal deaths and illnesses are caused by PTB. Recently, three PTB peptide biomarkers have been found, that complement six previously identified PTB biomarker proteins (see Table 4.1).[7] This panel of nine biomarkers in serum results in high sensitivity (86.5%) and specificity (80.6%) in predicting a PTB 9 weeks before contractions. Unfortunately, there is presently no simple clinical method available for early diagnosis of PTB; hence, therapeutic interventions are often too late to prevent PTB. Importantly, these nine PTB biomarkers at 28 weeks of pregnancy show promise to be used to predict risk of a subsequent PTB; with that information, steps can be taken that would help in delaying the delivery.

Table 4.1 A list of PTB biomarkers.[7]

Peptide 1	QLGLPGPPDVPDHAAYHPF
Peptide 2	NVHSAGAAGSRMNFRPGVLSSRQLGLPGPPDVPDHAAYHPF
Peptide 3	NVHSAGAAGSRM(O)NFRPGVLSSRQLGLPGPPDVPDHAAYHPF
Proteins	Ferritin, Defensin, Lactoferrin, Thrombin antithrombin, TNF-α receptor type 1, and Corticotropin-releasing factor

Liquid chromatography-mass spectrometry (LC-MS) is often used for initial identification of biomarkers,[8] but LC-MS has problems with scalability and cost. For example, LC-MS instruments are bulky and expensive, and cannot be used for point-of-care applications; additionally, the cost of completing LC-MS analyses can be high. On the other hand, microfluidics offers a promising platform for routine biomarker analysis, presenting advantages such as portability, rapidity, and point-of-care capability.[9] Microchip electrophoresis (μCE) is a powerful microfluidic separation method; it involves short analysis time, reduced reagent consumption, and ease of integration of multiple processes. Such advantages of μCE could allow rapid and sensitive analysis of PTB biomarkers at low cost.

Laser-induced fluorescence (LIF) is the most common detection method used in μCE.[10] Unfortunately, most analytes are not naturally fluorescent; therefore, they need to be derivatized with fluorophores, for example they covalently react with amine, thiol, aldehyde and other groups to form a fluorescing complex.[11] Alternatively, noncovalent labeling based on hydrophobic or ionic interactions is also possible.[12] The nine PTB biomarkers (Table 4.1) are proteins or peptides on which lysine residues and the N-terminus provide primary amine sites for fluorescent labeling. However, there are some challenges in labeling of PTB biomarkers. PTB peptides are difficult to

label in their native conformation due to unavailability of the N-terminus which may be enclosed in the peptide 3-D structure.[13] Additionally, proteins label slowly (~24 h) and form multiply-labeled isoforms that result in broad µCE peaks that might overlap with closely eluting peaks and cause problems in quantitative analysis.

In this chapter, the labeling of four PTB biomarkers is assessed using conventional CE and µCE. Peptide labeling is improved under denaturing conditions that improve access to the N-terminus. Moreover, a narrow ferritin (Fer) fluorescence peak is obtained when it is labeled only for a short duration (~20 min). Finally, a µCE protocol is developed to separate four PTB biomarkers, including the three peptides and Fer in less than 3 min. These separation procedures should be useful in the analysis of PTB biomarkers in integrated devices developed in Chapters 5-6.

4.2 MATERIALS

Silicon <100> wafers are purchased from Desert Silicon (Tempe, AZ) to prepare templates for microchannel fabrication, using photolithography and wet etching. PMMA sheets (1.5- and 3.0-mm-thick) for device fabrication are obtained from Cyro Industries (Rockaway, NJ) and cut into 2"x0.8" pieces using a laser cutter (Universal Laser Systems, Scottsdale, AZ). Peptide 1, peptide 2, and peptide 3 (see Table 4.1) are custom synthesized by GenScript (Piscataway, NJ). Fer is obtained from EMD milllipore (Billerica, MA). Sodium borate buffer (100 mM) is prepared by dissolving 155 mg of boric acid in deionized (DI) water and adjusting the pH to 10.1 with 6 M NaOH solution. Borate buffer is diluted to 20 mM, and 20 mM NaCl and 0.2% w/w hydroxypropylcellulose (HPC, Sigma-Aldrich, St. Louis, MO) are added for µCE. Fluorescein isothiocyanate (FITC) and Alexa Fluor 488 5-tetrafluorophenyl ester (ALF) are obtained from Life Technologies (Carlsbad, CA) for fluorescent labeling of peptides and Fer. Dimethyl sulfoxide

(DMSO) used in preparation of the fluorescent label stock and peptide denaturation is obtained from Sigma-Aldrich. All solutions are prepared in purified DI water filtered through a Barnstead Nanopure System (Thermo Scientific, Waltham, MA).

4.3 EXPERIMENTAL

4.3.1 PMMA device fabrication

A master mold is fabricated on a 4" Si wafer using photolithography and wet etching as shown in Figure 4.1. First, the Si wafer is oxidized in a Bruce tube furnace (Bruce Industrial Controls, New Castle, DE) to grow 500-600 nm of oxide. The oxidized Si wafer is cleaned with acetone and 2-propanol (IPA), and dried with N_2. The cleaned oxidized wafer is baked in an Ultra-Clean 100 Oven (Lab-Line, Dubuque, IA) at 150 ºC for 15-20 min. The cleaned Si wafer is primed with hexamethyldisilazane (HMDS, SPI, West Chester, PA) followed by spin coating of photoresist (S1805, Rohm and Haas, Marlborough, MA). The photoresist-coated wafer is baked at 110 ºC for 1 min and exposed to UV light through a Cr mask. The exposed Si wafer is baked at 110 ºC for 5 min and developed in MF-26A developer (Rohm and Haas) for ~2 min until clear features are formed. The developed wafer is baked at 110 ºC for 5 min to improve resist adhesion to the wafer and cleaned in an O_2 plasma (Planar Etch II, Technics, San Jose, CA) for 1 min at 150 W. Then, the unprotected oxide is etched in buffered oxide etchant (BOE, Transene, Danvers, MA) for 8-10 min until the SiO_2 is completely etched down to the Si surface. Next, photoresist is rinsed off using acetone and IPA. The Si wafer is diced into individual device templates using a diamond cutter. Diced templates are wet etched in 40% aqueous KOH solution at 70 ºC to make 18-20 μm tall features.
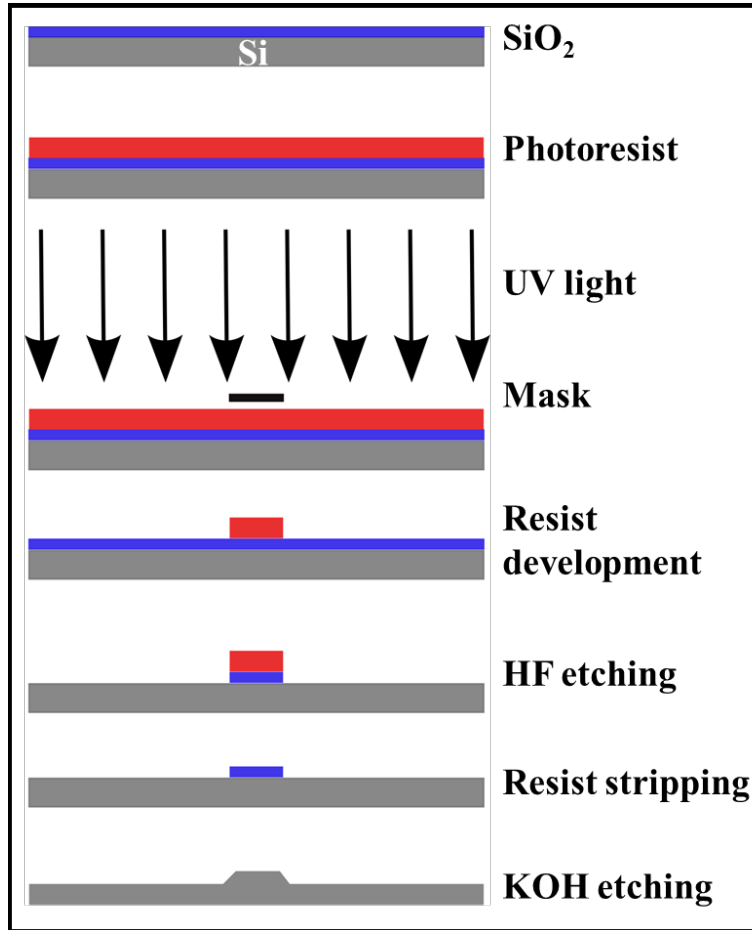
Figure 4.1 Schematic showing Si template fabrication.

Next, enclosed microchannels are made in PMMA as shown in Figure 4.2. Microchannel fabrication involves three steps: hot embossing, laser cutting, and thermal bonding. Patterns from the Si template are transferred into 1-mm-thick PMMA by hot embossing at 138 ºC for 26 min in a precision convection oven (Thermo Scientific, Asheville, NC). Reservoir holes are laser cut in 3-mm-thick PMMA, and the plate is flattened at 110 ºC for 20 min to smooth reservoir edges. Later, the flattened and imprinted PMMA pieces are aligned together and thermally bonded at 110 ºC for 23-25 min. Finally, the bonded PMMA edges are sealed chemically using acetonitrile, and DI water is flowed to test the channels.
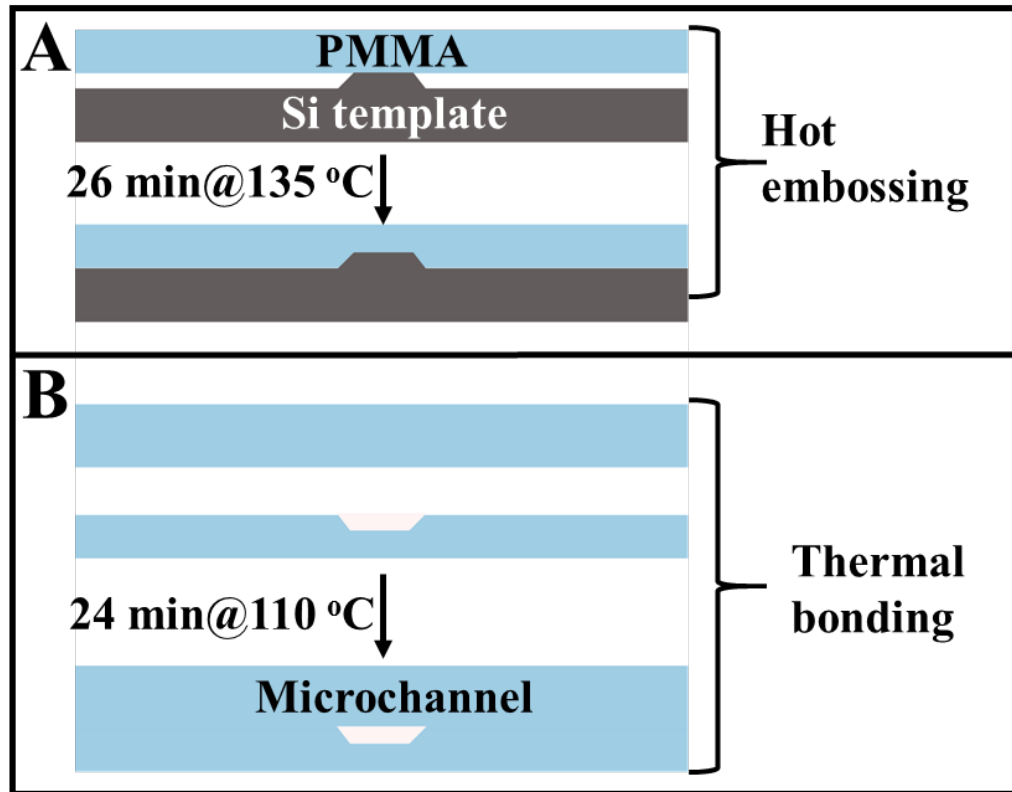
Figure 4.2 Schematic showing fabrication of PMMA microfluidic devices. (A) Hot embossing to imprint Si features on PMMA. (B) Thermal bonding to enclose microfluidic channels within the PMMA.

4.3.2 Off-chip labeling protocol

Fer is labeled with FITC as described in Chapter 2.2.1. Various additional labeling conditions were attempted for labeling PTB peptides since labeling is inefficient under the conditions used for Fer. FITC and ALF (structures shown in Figure 4.3) were used for peptide labeling with stock solutions prepared in DMSO. Fluorescent labeling conditions for all three peptides and the various parameters are given in Table 4.2. After labeling, all peptide samples were diluted in borate running buffer for conventional CE analysis. For μCE, only denatured solution of peptides 2 and 3 were filtered using a 2 kDa mass cutoff membrane filter (Millipore, Billerica, MA) in a microcentrifuge to remove excess dye. Microchip CE samples were diluted in 5 mM

borate (pH 10.1), containing 20 mM NaCl and 0.2% w/w HPC. Since a membrane filter smaller than 2 kDa mass cutoff is not available commercially, synthesized fluorescently labeled peptide 1 was used for μCE.

Table 4.2 PTB peptide labeling conditions.

Experiment	Peptide conc.	Dye conc.		Denaturing conditions	Labeling conditions†
		ALF	FITC		
Peptide 1-native	3 mM		0.5 mM		pH 10.65, 4 h @37 ºC, then overnight @4 ºC
Peptide 1-denatured	3 mM		2.5 mM	10% v/v DMSO + 5 min @95 ºC	pH 9.65, 7 h @37 ºC, then overnight @RT*
Peptide 2-native	0.8 mM	0.3 mM			pH 10.65, 4 h @37 ºC, then overnight @RT*
Peptide 2-denatured	1.2 mM		1.1 mM	10% v/v DMSO + 5 min @95 ºC	pH 9.65, 7 h @37 ºC, then overnight @RT*
Peptide 3-native A	1.9 mM	0.4 mM			pH 10.65, 4 h @37 ºC, then overnight @4 ºC
Peptide 3-native B	1.4 mM		1.3 mM		pH 10.65, 5 h @37 ºC, then overnight @RT*
Peptide 3-native C	1.9 mM		1.8 mM		pH 9.65, overnight @37 ºC
Peptide 3-denatured	2.1 mM		2 mM	10% v/v DMSO + 6 min @75 ºC	pH 9.65, 5 h @37 ºC, then overnight @RT*

† In all labeling 100 mM BCB was used. * RT: room temperature.
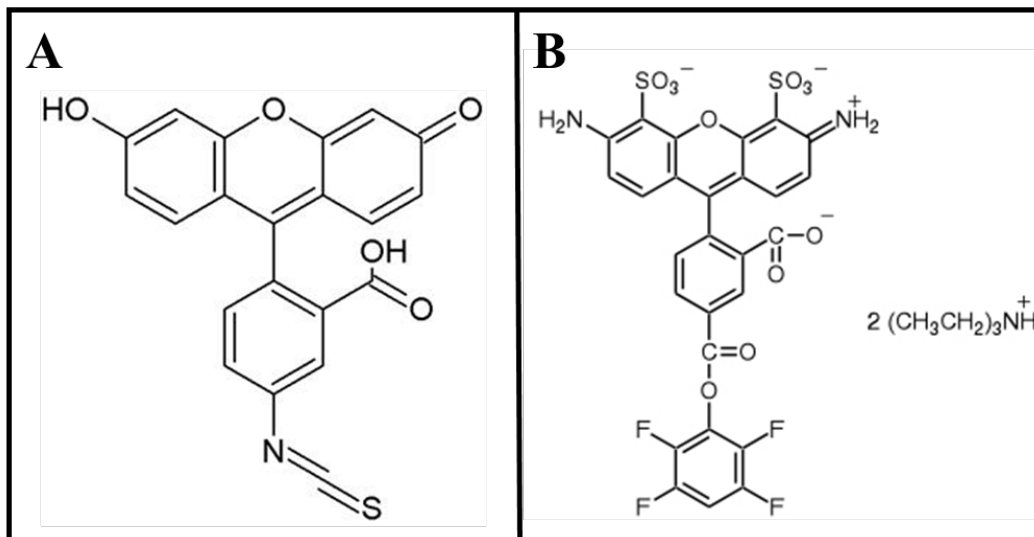
Figure 4.3 Fluorescent dye structures. (A) FITC and (B) ALF.

4.3.3 PMMA device layout and operation

Microchip electrophoretic separation of PTB biomarkers is performed in an offset "T" device fabricated in PMMA; a schematic is shown in Figure 4.4A.[14] Three different mixtures of PTB biomarkers are analyzed: Fer (10 nM) and peptide 3 (200 nM); Fer (9 nM), peptide 1 (125 nM) and peptide 3 (165 nM); and Fer (11 nM), peptide 1 (150 nM) and peptide 2 (150 nM). Each device consists of four reservoirs: sample, sample waste, running buffer, and separation waste (see Figure 4.4A). Microchip CE operation involves three steps: sample injection, plug formation, and electrophoretic separation. In this study, pinched injection is used to form the sample plug at the channel intersection.[15] Briefly, a small sample volume (~20 µL) is added in the sample reservoir, and separation buffer (20 mM borate, pH 10.1, 0.2% HPC, 20 mM NaCl) is loaded in the remaining 3 reservoirs. Then, 600 V is applied at the sample waste reservoir, while keeping the other reservoirs at ground, as shown in Figure 4.4B. This moves the negatively charged sample from the sample reservoir toward the sample waste reservoir. After ~1 min, the voltages are reconfigured (see Figure 4.4C): a small pull-back voltage (600 V) is applied to the sample and sample waste

reservoirs to pull back sample, a high voltage (1500 V) is applied at the separation waste reservoir, and the running buffer reservoir is maintained at ground. This results in the injection of the sample plug at the intersection, which leads to separation based on electrophoretic mobility as analytes go down the separation channel, as shown in Figure 4.4D. Separated analyte bands are detected using an LIF detection system, consisting of an inverted Eclipse TE 300 microscope (Nikon, Melville, NY), 488 nm diode laser (JDSU, Shenzhen, China), photomultiplier tube (PMT, Hamamatsu, Japan), low-noise preamplifier (Stanford Research Systems, Sunnyvale, CA) and custom-made voltage switching box. Data are acquired using a custom LabVIEW program. LIF detection system parameters include a PMT setting of 860 V, signal amplification of 2x, and a detection distance 2.6 cm past the intersection.
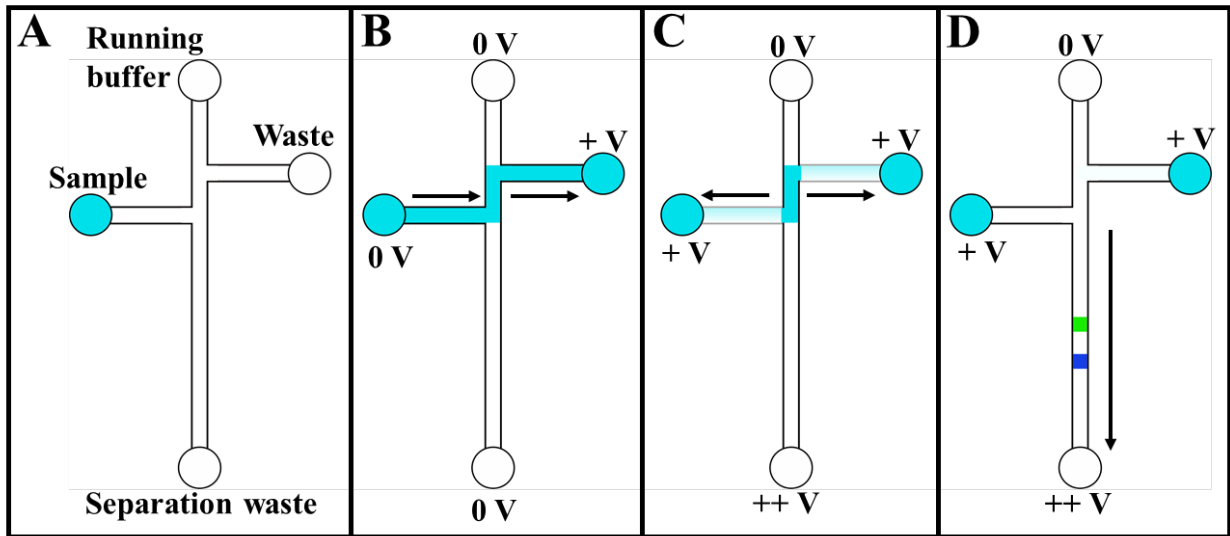

Figure 4.4 Schematic showing operation of an offset "T" µCE device. (A) Device layout. (B) Sample is injected through the intersection, and then the voltages are reconfigured, leading to (C) sample plug formation, and over time (D) electrophoretic separation.

4.3.4 Evaluation of ferritin labeling

Off-chip, time-dependent labeling of Fer with FITC and ALF is evaluated using µCE. A 500 nM Fer solution is prepared in 10 mM BCB (pH 9.8), and FITC or ALF is added to the solution at a molar ratio of 20:1. The protein-dye mixture is incubated either for 20 min or overnight at room temperature to evaluate the degree of labeling. Next, excess dye is removed using a 30 kDa cutoff membrane filter. To avoid sample loss, a maximum of two centrifugal filtrations are done. Fer stock solution concentration is measured using a Nanodrop spectrophotometer (ND-1000, Wilmington, DE) and reconstituted to 500 nM in 10 mM BCB (pH 9.8). Labeled Fer samples are separated using µCE. Microchip separation buffer is 20 mM BCB, pH 11, 20 mM NaCl, and 0.2% HPC. Sample is injected for 45 s as described in Section 4.3.3, but using 400 V and separation is performed using 1000 V. LIF is detected 1.5 cm from the intersection using a PMT setting of 970 V with 2x amplification.

4.3.5 Capillary electrophoresis separation

A P/ACE MDQ capillary electrophoresis system (Beckman Coulter, Pasadena, CA) is used to analyze off-chip labeled PTB biomarkers. The CE system is equipped with a diode array UV/Vis detector and 57-cm-long fused silica capillary with a 75 µm internal diameter and 50 cm effective separation length. All samples are prepared in CE running buffer and injected for 0.5 s using 0.5 psi. Most separations are in 50 mM borate buffer (pH 10.3) at 25.0 kV; any exceptions are noted in the figure captions.

4.4 RESULTS AND DISCUSSION

PTB biomarkers for microchip and conventional CE were labeled off-chip, enabling LIF detection during µCE. Fer has multiple labeling sites and is easy to fluorescently label with the procedure described in Chapter 2.2.1. Conversely, PTB peptides have only one primary amine labeling site (on the N-terminus), which made labeling problematic under conventional conditions. Therefore, multiple procedures were tried and labeling was assessed using benchtop CE.

Figures 4.5A-B show CE separations of fluorescent dyes (FITC and ALF) and unlabeled peptide 3, respectively. Dye peaks were symmetrical, but unlabeled peptide 3 peak had a little fronting. I compared peak heights of labeled and unlabeled peptides in all CE plots to evaluate the degree of labeling. In Figure 4.5C-D (native A and B), peptide 3 was not labeled efficiently with either ALF or FITC, but FITC labeling was better than with ALF. ALF is larger than FITC (see Figure 4.3), which could possibly cause steric hindrance to access the N-terminus. Therefore, FITC labeling was further evaluated. The extent of peptide 3 labeling was improved somewhat in comparison to Figure 4.5D by a longer time at 37 ºC as shown in Figure 4.5E, since reaction kinetics increase with temperature. Moreover, a further improvement in labeling was observed as compared to Figure 4.5E when peptide 3 was denatured before labeling (see Figure 4.5F). Denatured peptide 3 should open up access to the N-terminus for labeling. All peaks in the CE plots were baseline resolved; however, peptide peaks showed a little fronting except in Figure 4.5C.

Figure 4.5 CE separation of peptide 3 labeled with ALF and FITC under different conditions. (A) FITC (500 µM) and ALF (3.4 µM). Separation in 50 mM borate buffer, pH 10.5, 22.0 kV. (B) Unlabeled peptide 3 (50 µM). (C) Peptide 3-native A (58.0 µM). Separation in 50 mM borate buffer, pH 10.5, 22.0 kV. (D) Peptide 3-native B (50 µM), 50 mM borate buffer, pH 10.5, 20.0 kV. (E) Peptide 3-native C (50 µM). (F) Peptide 3-denatured (50 µM). Labeling conditions are in Table 4.2.

Peptide 2 labeling was also evaluated using conventional CE as shown in Figure 4.6. Figures 4.6A-B show CE separations of fluorescent dyes (FITC and ALF) and unlabeled peptide 2, respectively. Dye peaks were symmetrical, but the unlabeled peptide 2 peak had a little fronting

and an apparent unresolved impurity peak. Under native labeling conditions, the labeled peptide 2 peak height was lower than that of the remaining unlabeled peptide 2 after reaction, as seen in Figure 4.6C. Here, all peaks were resolved and symmetrical. When peptide 2 was denatured before labeling, an increase in the labeled peptide 2 peak height compared to the unlabeled one was observed as shown in Figure 4.6D, indicating that as with peptide 3, labeling efficiency is improved with denaturation. In Figure 4.6D, unlabeled and labeled peptide 2 peaks showed tailing and fronting, respectively.
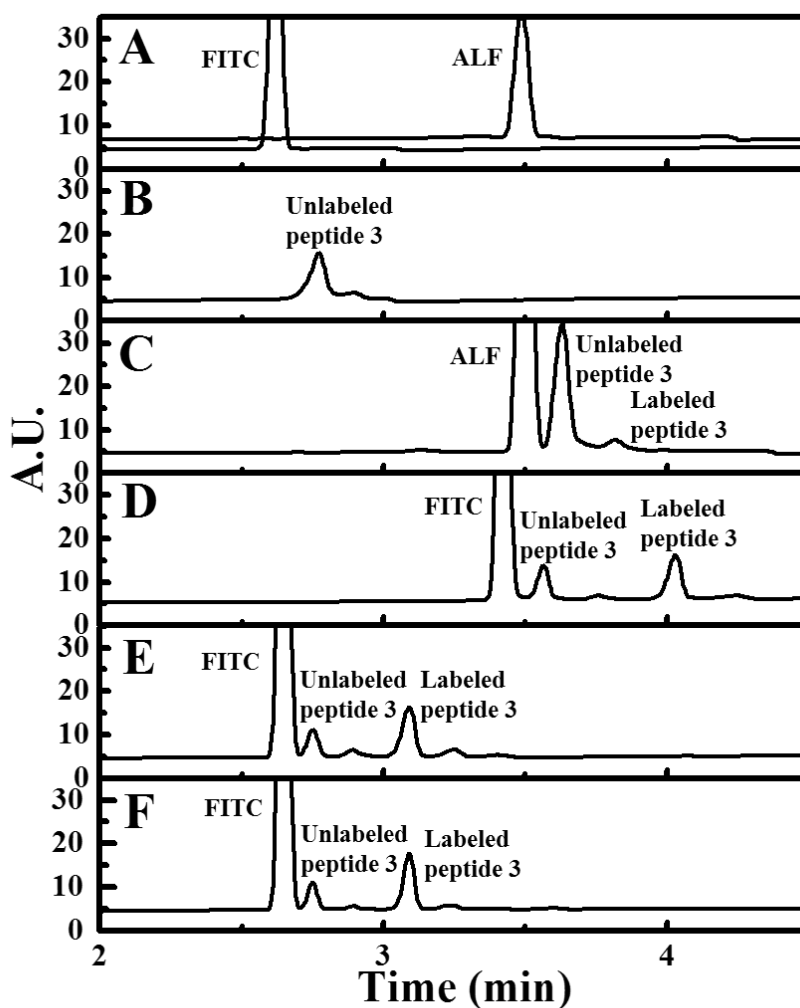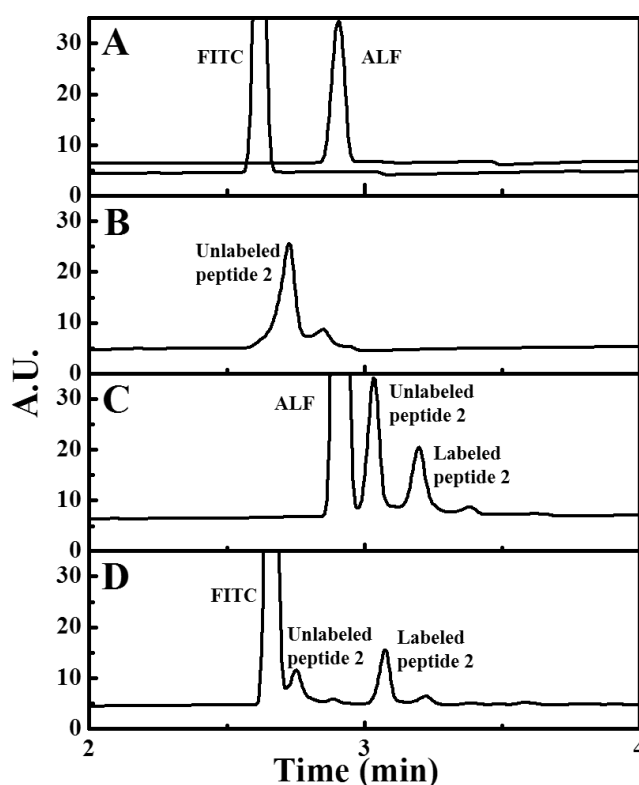

Figure 4.6 CE separation of peptide 2 labeled with ALF and FITC under different conditions. (A) FITC (500 µM) and ALF 488 (4.5 µM). Separation in 50 mM borate buffer, pH 10.5, 25.0 kV. (B) Unlabeled peptide 2 (70 µM). (C) Peptide 2-native (50 µM). Separation in 50 mM borate buffer, pH 10.5, 25.0 kV. (D) Peptide 2-denatured (23 µM). Labeling conditions are in Table 4.2.

Finally, peptide 1 was labeled with FITC and separated using CE as shown in Figure 4.7. Figures 4.7A-B show CE separations of FITC and unlabeled peptide 1, respectively; both the peaks

were symmetrical. In Figure 4.7C, the degree of peptide 1 labeling was low under native conditions; moreover, the unlabeled and labeled peptide 1 peaks showed tailing and fronting, respectively. As with peptides 2-3, peptide 1 labeling was improved significantly (see Figure 4.7D) on denaturing before labeling, and a symmetrical peak was formed in the CE run.
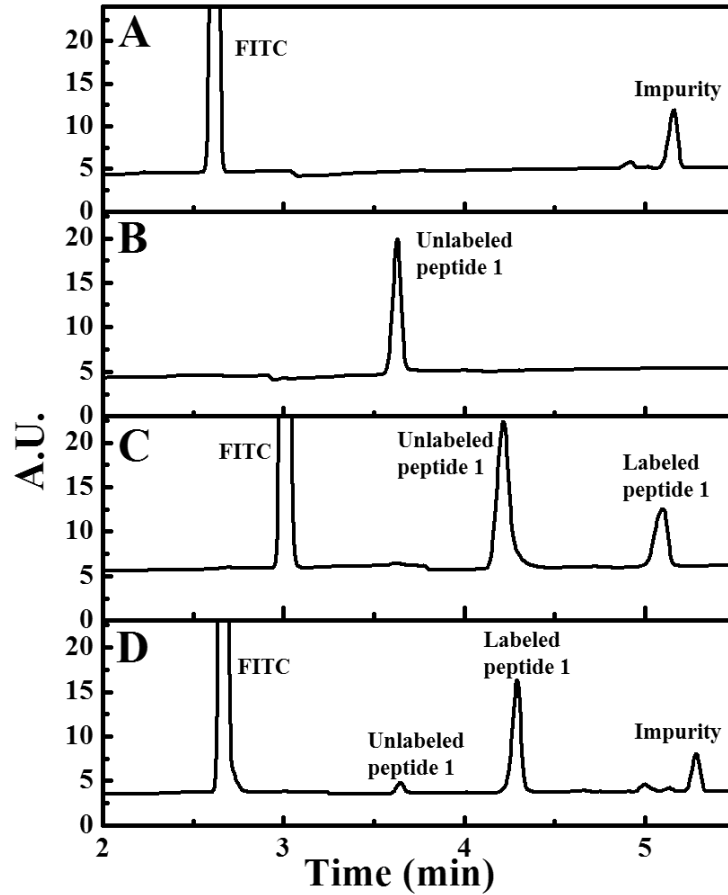
Figure 4.7 CE separation of peptide 1 labeled with FITC under different conditions. (A) FITC (500 µM). (B) Unlabeled peptide 1 (50 µM). (C) Peptide 1-native (100 µM). Separation in 50 mM borate buffer, pH 10.5, 25.0 kV. (D) Peptide 1-denatured (60 µM). Labeling conditions are in Table 4.2.

Differences in migration times of peptides and dyes resulted from different CE conditions described in the figure captions. Furthermore, ALF- and FITC-labeled peptide migration was

different under similar CE conditions because of their different charge-to-mass ratios. For all three peptides, the labeling was improved when they were denatured before labeling. Among the peptides, peptide 1 showed the best labeling, most likely because it is shorter than peptides 2 and 3, so the N-terminus is more accessible.

On-chip protein labeling for PTB analysis in an integrated device may need to be done with low protein concentrations (~1 μM) in low ionic strength (10 mM) buffers with short (~20 min) reaction times. I tested conventional off-chip labeling conditions, including ones that might be used for on-chip labeling. Both ALF and FITC were tested; protein-dye mixtures were incubated for 20 min and overnight at room temperature. Labeled Fer samples were separated by μCE as shown in Figure 4.8. Fer was labeled to approximately the same degree in 20 min with ALF and FITC in Figure 4.8A. In contrast, Fer was labeled better with ALF over FITC in overnight labeling in Figure 4.8B; however, the Fer peaks were broader compared to 20 min labeling. Fer is a large (450 kDa) protein and has thirteen lysine residues that can react with FITC and ALF. Available labeling sites would be distributed on Fer and longer labeling times would result in reaction of more of the available sites. However, not all Fer molecules label equally, so they form isomers with different charge-to-size ratios primarily due to charge change. These isomers should have closely related electrophoretic mobilities and would migrate as a broad, unresolved band in μCE. Therefore, limited site labeling of Fer with short reaction times offers the opportunity for a narrower peak which can result in better resolution in separation with other PTB biomarkers.
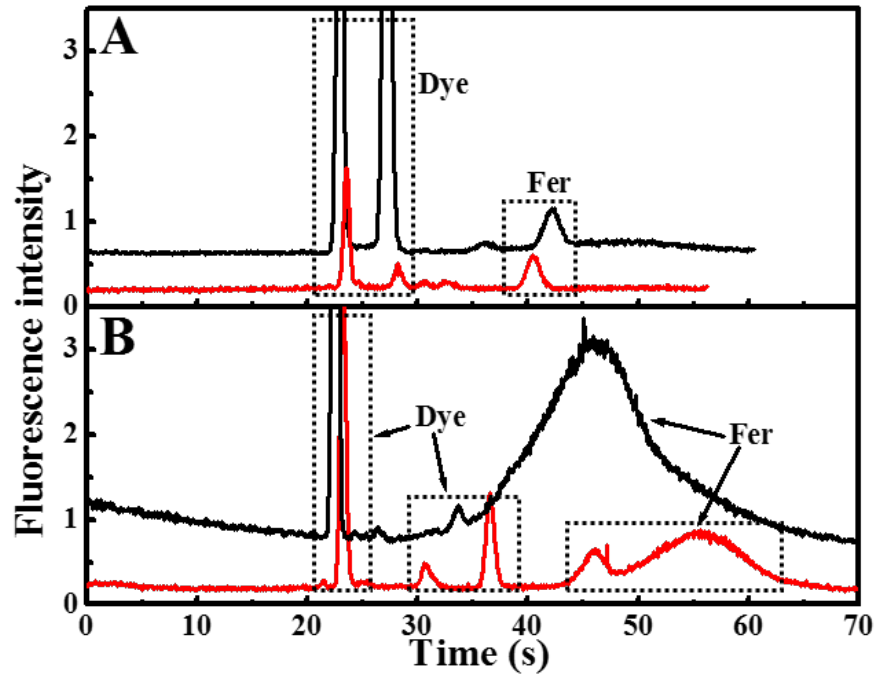
Figure 4.8 Microchip electropherograms of 500 nM Fer labeled with ALF 488 (black) and FITC (red). (A) 20 min incubation, and (B) overnight incubation.

Finally, FITC-labeled PTB biomarker mixtures were separated by µCE as shown in Figure 4.9. All mixtures were separated in less than 2 min, and provided adequate resolution to include other PTB biomarkers with different mobilities in the future. The impurity peak in the electropherograms likely resulted from breakdown of peptides into smaller fragments during labeling or other conditions. Fragments smaller than 2 kDa were removed during the dye filtration process, while larger fragments would appear as impurities. Peptides 2 and 3 were not used in the same mixture since their mobilities are similar, as both peptides have the same amino acid sequence and only differ in the oxidation of a methionine in peptide 3. Peptides 2 and 3 might be resolved by labeling each one with a different dye (i.e., FITC and ALF) that would result in a greater difference in charge-to-size ratio. Alternatively, different buffer pH might also change

charge-to-size ratios; or the oxidized methionine could be alkylated selectively to change peptide

3's charge-to-size ratio.[16]
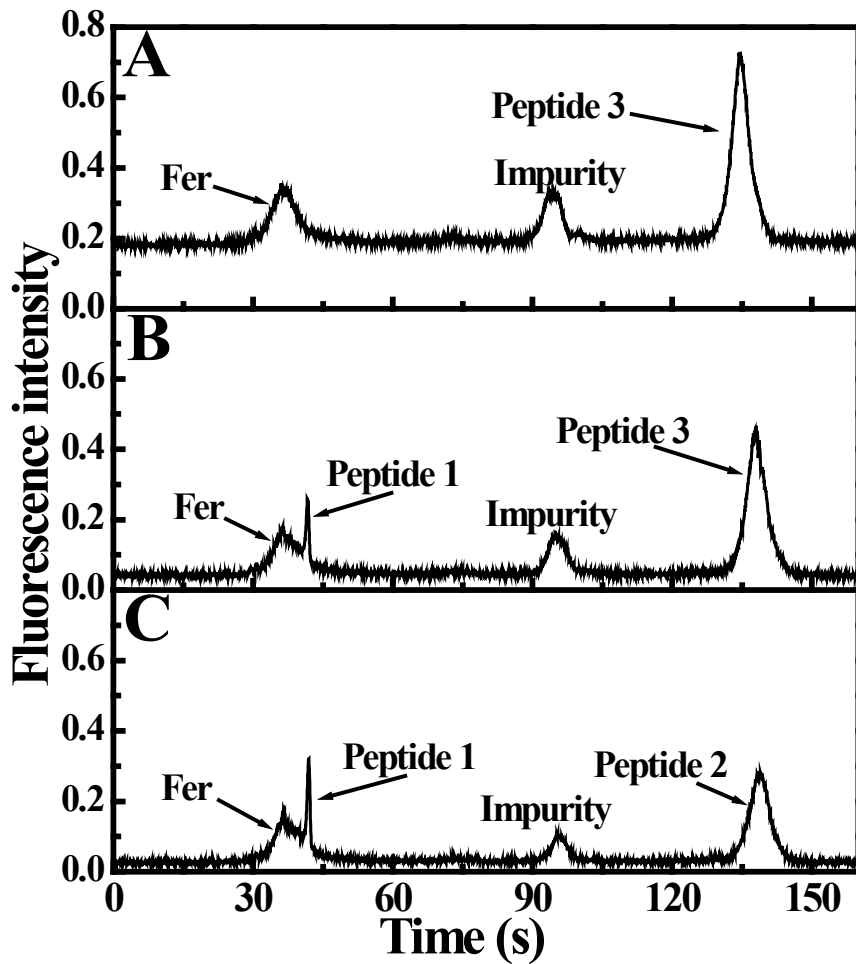
Figure 4.9 Microchip electrophoresis of PTB biomarkers. (A) Fer and peptide 3. (B) Fer, peptide 1 and peptide 3. (D) Fer, peptide 1 and peptide 2.

4.5 REFERENCES

1.   Holler, F. J.; Skoog, D. A.; West, D. M., Fundamentals of analytical chemistry. 7th ed.; Saunders College Publication: Philadelphia, **1996**.

2.   Ludwig, J. A.; Weinstein, J. N., Biomarkers in cancer staging, prognosis and treatment selection. Nat. Rev. Cancer **2005,** 5, 845-856.

3.   Frank, R.; Hargreaves, R., Clinical biomarkers in drug discovery and development. Nat. Rev. Drug Discovery **2003,** 2, 566-580.

4.   Henry, N. L.; Hayes, D. F., Cancer biomarkers. Mol. Oncol. **2012,** 6, 140-146.

5.   Urbschat, A.; Obermüller, N.; Haferkamp, A., Biomarkers of kidney injury. Biomarkers **2011,** 16, S22-S30.

6.   Goldenberg, R. L.; Culhane, J. F.; Iams, J. D.; Romero, R., Epidemiology and causes of preterm birth. Lancet **2008,** 371, 75-84.

7.   Esplin, M. S.; Merrell, K.; Goldenberg, R.; Lai, Y.; Iams, J. D.; Mercer, B.; Spong, C. Y.; Miodovnik, M.; Simhan, H. N.; van Dorsten, P., Proteomic identification of serum peptides predicting subsequent spontaneous preterm birth. Am. J. Obstet. Gynecol. **2011,** 204, 391. e1-391. e8.

8.   Diamandis, E. P., Mass spectrometry as a diagnostic and a cancer biomarker discovery tool opportunities and potential limitations. Mol. Cell. Proteomics **2004,** 3, 367-378.

9.   Whitesides, G. M., The origins and the future of microfluidics. Nature **2006,** 442, 368-373.

10.   Zhu, Y.; Fang, Q., Analytical detection techniques for droplet microfluidics—A review. Anal. Chim. Acta **2013,** 787, 24-35.

11.   Lacroix, M.; Poinsot, V.; Fournier, C.; Couderc, F., Laser-induced fluorescence detection schemes for the analysis of proteins and peptides using capillary electrophoresis. Electrophoresis **2005,** 26, 2608-2621.

12.   Patonay, G.; Salon, J.; Sowell, J.; Strekowski, L., Noncovalent labeling of biomolecules with red and near-infrared dyes. Molecules **2004,** 9, 40-49.

13.   Dobson, C. M., Protein folding and misfolding. Nature **2003,** 426, 884-890.

14.   Kelly, R. T.; Woolley, A. T., Thermal bonding of polymeric capillary electrophoresis microdevices in water. Anal. Chem. **2003,** 75, 1941-1945.

15.   Jacobson, S. C.; Hergenroder, R.; Koutny, L. B.; Warmack, R.; Ramsey, J. M., Effects of injection schemes and column geometry on the performance of microchip electrophoresis devices. Anal. Chem. **1994,** 66, 1107-1113.

16.   Saunders, C. C.; Stites, W. E., An electrophoretic mobility shift assay for methionine sulfoxide in proteins. Anal. Biochem. **2012,** 421, 767-769.

5. DESIGN AND FABRICATION OF AN INTEGRATED PUMP AND VALVE SOLID-PHASE EXTRACTION AND MICROCHIP ELECTROPHORESIS SYSTEM

5.1 INTRODUCTION

Microfluidics allows integration of many laboratory processes on a single platform to provide complete analysis.[1-2] These micro total analysis systems (µTAS) include processes like sample preparation, analyte separation, and detection.[3] Sample preparation including microdialysis, extraction, purification, preconcentration, and on-chip derivatization such as fluorescent labeling, consumes considerable time in analyses;[4] therefore, its integration is significant. Integration of sample preparation with other processes offers advantages of high throughput, automation, and faster analysis compared to traditional methods.[5]

Solid-phase extraction (SPE) is a common sample preparation method[6] explored for integration in microfluidic systems,[7] especially reversed-phase and affinity SPE.[8-9] Reverse-phase SPE utilizes hydrophobic interactions between the sample and solid support.[10] A solid support can be built in microfluidic channels by either particle packing or monolith fabrication.[11] Monoliths are gaining popularity because of the ease of on-chip fabrication and ability to tune structure by adjusting the synthesis conditions.[12] Monoliths can be made with alkyl chains such as butyl (C4), octyl (C8), lauryl (C12) or octadecyl (C18) for reversed-phase applications.[13] This chapter focuses on the design and fabrication of a pressure-driven, reversed-phase SPE and microchip electrophoresis (µCE) integrated system. The application of this system will be covered in Chapter 6. Herein, C8 monoliths are made to capture and enrich samples and perform on-chip covalent labeling with a fluorescent dye. As reversed-phase SPE involves use of organic solvents to elute sample from the solid support, an organic solvent compatible material, cyclic olefin copolymer (COC), is used for microchip fabrication. Furthermore, a peristaltic pump and pneumatic valves

are integrated in the system to allow controlled manipulation of fluids. The integrated SPE and separation system described in this chapter comprises parts B-C of the microfluidic system in Figure 5.1, which will be used for the complete analysis of pre-term birth (PTB) biomarkers.
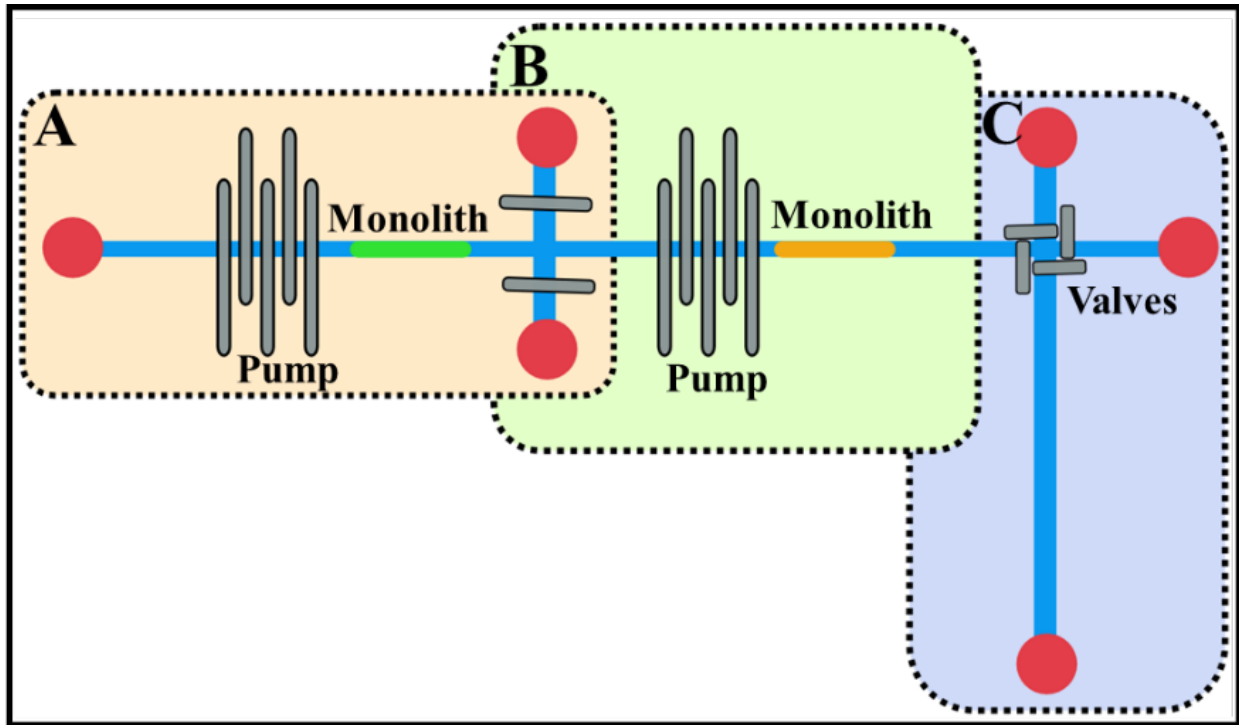
Figure 5.1 Schematic of a pump and valve integrated microfluidic system for complete analysis of PTB biomarkers. (A) Immunoaffinity extraction module. (B) SPE and on-chip labeling module. (C) Electrophoretic separation module.

5.2 MATERIALS

The integrated device is a four layer structure consisting of two polydimethylsiloxane (PDMS) and two COC layers. A single-side-polished 100 mm Si wafer (Desert Silicon, Tempe, AZ) with <100> orientation is used to make fluidic and control layer templates. PDMS base and curing agent kit used for fluidic and control layer fabrication is obtained from Dow Chemical (Midland, MI). Tridecafluorooctyltrichlorosilane (UCT, Bristol, PA) is used to prime control and

fluidic templates to prevent sticking of cured PDMS to Si. Microfluidic channels are enclosed in top and base COC (Zeonor 1020R, Zeon Chemicals, Louisville, KY). Octylmethacrylate (OMA) and Tween 20 are obtained from Scientific Polymer (Ontario, NY) and Mallinckrodt (Paris, KY), respectively. Ethylene glycol dimethacrylate (EGDMA, 98%), 2,2-dimethoxy-2-phenylacetophenone (DMPA, 99%), 1-dodecanol (98%), cyclohexanol, and 2-propanol (IPA) are obtained from Sigma-Aldrich (St. Louis, MO). A SunRay 600 UV lamp (Uvitron International, West Springfield, MA) is used to polymerize monoliths. A biopsy punch (Miltex, York, PA) is used to make 2.5 mm diameter reservoirs in PDMS layers. Blunt-end, 1.5"-long, 22-gauge needles are obtained from Jansen Global (Santa Barbara, CA) to punch holes in the control PDMS layer. Circuit board drill bits (550 and 200 μm diameter) are purchased from MSC Industrial Supply (Melville, NY) to make holes in top COC plates.

5.3 METHODS

5.3.1 Solid-phase extraction module

The SPE module is a multi-layer structure, made up of elastomeric and thermoplastic materials (see Figure 5.2). An elastomeric material, PDMS, is used for making pneumatic valves and the peristaltic pump, as shown in Figure 5.2A-B. Reservoirs 1, 2, and 3 are used to introduce buffer, sample, and eluent, respectively, and waste is collected in reservoir 4. A pneumatic valve on each inlet helps in regulating the flow of fluid from the reservoir and enable automation. The peristaltic pump, placed after the junction, pushes fluid through the fluidic channel into the COC reservoir. Each pneumatic valve is 150 μm wide and spaced at a 150 μm pitch to make a three-valve peristaltic pump. This configuration of peristaltic pump generates an approximate flow rate of 12 nL/min for 85% v/v acetonitrile at a 40 Hz actuation frequency. The COC channel contains

a C8 monolith for reversed-phase SPE. Reservoirs connect the COC channel to the fluidic channel in the PDMS layer and enable integration.
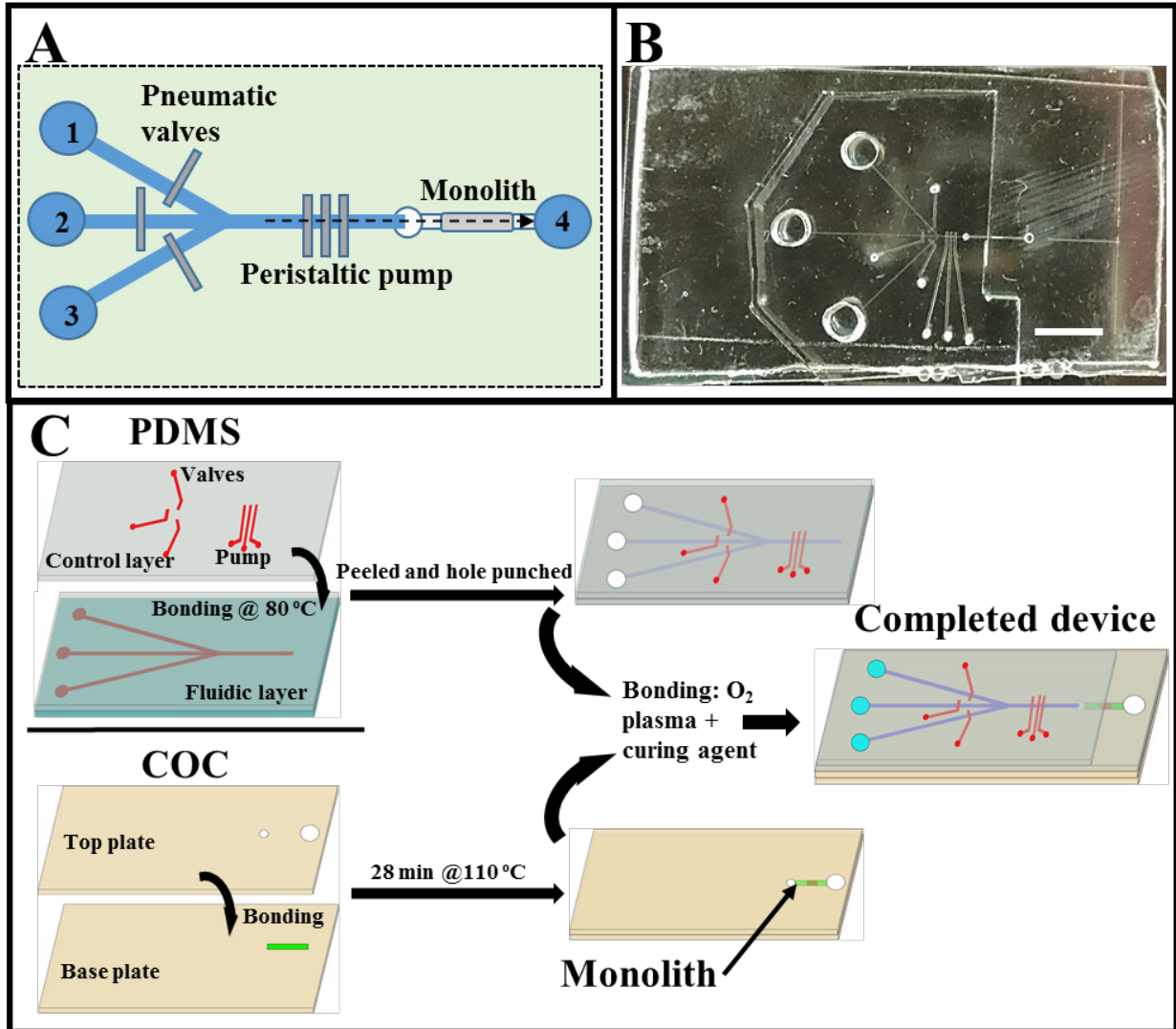

Figure 5.2 Design and fabrication of the SPE module. (A) Device schematic, 1: buffer, 2: sample, 3: eluent, and 4: waste reservoir. (B) Photograph of a completed device; scale bar is 5 mm. (C) Schematic showing assembly process.

Each layer of the SPE module is fabricated separately. Fluidic and control Si templates are fabricated using photolithography and wet etching as shown in Figure 5.3. Four-inch Si wafers cleaned in buffered oxide etchant (BOE, Transene, Danvers, MA) for 30 s and baked at 150 °C for 15 min are used to make templates. Cleaned Si wafers are exposed to hexamethyldisilazane (HMDS) vapor at 65 °C for 5 min to coat the surface. Then, photoresist (AZ 50XT, AZ Electronic Materials, Branchburg, NJ) is spin coated on the fluidic and control wafers to make 13.5 and 20 μm thick photoresist layers, respectively. Photoresist-coated wafers are soft baked at 60 °C for 10 min to degas the photoresist layer and subsequently at 125 °C for 3 min. Baked control and fluidic wafers are cooled in air for 2 min and placed in a box to rehydrate the photoresist for 40 min. Photoresist rehydration is a crucial step that prevents cracking. Then, the fluidic and control wafers are exposed to UV light through a clear-field Cr mask in a UV aligner (Karl Suss America, Waterbury, VT) to transfer mask features into the photoresist layer. Exposed wafers are developed in diluted MIF 400K developer (AZ electronics, Somerville, NJ) for 3-4 min to form fluidic and control channel features. The developed fluidic wafer is heated at 125 °C for 10 min to reflow photoresist and form rounded features. A post development bake increases the fluidic channel height to ~18 μm. Finally, the fluidic and control layer feature heights are confirmed using an Alpha Step 200 profilometer (Tencor, Mountain View, CA).
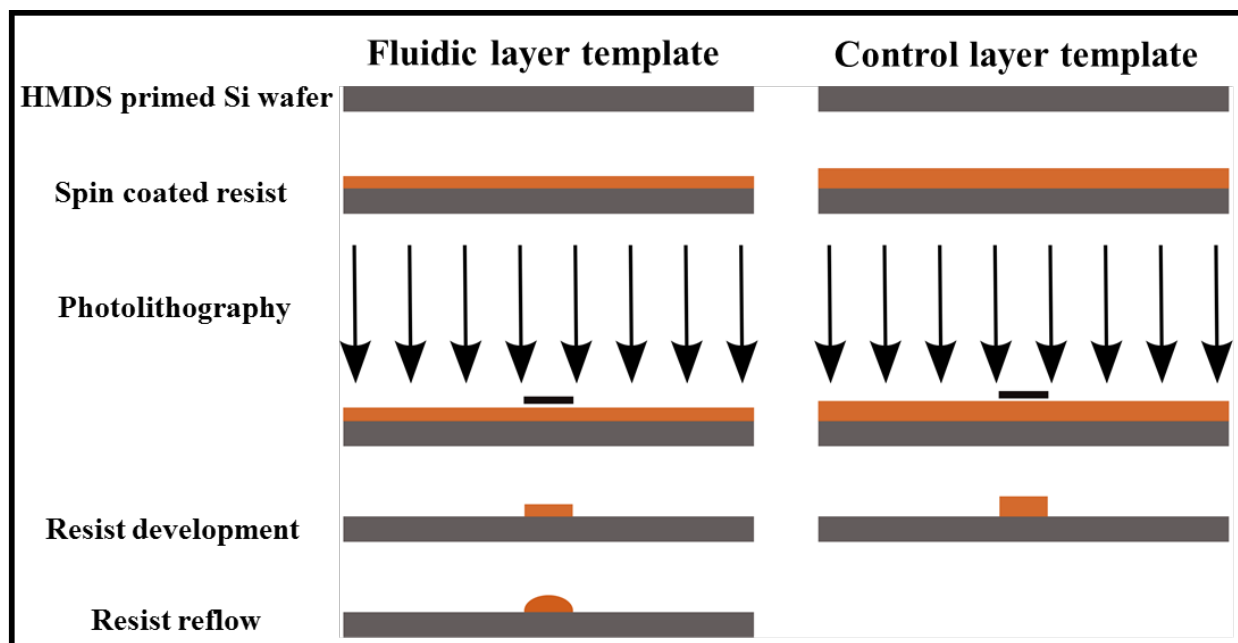
Figure 5.3 Schematic showing fabrication of fluidic and control layer templates.

Next, fluidic and control template features are transferred into PDMS by soft lithography as shown in Figure 5.4. PDMS base and curing agent are mixed in 4:1 and 20:1 for the fluidic and control layers, respectively, and degassed for 30 min in vacuum. In the meantime, fluidic and control templates are silanized by exposing to tridecafluoro-trichlorosilane vapor at 80 °C for 10 min. A 4" diameter PVC ring has its edges coated with degassed control layer PDMS mixture, and the silanized control template is placed on it to make an airtight seal. The PVC ring prevents PDMS leakage and maintains constant material height during polymerization. The assembly is baked on a hot plate at 80 °C for 10 min to polymerize PDMS. Next, control layer PDMS mixture is poured in the center of the control template and allowed to spread uniformly to cover the features. The silanized fluidic template is spin coated with fluidic layer PDMS mixture to form a uniform coating of 25-28 μm thickness. Finally, the fluidic and control layer PDMS is cured in an oven at 80 °C for 1 hour. Cured control layer PDMS is peeled off from the template and diced into individual devices, and then holes are punched using a 22-gauge blunt end needle to connect control channels

to pressure tubing. Hole-punched control PDMS is cleaned using IPA, stamped with curing agent coated on a Si wafer, aligned and contacted to the fluidic PDMS layer while observing in a modified stereomicroscope. Aligned PDMS layers are baked at 80 °C for 1 hour to form a bond. Then, the bonded PDMS layers are peeled off from the fluidic templates, and reservoir holes are made using a biopsy punch.
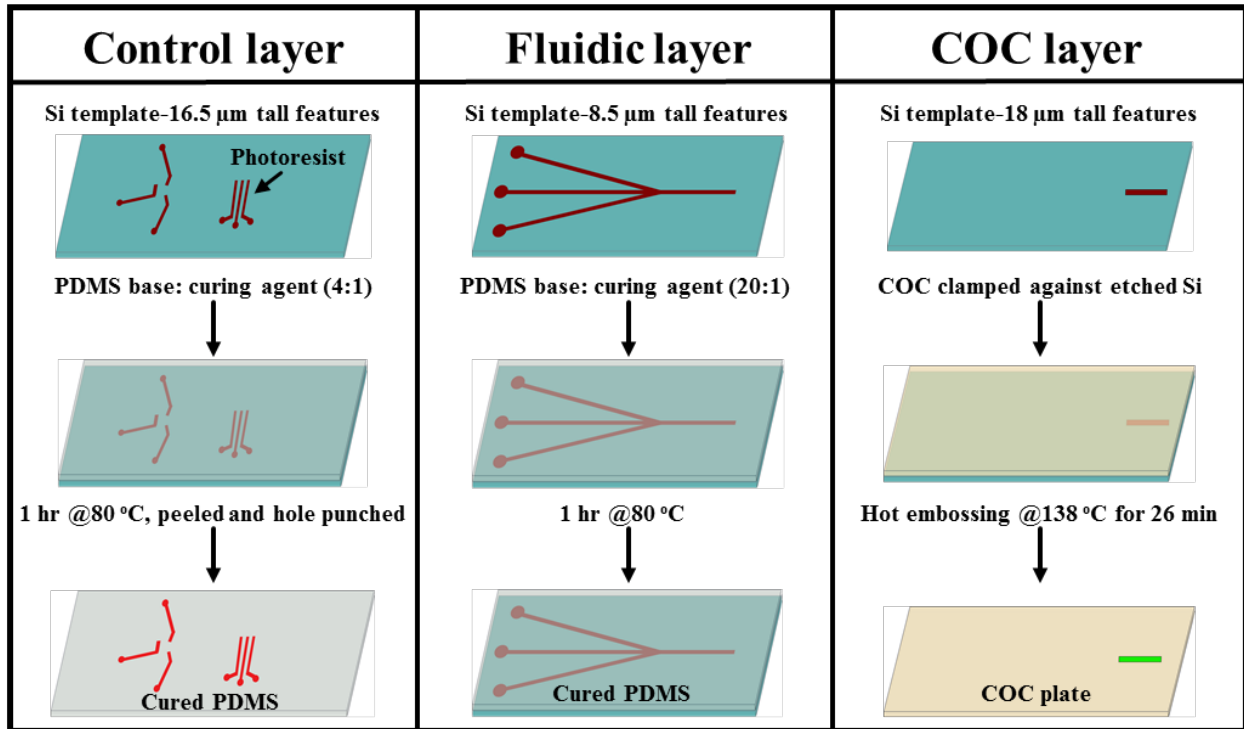
Figure 5.4 Schematic showing fabrication of control, fluidic and COC layers for the SPE unit.

In parallel, the COC channels are made as shown in Figure 5.4. A 4" Si template is prepared to make COC channels as described in Chapter 4.3.1 and Figure 4.1; the template is wet etched in 40% aqueous KOH solution at 70 °C to yield 18-20 μm tall features. A 1 mm thick 6" x 6" COC plate is cut into 3.5 x 2.5 cm^2 pieces using a bandsaw, and edges are smoothed with a razor. Etched Si template features are then hot embossed in COC at 138 °C for 26 min. Holes are drilled in a 1-mm-thick COC plate using a 0.54 mm diameter drill bit, and the plate is reflattened at 110 °C for

20 min. COC with imprinted features is aligned and thermally bonded to the drilled COC plate at 110 ºC for 23 min, and the bonded COC device edges are sealed using cyclohexane. A C8 monolith is formed inside the COC channel as described in the next section of this chapter. Finally, PDMS and COC structures are bonded together as shown in Figure 5.2C. Briefly, COC and PDMS are cleaned with IPA and dried using a N_2 gun. The COC device surface is further cleaned in an O_2 plasma (Planar Etch II, Technics, Osaka, Japan) for 4 min at 200 W, and the PDMS is stamped in curing agent coated on a wafer. Finally, COC and PDMS are aligned and thermally bonded at 80 ºC for 1.5 h. Figure 5.2B shows a photograph of a complete device.

5.3.2 Octylmethacrylate monolith

SPE is performed on a solid porous support formed inside a COC channel by in-situ UV photopolymerization of monomer, porogens and crosslinker mixture in the composition shown in Table 5.1. A schematic showing monolith fabrication in a COC channel is shown in Figure 5.5A. Monolith solution with the composition in Table 5.1 and having a total mass of 1.18 g is prepared by weighing in a 10 mL glass vial. The mixture is vortexed for 30 s and sonicated for 5 min. Next, 12 mg of DMPA is weighed and added to the monolith mixture, followed by vortexing and sonication for 10 min. After that, the mixture is purged with N_2 for 5 min to remove dissolved gas. The COC channel is rinsed with IPA and vacuum dried followed by the introduction of degassed monolith mixture using a 2 µL pipette. The solution flows through the COC channel due to capillary action, and excess solution is removed from the inlet reservoir. A Cr mask with multiple openings is used to cover the solution-filled COC channel, exposing the desired channel area where the solution is polymerized. The assembly is stabilized using electrical tape, another COC device of similar thickness is attached to the mask to maintain uniform height, and everything is placed in a SunRay 600 UV floodlight chamber at a 14" distance from the bulb. The UV lamp is turned

on at 50 mW/cm^2, and the device is exposed for 11 min. Then, the device is removed from the Cr mask, reservoirs are rinsed with IPA and unpolymerized monolith solution is removed by vacuum. The monolith is further rinsed with IPA to remove any unpolymerized components left on the surface, followed by water rinsing to remove IPA. A photograph of a polymerized monolith in a COC device is shown in Figure 5.5B (left).

Table 5.1 Composition of C8 monolith. All percentages are by mass.

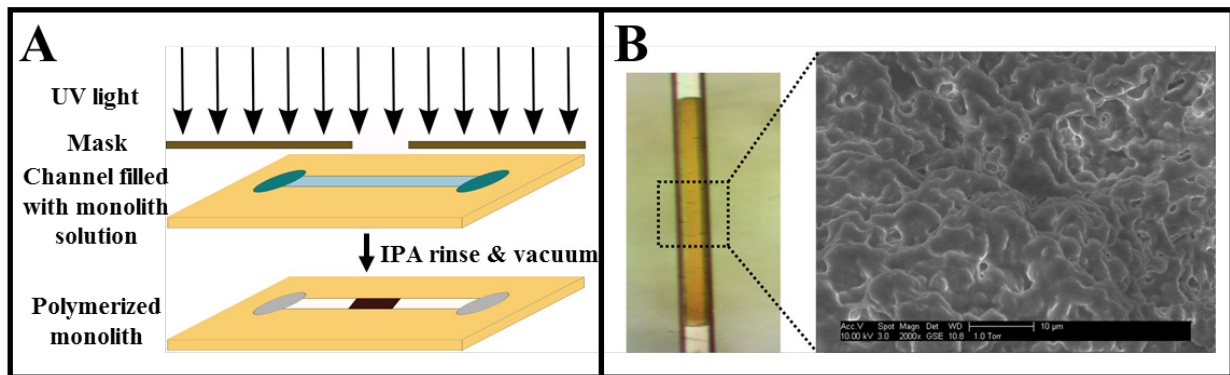|	
Monomer	Octylmethacrylate (23%)
Cross linker	Ethylene glycol dimethacrylate (11%)
Photoinitiator	2,2-Dimethoxy-2-phenylacetophenone (1%)
Porogens	Cyclohexanol (25%), 1-dodecanol (23%), and Tween 20 (17%)

Figure 5.5 C8 monolith fabrication. (A) Schematic showing fabrication steps. (B) Photograph and SEM image showing internal structure.

The morphology of a bulk-polymerized C8 monolith is observed using a Philips XL30 FEG environmental scanning electron microscope (ESEM) from FEI (Hillsboro, OR, USA). Sample preparation includes polymerization of 200 µL of monolith solution in a polypropylene tube under similar UV exposure. The polymerized monolith mass is broken into small pieces and mixed in IPA on a shaker overnight to remove unpolymerized solution. Finally, the monolith is stored in vacuum overnight to form a dry, porous structure. The dried monolith is placed on a carbon taped stub and examined under ESEM for internal structural information as shown in Figure 5.5B (right). ESEM imaging shows that fused structures are formed with varying pore sizes, which allow liquid flow through the monolith structure.

5.3.3 Microchip electrophoresis

A three-layer µCE device is fabricated similar to the SPE module, except for the COC channel and monolith fabrication. The layout and an actual device are shown in Figure 5.6. A three-valve peristaltic pump and a set of four pneumatic valves are incorporated around a 'T' shape design channel network to manipulate fluids using pressure. Valves are 250 µm wide, and are spaced with a 120 µm gap in the peristaltic pump. Reservoir 1 is used to introduce fluorescenctly labeled analyte solution using the on-chip peristaltic pump. A set of four pneumatic valves surrounding the injection intersection is used for capturing the sample plug. Reservoirs 3 and 4 are filled with separation buffer and sample waste is collected in reservoir 2. During electrophoresis, reservoir 3 is kept at ground while high voltage is applied at reservoir 4. Sample plug formation depends on factors such as valve spacing at the intersection, solution flow rate, and intersection geometry. A fixed valve spacing of 300 µm from the intersection to each valve is used. A different study is ongoing to optimize the valve spacing for the final device.[14] Solution flow rate can be controled using pump actuation frequency, and a simple "T" intersection is used in all devices.
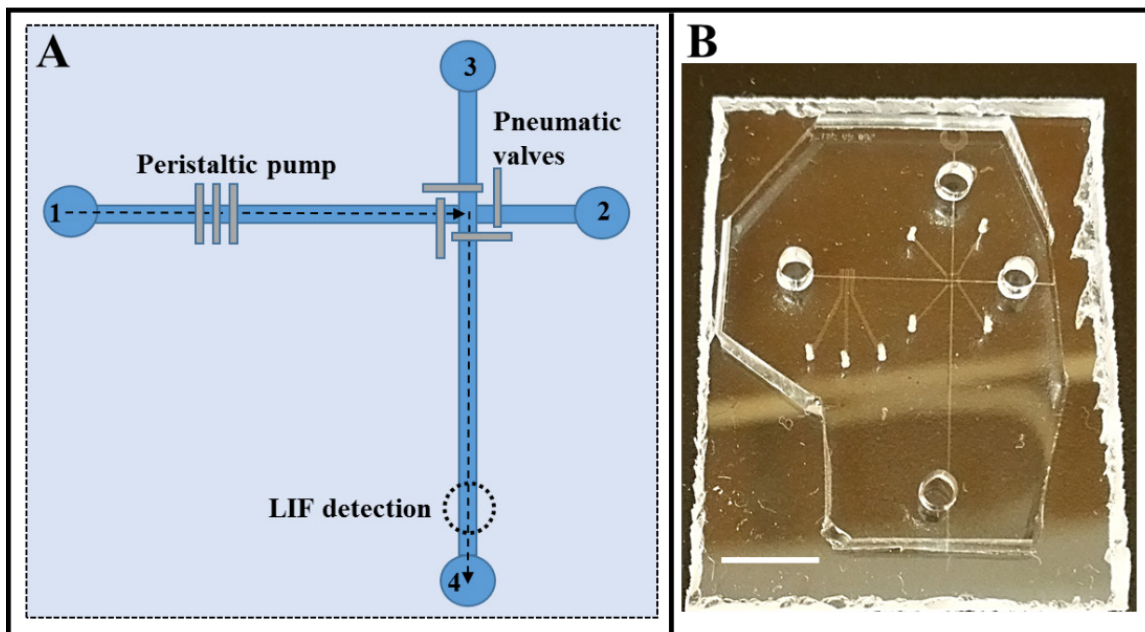
Figure 5.6 Design of separation module. (A) Device schematic, 1: sample, 2: waste, 3: ground, and 4: high voltage reservoir. (B) Photograph of completed device; scale bar is 7 mm.

The fabrication procedure for the separation module is similar to that for the SPE system, as shown in Figure 5.7. Fluidic and control templates are fabricated as described in Section 5.3.1. PDMS base and curing agent mixture are prepared in a ratio of 4.4:1 and 19:1 for the control and fluidic layer, respectively. All other processes are the same as in Section 5.3.1.
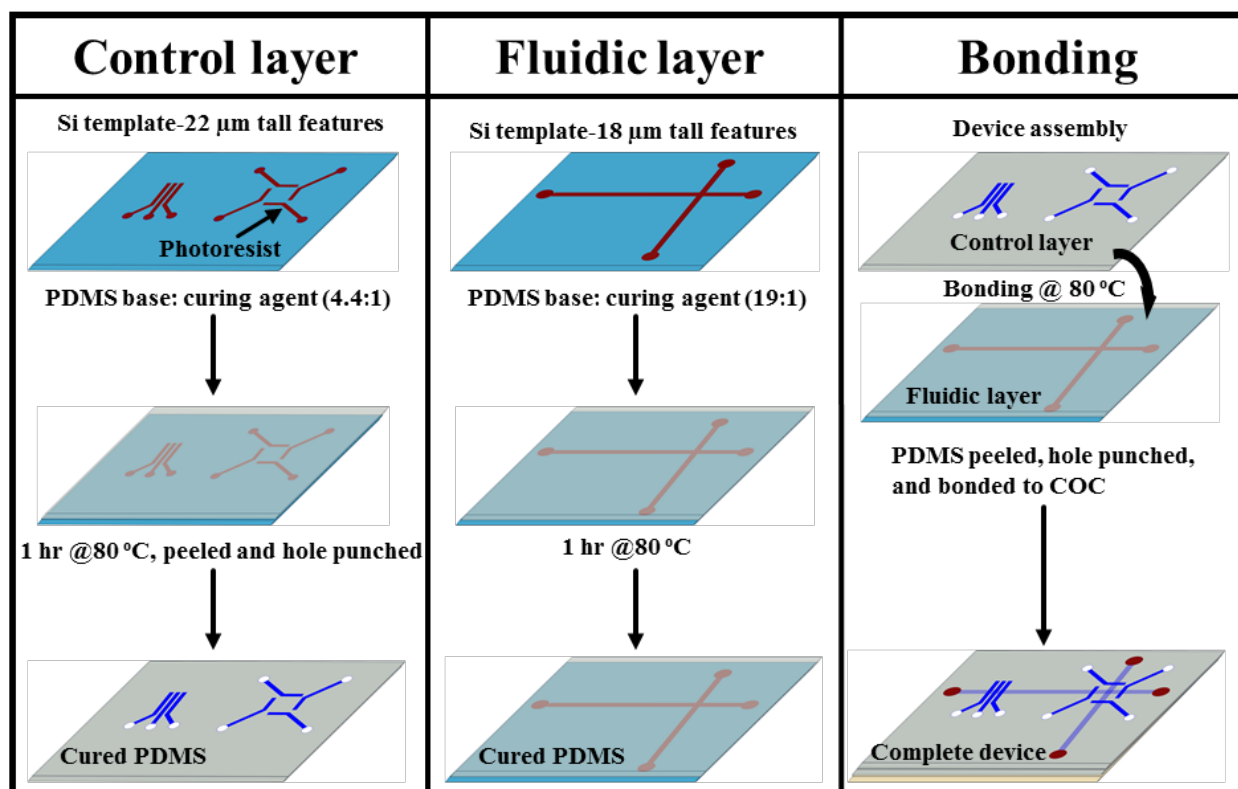
Figure 5.7 Fabrication of control and fluidic layers for the separation module and their assembly to make a device.

5.3.4 Integration of the SPE and separation modules

The SPE and separation modules were integrated on a single platform to provide complete on-chip analysis of PTB biomarkers as shown in Figure 5.8. The SPE design was slightly modified to simplify the fabrication procedure and increase device yield. Previously, the purpose of using three inlet channels to the SPE module (Figure 5.2A-B) was to automate device operation. However, the SPE process requires 8-10 different solutions which makes necessary many sample inlets for complete automation, making the device design more complex. Therefore, in these initial studies the SPE design was simplified to have a single inlet to allow preliminary study of integration with the separation module. The peristaltic pump was also switched to a five-valve configuration from three valves because the five-valve pump was found to generate a higher flow rate (data are in

section 6.4). In the integrated design, prelabeled or unlabeled analyte was captured and concentrated on the C8 monolith. Unlabeled analyte was derivatized fluorescently for detection. Sample prepared in the SPE unit was released and captured at the injection intersection using valves, and the captured plug was separated into individual analytes by microchip electrophoresis. Reservoir 1 was used to introduce sample, dye, buffer, and ACN-buffer mixtures. Reservoirs 2 and 4 collected sample and separation waste, respectively. Reservoirs 3 and 4 were filled with separation buffer and used to apply voltage along the separation channel during μCE.
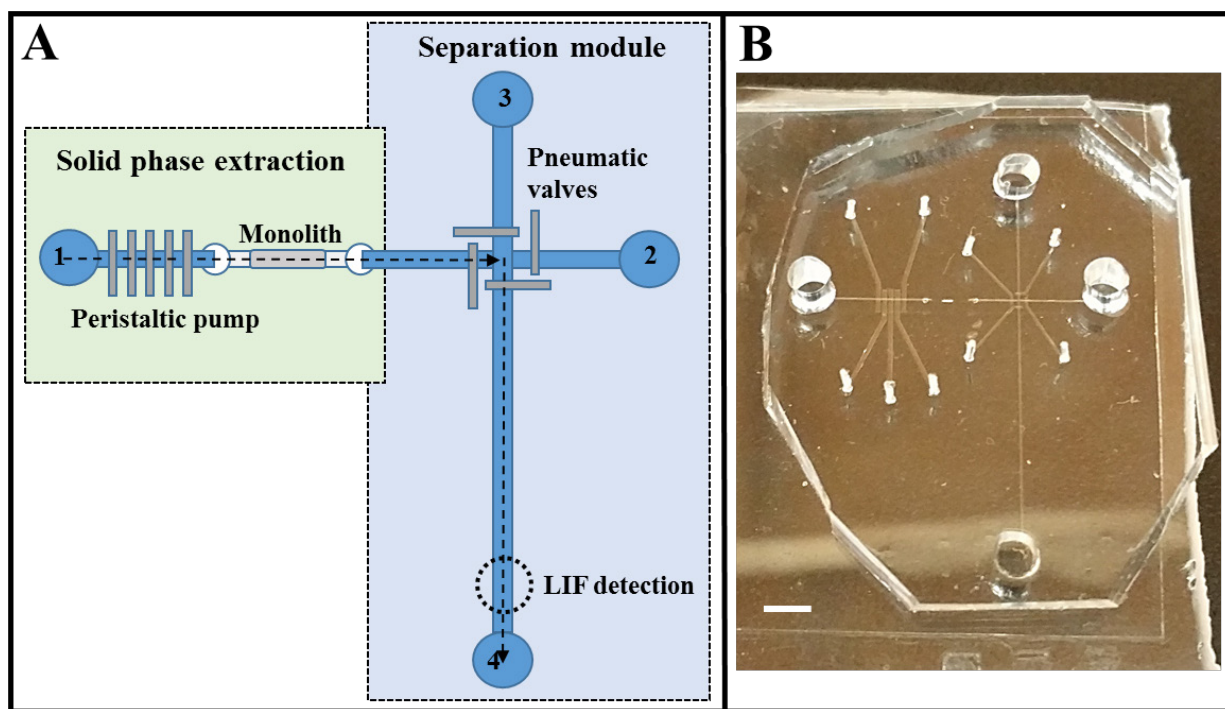
Figure 5.8 Design of integrated SPE and separation module. (A) Device schematic, 1: buffer, sample, or eluent reservoir, 2: waste, 3: ground, and 4: high voltage reservoir. (B) Photograph of completed device; scale bar is 3 mm.

The fabrication procedure is similar to that for the separation module described in Section 5.3.3. Briefly, control and fluidic PDMS layers are prepared by polymerizing the PDMS base and curing agent mixture on the templates as shown in Figure 5.9. The control layer is bonded to the

fluidic layer and holes are punched. COC device fabrication is modified to reduce dead volumes in the final device. One-millimeter-thick COC is cut into 1x1 cm^2 pieces using a bandsaw. Each 1-mm-thick COC piece is thinned to 80-100 μm using a hydraulic press (Carver, Wabash, IN) with top and base plates heated to 196 °C and ~2 metric tons applied pressure. Thinned COC is again cut into sizes matching the base COC plate, and holes are drilled using a 200-μm-diameter circuit board drill bit. The top COC plate is flattened between two glass slides at 110 °C for 25 min and thermally bonded to the imprinted base COC at 110 °C for 28 min. This new COC device design allows COC reservoir filling in less than 1 min when the pump is actuated. Then, a C8 monolith is polymerized in the COC channel as described in Section 5.3.2. Finally, all layers are assembled and bonded together as shown in Figure 5.10 and described in Section 5.3.1 to make the final device. A photograph of a completed integrated device is shown in Figure 5.8B.
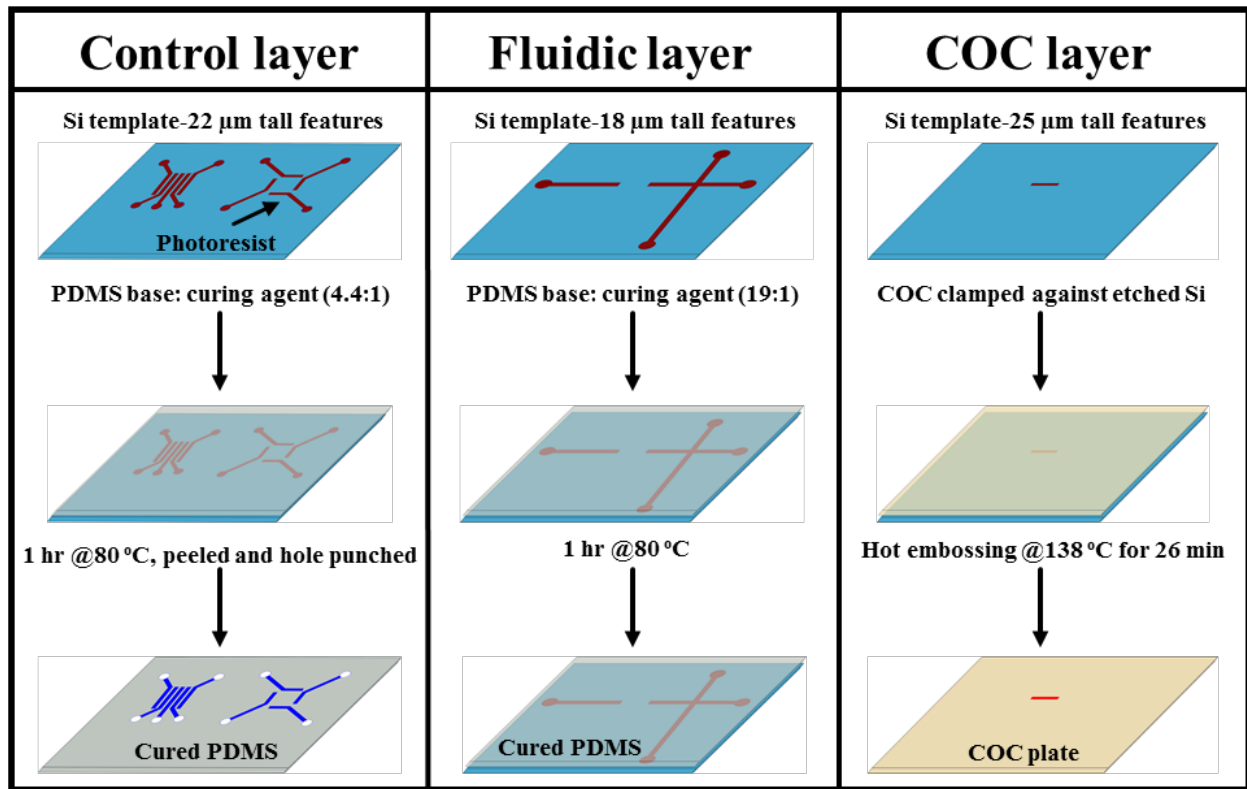
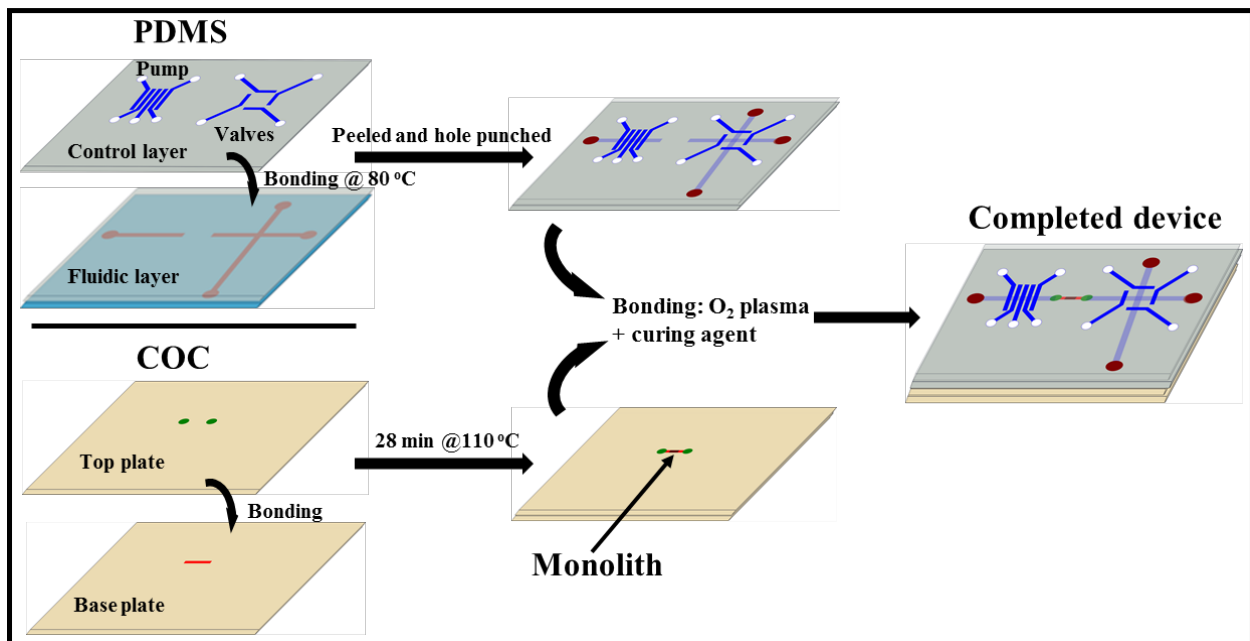**Figure 5.9** Fabrication of control, fluidic and COC layers for an integrated device.

Figure 5.10 Schematic showing assembly of an integrated device.

5.4 REFERENCES

1.   Erickson, D.; Li, D., Integrated microfluidic devices. *Anal. Chim. Acta* **2004,** *507*, 11-26.

2.   Yu, Z. T. F.; Guan, H.; Cheung, M. K.; McHugh, W. M.; Cornell, T. T.; Shanley, T. P.; Kurabayashi, K.; Fu, J., Rapid, automated, parallel quantitative immunoassays using highly integrated microfluidics and AlphaLISA. *Sci. Rep.* **2015,** *5*, 1-12.

3.   Culbertson, C. T.; Mickleburgh, T. G.; Stewart-James, S. A.; Sellens, K. A.; Pressnall, M., Micro Total Analysis Systems: Fundamental Advances and Biological Applications. *Anal. Chem.* **2014,** *86*, 95-118.

4.   Mariella, R., Jr., Sample preparation: the weak link in microfluidics-based biodetection. *Biomed. Microdevices* **2008,** *10*, 777-784.

5.   Kovarik, M. L.; Ornoff, D. M.; Melvin, A. T.; Dobes, N. C.; Wang, Y.; Dickinson, A. J.; Gach, P. C.; Shah, P. K.; Allbritton, N. L., Micro Total Analysis Systems: Fundamental Advances and Applications in the Laboratory, Clinic, and Field. *Anal. Chem.* **2013,** *85*, 451-472.

6.   Augusto, F.; Hantao, L. W.; Mogollón, N. G. S.; Braga, S. C. G. N., New materials and trends in sorbents for solid-phase extraction. *T. Anal. Chem.* **2013,** *43*, 14-23.

7.   Kim, J.; Johnson, M.; Hill, P.; Gale, B. K., Microfluidic sample preparation: cell lysis and nucleic acid purification. *Integr. Biol.* **2009,** *1*, 574-586.

8.   Nge, P. N.; Pagaduan, J. V.; Yu, M.; Woolley, A. T., Microfluidic chips with reversed-phase monoliths for solid phase extraction and on-chip labeling. *J. Chromatogr. A* **2012,** *1261*, 129-135.

9.   Sun, X.; Yang, W.; Pan, T.; Woolley, A. T., Affinity Monolith-Integrated Poly(methyl methacrylate) Microchips for On-Line Protein Extraction and Capillary Electrophoresis. *Anal. Chem.* **2008,** *80*, 5126-5130.

10.   Żwir-Ferenc, A.; Biziuk, M., Solid phase extraction technique–trends, opportunities and applications. *Pol. J. Environ. Stud.* **2006,** *15*, 677-690.

11.   Kutter, J. P., Liquid phase chromatography on microchips. *J. Chromatogr. A* **2012,** *1221*, 72-82.

12.   Svec, F.; Lv, Y., Advances and recent trends in the field of monolithic columns for chromatography. *Anal. Chem.* **2014,** *87*, 250-273.

13.   Liu, K.; Aggarwal, P.; Lawson, J. S.; Tolley, H. D.; Lee, M. L., Organic monoliths for high-performance reversed-phase liquid chromatography. *J. Sep. Sci.* **2013,** *36*, 2767-2781.

14.   Sahore, V.; Kumar, S.; Rogers, C. I.; Jensen, J.; Sonker, M.; Woolley, A. T., Pressure-Actuated Microfluidic Devices for Electrophoretic Separation of Pre-Term Birth Biomarkers (in preparation). *Anal. Bioanal. Chem.* **2015**.

6. EVALUATION OF AN INTEGRATED MICROFLUIDIC SOLID-PHASE EXTRACTION AND SEPARATION MODULE

6.1 INTRODUCTION

Analytical techniques are often insensitive to analytes in their crude form. [1-3] Therefore, sample preparation is an essential step in analysis and can involve processes such as sample dissolution, matrix removal, enrichment, and chemical derivatization.[4] A typical separation analysis may involve more than ~60% of the time in sample preparation and require large quantities of solvent (~9x more than the sample volume) and breakable glassware.[5-7] Integrating sample preparation with separation techniques on a microfluidic chip can address these problems;[8-9] however integration is difficult.[10] Solid-phase extraction (SPE) is a common, widely used, and well-studied sample purification and extraction technique for clinical, biological, environmental and food studies.[11] The use of SPE has been growing over liquid-liquid extraction in recent years because SPE offers simplicity, lower organic solvent consumption (~70% less), and 2x faster speed.[12-13]

The use of on-chip SPE in microfluidics allows enrichment of analyte and can improve detection limits.[14-15] Several researchers have integrated SPE and separation techniques in a microfluidic device. Ramsey et al.[15] packed C18-coated silica beads in a microchannel to make an SPE column and integrated it with micellar electrokinetic chromatography separation on a microchip. Particle packing required porous plug polymerization in the microchannel to act as a frit. This integrated device performed an automated sequence of extraction, elution, injection, separation and detection of two model fluorescent dyes in less than 5 min. However, more complex and biologically relevant analytes were not demonstrated. Foote et al.[16] used a porous silica membrane to concentrate fluorescently labeled proteins and then separated the enriched proteins

by microchip gel electrophoresis. However, protein was labeled off-chip, which is the most time-consuming step in sample preparation for laser induced fluorescence detection. Long et al.[17] used a C18-bead-packed micro SPE column to enrich rhodamine 123 and FITC-labeled ephedrine in a polydimethylsiloxane (PDMS) device. Enriched samples were injected by applying a pulse of voltage through a nonporous membrane separating the SPE column and separation channel. However, off-chip labeled simple molecules were demonstrated, two external syringe pumps were needed for fluid handling, and the SPE column required frits and particle packing. Kang et al.[18] demonstrated online extraction, electrophoretic separation, and electrochemical detection of dopamine in an integrated multilayer device. A polymeric monolith was fabricated in PDMS and micro valves were used to control fluid flow. However, the device was operated using an external pump, and the extracted sample was eluted into a reservoir that caused sample dilution before injection. In summary, previously reported studies on integration of sample preparation and separation demonstrated simple model analytes, off-chip fluorescent labeling, and external pumps for flow. In contrast, a truly integrated microfluidic device should perform all sample analysis steps including extraction, enrichment, labeling, and separation on a single microchip with on-chip fluid control.

In microfluidic devices, liquids can be manipulated or handled using electrokinetic or pressure-based methods.[19] Both methods have their merits and demerits. For example, device fabrication is simple and only requires voltage controllers for electrokinetic operation, but this method is limited by analyte charge bias, Joule heating, and sensitivity to variations in both fluid composition and channel wall coatings.[19-20] On the other hand, in pressure-driven systems, a wide range of fluids can be pumped with precise control of fluid volumes, and injection is not biased.[20-21] There are many types of pumps for pressure-driven operation in microfluidics; they involve

membranes, electroosmotic flow (EOF), electrohydrodynamics, magnetohydrodynamics or external components.[21] Magnetohydrodynamic and EOF pumps cannot be used for pumping nonionic liquids, and require either magnets or applied voltages for operation. Use of external pumps counteracts the ideal of miniaturization in microfluidics. In contrast, membrane-actuated peristaltic pumps allow pumping of precise fluid volumes and easy integration into microfluidic devices. Flow rates and direction are also easy to control with peristaltic pumps. Therefore, in this study, a membrane-actuated peristaltic pump and pneumatic valves are used to allow pressure-actuated sample handling and manipulation.

Here, acrylate-based monoliths with octyl (C8) surface functional groups are used for on-chip SPE of proteins and peptides. Extracted protein is derivatized on-chip with fluorescent dyes to enable detection. On-chip extracted and labeled ferritin (Fer) samples are separated in a microchip electrophoresis (µCE) module. This study demonstrates integration of sample preconcentration, fluorescent labeling, and separation all on a single platform.

6.2 MATERIALS

Food dyes (Great Value, Walmart, Bentonville, AR) are filled into microfluidic channels for visual inspection of device operation. Solenoid valves (Clippard, Cincinnati, OH) connected to the building compressed air supply are used to actuate on-chip valves. The control channel and solenoid are connected using microbore polytetrafluoroethylene (PTFE) tubing (0.022" ID x 0.042" OD, Cole Parmer, Vernon Hills, IL) and hypodermic stainless steel pins (0.025" OD x 0.018" ID x 0.394" long, Type 304, New England Small Tube, Litchfield, NH). Hydroxypropylcellulose (HPC), phenylalanine-alanine (FA), and glycine-glycine-tyrosine-alanine (GGYR) are obtained from Sigma Aldrich, St. Louis, MO. Fer is purchased from EMD Millipore, Billerica, MA. Fluorescein isothiocyanate (FITC) and Alexa Fluor 488 5-tetrafluorophenyl ester

(ALF), obtained from Life Technologies, Carlsbad, CA, are used to fluorescently label samples. The fluorescent labeling procedure, described in Chapter 2.2.1, is used to label Fer with FITC and ALF. FA and GGYR are labeled as follows: sodium bicarbonate buffer (BCB, 100 mM) is prepared by dissolving 420 mg NaHCO$_3$ (EMD Chemical, Gibbstown, NJ) in deionized (DI) water, and the pH is adjusted to 9.1, as recommended for overnight labeling, using 6 M NaOH (Spectrum, Gardena, CA). FA and GGYR solutions are prepared in BCB, each containing 10 mM peptide and 1.6 mM FITC. Peptide and FITC mixtures are incubated overnight at room temperature for labeling. For on-chip labeling, BCB is diluted to 10 mM and the pH is raised to 9.8 (higher pH favors rapid on-chip labeling). Solid-phase elution buffers are prepared containing 100, 90, 70, 50, and 30% v/v acetonitrile (ACN, Sigma Aldrich) in 10 mM BCB. Electrophoretic separations are performed using 20 mM BCB (pH 9.8), 30 mM NaCl, and 0.05% HPC.

6.3 METHODS

6.3.1 Device characterization

Devices fabricated in Chapter 5 are initially tested using food dye solutions prepared in 10 mM BCB and 85% ACN. Device design and operational aspects such as pneumatic valve actuation pressure, pump flow rate, dead volume, flow through monolith and sample plug capture are studied. Figure 6.1A-B shows the SPE module layout; the control channels are filled with green dye, and three inlet fluidic channels lead into a 0.53-mm-wide and 1-mm-deep cyclic olefin copolymer (COC) reservoir. Features in the control layer regulate the flow through fluidic channels; three control channels placed in series form a peristaltic pump as shown in Figure 6.1B. Figure 6.1C shows the SPE experimental setup; the green dye filled tubing connects control reservoirs with external solenoids that cause valve actuation. Solenoid operation is controlled using a computer program written in LabVIEW.
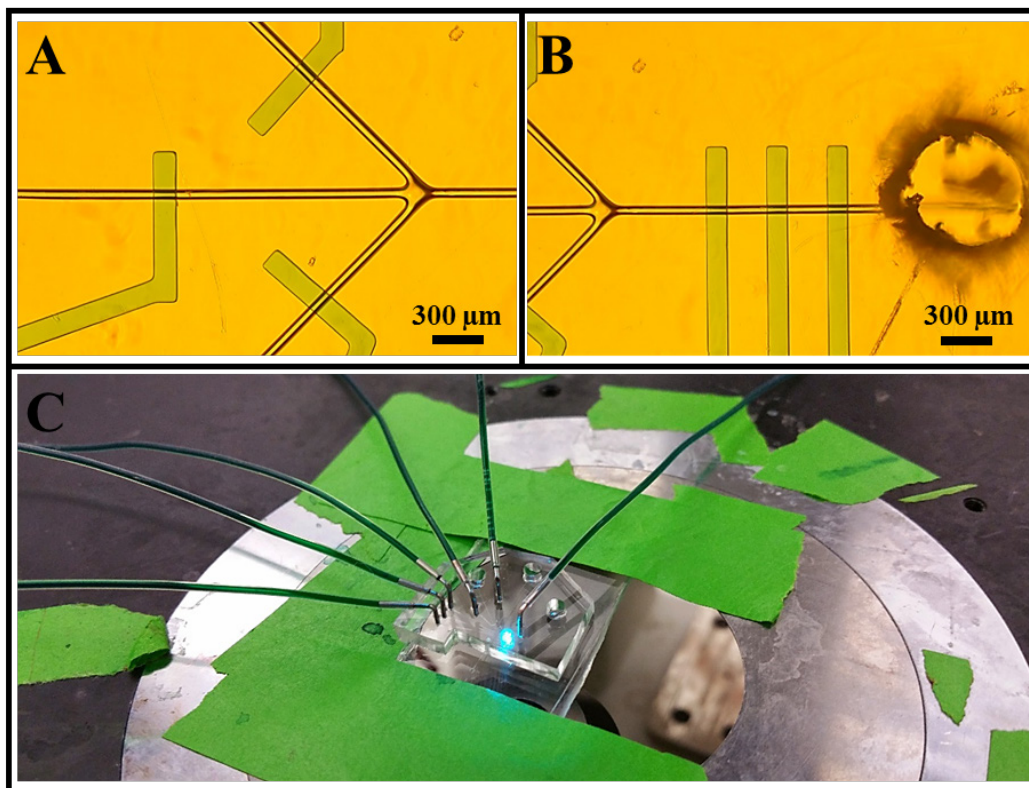
Figure 6.1 Initial SPE module design. (A) Photograph showing sample, buffer, and eluent inlet channels and pneumatic valves. (B) Photograph showing three-valve peristaltic pump and fluidic channel connected to a reservoir to access a C8 monolith in the COC layer. (C) Final device on an inverted microscope, connected to external tubing and solenoids (not shown) to actuate valves.

Figure 6.2A shows a schematic and photograph of open fluidic and control channels separated with a 6-8 µm thick flexible membrane. Several fluidic channel heights (7-16 µm) are tested for a 65-µm-wide fluidic channel, and 25-50 psi is applied in the control channel to completely close pneumatic valves. Figure 6.2B shows a schematic and photograph of membrane actuation into the fluidic channel, which stops the flow. Fluidic channel inlet reservoirs are filled with red dye in 85% ACN, and the pump is actuated at 40 Hz for 8 h to evaluate material robustness.
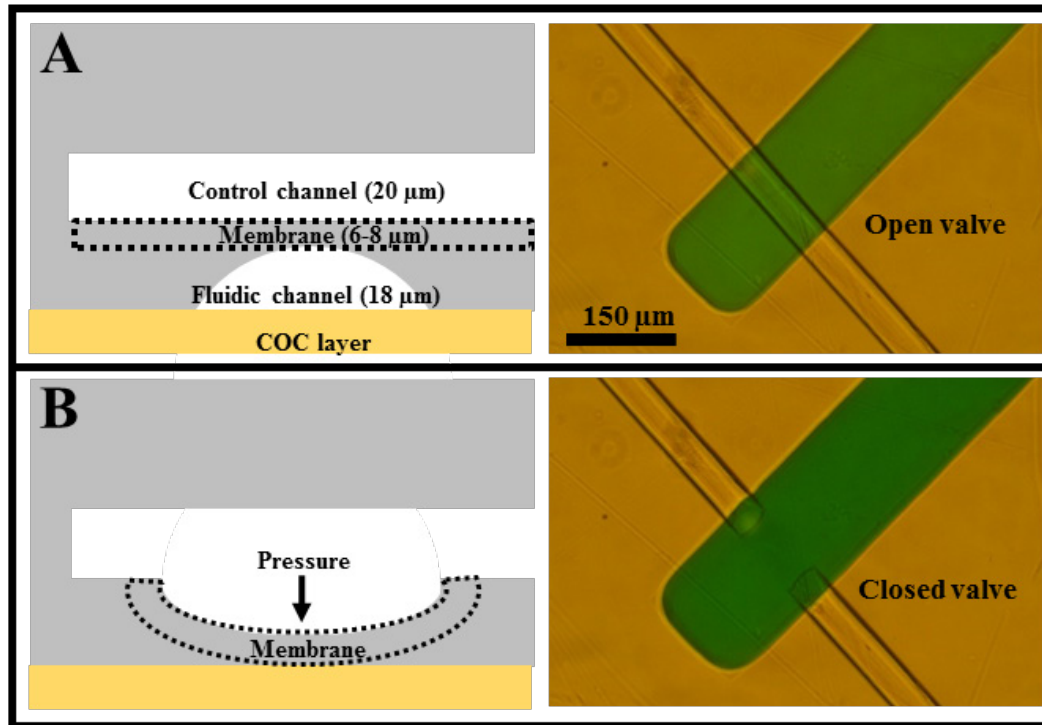
Figure 6.2 Pneumatic valve structure. (A) Open valve configuration (left) schematic showing vertical cross-section, and (right) photograph of an actual valve. (B) Closed valve configuration (left) schematic, and (right) photograph of an actual valve.

ACN and buffer flow through the monolith is tested in the SPE module with a three-valve pump. The pump actuated at 40 Hz is used to flow red dye prepared in 85% ACN through the monolith for 15 min, and rinse solution containing 85% ACN for 1 h to elute. Next, green dye prepared in 10 mM BCB is pumped for 30 min to replace 85% ACN in the monolith structure.

The SPE module is integrated with the separation module to allow on-chip extraction, labeling and separation. Three- and five-valve peristaltic pumps are fabricated on chip using 250-µm-wide control channels, spaced at a 120 µm distance. Figures 6.3A-B show a five-valve peristaltic pump and a set of four pneumatic valves built in the integrated design. Four pneumatic valves are placed around the injection intersection with a 300 µm distance from the intersection to

capture the sample plug prepared in the SPE module. Figure 6.3C shows the experimental setup used for integrated device operation. Three- and five-valve pump flow rates are calculated by recording the time to pump different solutions from the intersection to the sample waste reservoir (4 mm). Pumps are actuated at 10 and 20 Hz frequencies with ~30 psi applied.
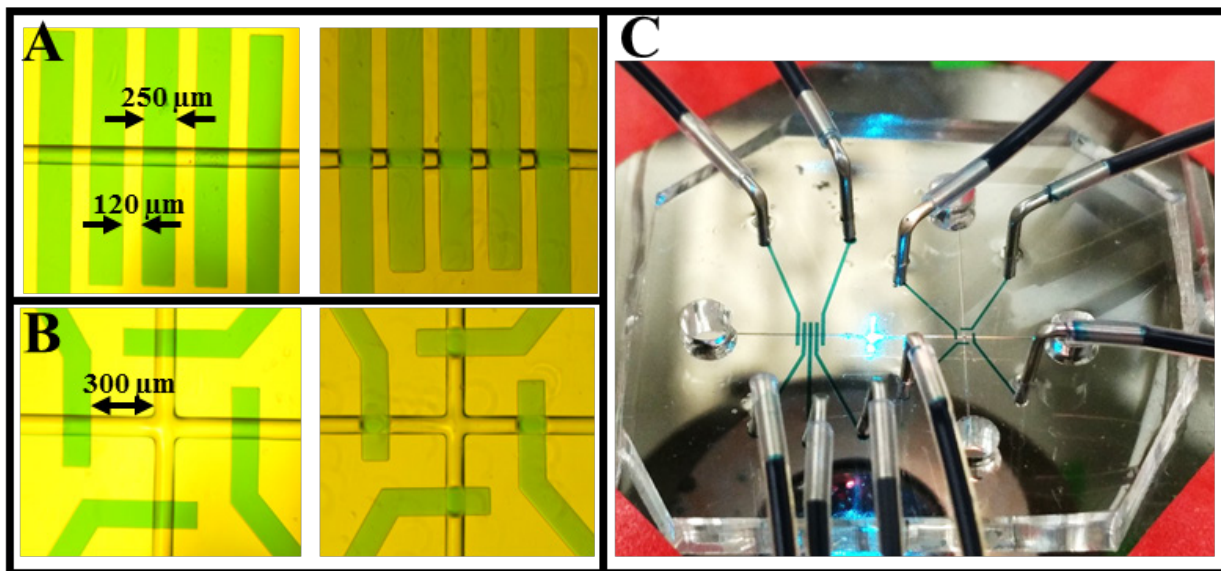
Figure 6.3 SPE and separation module integrated device. (A) Five-valve peristaltic pump in the SPE module with (left) open and (right) actuated valves. (B) Pneumatic valve arrangement surrounding the intersection in the separation module; (left) open and (right) actuated. (C) Integrated device on a microscope stage with dye-filled control channels connected to external tubing.

6.3.2 Protein and dye retention and elution

Fluorescent dye (FITC and ALF) retention and elution from a C8 monolith are studied to select the least retained dye for on-chip labeling. A five-valve on-chip peristaltic pump operates at 10 Hz frequency, and valves are actuated with ~30 psi to flow solutions. The C8 monolith surface is conditioned by passing 90, 50 and 30% ACN solutions through the monolith for 5 min followed by a 5 min 10 mM BCB (pH 9.8) rinse. FITC (1 μM) prepared in BCB is loaded onto the column

for 10 min, and unretained FITC is rinsed off using BCB. Next, the column is rinsed successively with eluents composed of increasing amounts of ACN (30, 50, 70, 90, and 100%) in BCB. A similar experiment is performed on the same device by replacing FITC with 1 μM ALF. Under illumination from a 488 nm laser, monolith images at each step are recorded using a Photometrics CoolSNAP HQ2 (Tucson, AZ) cooled CCD camera with 500 ms exposure. Furthermore, to study the change in monolith fluorescence intensity, average values are measured by drawing a box (approx. 400 x 110 pixel^2) around the monolith using ImageJ software.

Prelabeled Fer is used to study Fer retention and elution on a C8 monolith in the SPE module. Here, a three-valve peristaltic pump is operated at 40 Hz, and valves are actuated with ~30 psi. The monolith surface is conditioned as described in the previous paragraph. FITC-labeled Fer (500 nM) is loaded onto the monolith for 5 min and unretained Fer is rinsed off by flowing BCB. The captured Fer is eluted using eluents composed of increasing amounts of ACN (30, 50, 90 and 100%). Fluorescence images of monoliths are recorded using a CCD with 500 ms exposure time, as described above.

The effect of three- vs. five-valve pumps on Fer retention and elution in an integrated device is also studied. First, 200 nM prelabeled Fer is loaded onto a C8 column after column conditioning for 5 min using a five-valve peristaltic pump operated at 10 Hz, and ~30 psi applied pressure. The C8 column is rinsed with BCB and the captured protein is eluted by flowing 90% ACN through the column. Content eluted from the column is detected using a photomultiplier tube (PMT) detector (Hamamatsu, Bridgewater, NJ) at the injection intersection. A similar experiment is performed using a three-valve pump operated at 20 Hz, and ~30 psi pressure. 100 nM prelabeled Fer is loaded onto the column for 15 min and the captured Fer is eluted in 90% ACN.

6.3.3 Evaluation of acetonitrile effects on peak shape in the separation module

Eluent composed of different percentages of ACN in 10 mM BCB is used for eluting fluorescently labeled Fer from the C8 column and transports the sample into the separation module for separation. Therefore, 40 nM FITC samples are prepared in separation buffer with either 90, 70, or 50% ACN to study the effect of ACN concentration in the injection solution on analyte separation. All FITC solutions are tested in devices lacking a monolith. A three-valve peristaltic pump operated at 10 Hz and ~30 psi is used to inject sample into the injection intersection for 40 s. During injection, valves on the injection channel are kept open, but those on the separation channels are closed. Next, the sample plug is captured by closing the injection channel valves, followed immediately by opening the valves on the separation channel, and applying 1200 V along it. Fluorescence detection is performed at a 5 mm distance from the intersection using a PMT as described in Section 6.3.2, with the voltage set to 830 and 2x amplification.

6.3.4 Protein enrichment study

An integrated device with three-valve peristaltic pump is used for prelabeled Fer enrichment on the C8 monolith. The peristaltic pump is operated at 20 Hz, and the valves are actuated at ~30 psi. First, the C8 column is conditioned with eluents as described in Section 6.3.2. Prelabeled Fer (100 nM) is loaded onto the column for 10 min (~300 nL) and monolith fluorescence images are recorded after each minute. Next, the column is rinsed with 10 mM BCB for 4 min to wash away unretained Fer. Enriched Fer is eluted from the column using 90% ACN and captured at the injection intersection using the valves as described in Section 6.3.3. The captured plug is separated with 700 V applied down the separation column, and the fluorescence is recorded at 3 mm from the intersection with a PMT having a 780 V setting and 2x amplification. Finally, the column is rinsed with 100% ACN to completely free the labeled Fer from the C8

monolith. Electrophoretic separation of 100 nM Fer is also performed under similar conditions using a pump and valve integrated separation module lacking the C8 monolith; fluorescence is recorded 5 mm from the intersection.

Enrichment of model peptides (FA and GGYR) on the C8 column is also studied in an integrated device. A three-valve peristaltic pump is operated at 20 Hz, and ~30 psi is used for actuating the valves and pump. FA and GGYR (500 nM each) are loaded onto a preconditioned C8 monolith for 10 min and rinsed with 10 mM phosphate buffer (pH 7.2) to remove unretained peptides. The enriched peptides are eluted in 90% ACN and captured using four valves as described in Section 6.3.3. The captured plug is separated into FA and GGYR bands with 700 V applied along the column length. Fluorescence is detected 4 mm from the intersection using 1010 V as the PMT setting and 2x amplification. The same peptide mixture is also separated in the separation module without enrichment.

6.3.5 On-chip labeling

On-chip Fer labeling with FITC and ALF is performed in the integrated device shown in Figure 6.3C. All solutions are introduced from the same reservoir (left side) in the integrated device. The C8 column is conditioned, and 200 nM unlabeled Fer is loaded for 5 min (~700 nL) using a five-valve peristaltic pump. Pump operation parameters include 10 Hz actuation frequency and ~30 psi valve closing pressure. FITC (1 µM) prepared in 10 mM BCB (pH 9.8) is flowed through the column for 3 min (~400 nL) and allowed to react with retained Fer for 10 min under stopped flow conditions. Unreacted FITC is rinsed off the column using BCB for 2 min (~300 nL). The monolith column is rinsed with 50% ACN (~400 nL) to remove any unreacted FITC after the buffer wash. Labeled Fer is eluted from the column using 90% ACN. Finally, the column is rinsed with 100% ACN to completely elute any Fer left. A control experiment is run by omitting Fer

under similar conditions in the same device. Fluorescence images are recorded as described in Section 6.3.2 using a CCD camera with a 500 ms exposure time.

ALF is used to label Fer on-chip in the integrated device. First, 1 µM Fer is loaded onto a preconditioned C8 column (see Section 6.3.2 for details) for 7 min (~1 µL) using a five-valve peristaltic pump operated at 13.3 Hz with ~30 psi applied pressure. Next, 30 µM ALF prepared in 10 mM BCB (pH 10.0) is flowed through the column for 2 min (~300 nL) and allowed to react with Fer for 25 min. Unreacted ALF is rinsed off using BCB (~450 nL) and 30% ACN (~340 nL). Finally, the labeled Fer is eluted in 90% ACN, and LIF signal is recorded at the injection intersection as in Section 6.3.2 with the PMT set at 740 V and 2x gain. A control experiment is also run on the same device under similar conditions by omitting the Fer loading.

6.3.6 On-chip labeling and separation of ferritin in an integrated device

The schematic diagram shown in Figure 6.4 explains the operation of the integrated device for on-chip Fer labeling and µCE. All solutions are introduced from the same inlet reservoir using a five-valve peristaltic pump operated at 10 Hz and ~30 psi. Device operation involves conditioning the C8 column by flowing 100% ACN for 5 min (~700 nL), 50% ACN for 2 min (~300 nL), 30% ACN for 2 min (~300 nL), and finally BCB for 5 min (~700 nL). After column conditioning 1 µM of Fer is loaded for 10 min (~1.4 µL) using a five-valve peristaltic pump (Figure 6.4A). Next, 20 µM ALF is flowed through the column for 2 min (~300 nL) and allowed to react with the captured Fer for 25 min. Fer is labeled (Figure 6.4B) and unreacted dye is rinsed off using buffer (~700 nL) and 30% ACN (~300 nL). Labeled Fer is eluted from the column in 90% ACN into the injection intersection. Valves are opened on the injection channels and closed on the separation channel during Fer elution. All four valves are closed when the eluted Fer reaches the intersection at ~20 s and the plug is captured (Figure 6.4C). Finally, the captured Fer plug is

separated by opening valves on the separation channel and applying 500 V (Figure 6.4D). LIF as described in Section 6.3.3 is used to detect the separated Fer peak 3 mm down from the intersection, with a PMT setting of 850 V and 2x amplification. Fluorescence images of the monolith are also recorded using a CCD with 500 ms exposure time as described in Section 6.3.2.
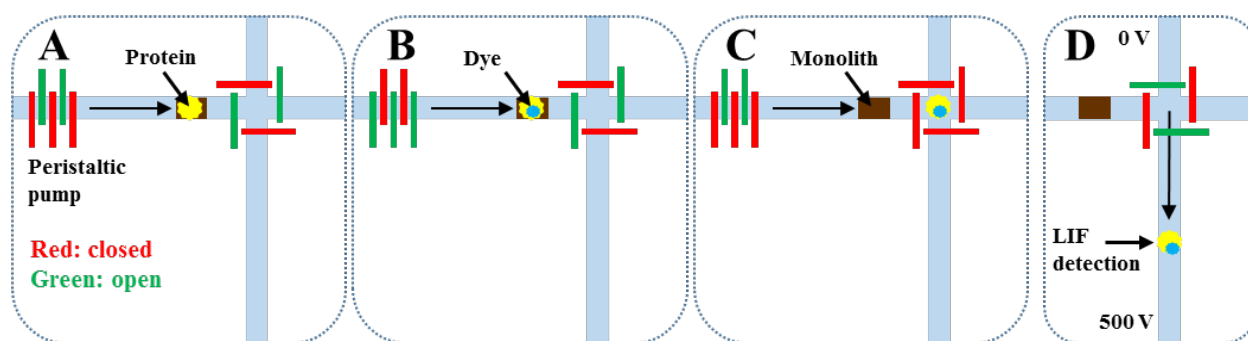

Figure 6.4 Schematic showing operation of an integrated device. (A) Protein (1 µM) is loaded onto a C8 column using the pump (~10 min). (B) Fluorescent dye (20 µM) is pumped through the column and the protein/dye mixture is incubated for covalent labeling (~25 min). (C) Labeled protein is eluted using 90% ACN and captured at the intersection using a set of four pneumatic valves (~1 min). (D) The captured plug is separated using µCE and detected using LIF (~1 min).

6.4 RESULTS AND DISCUSSION

Preliminary experiments to optimize the device design were performed using food dyes to visualize flow. Initial studies included PDMS compatibility with ACN, channel dimension optimization, pump flow rate measurements, and observation of flow through a monolith. The peristaltic pump was used to pump 85% ACN for 8 h to observe any effects on the cured PDMS. I found that PDMS didn't swell in ACN, the pump was still operational after 8 h of actuation, and no PDMS delamination was observed. Hence, ACN was compatible with PDMS devices. In the initial SPE module, shallower (<9-µm height) fluidic channels had low device yields due to blocking with curing agent during device bonding. On the other hand, taller (>10 µm) channels

131

required valve actuation pressures above 40 psi, which often caused device delamination. Therefore, ~9 µm tall fluidic channels were used as they needed valve actuation pressures <40 psi and channel blocking with curing agent was minimal. In the initial SPE module, the three-valve pump formed by placing three 150-µm-wide control channels 150 µm apart generated a 12 nL/min flow rate for 85% ACN solution and filled the 1-mm-deep COC reservoir in ~30 min. Solutions with dye flowed through a monolith in the SPE module (see Figure 6.5), demonstrating that the monolith was porous and the on-chip pump could move liquid through.
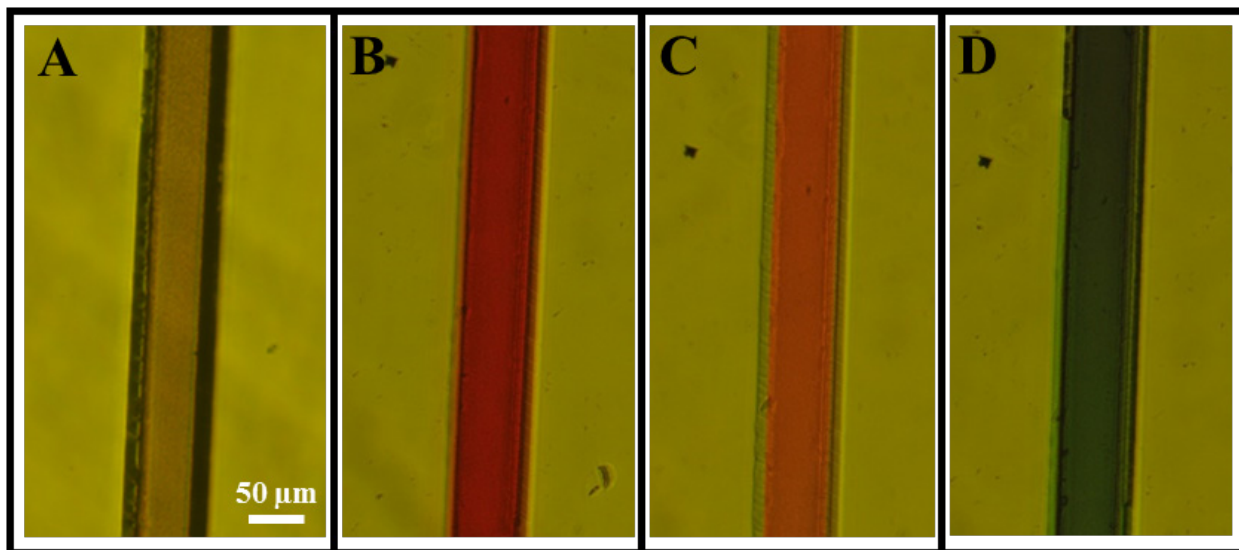

Figure 6.5 Study of flow through a C8 monolith in the SPE module. (A) Empty monolith, (B) red dye flow, (C) 90% ACN elution of red dye, and (D) green dye flow.

In the integrated design, the fluidic channel was 120 µm wide and 18 µm tall to prevent channel blockage during bonding. To increase the pump flow rate in the integrated device, 250-µm-wide control channels were fabricated and five control channels were placed with a 120 µm inter-feature distance to build a five-valve pump. The three-valve pump having dimensions similar to the five-valve pump was also formed in the integrated design for flow rate comparison. Wider control channels and a taller fluidic channel resulted in larger displaced solution volumes with

each valve actuation, and thus produced higher flow rates, as shown in Table 6.1. Such a configuration also allowed valve actuation pressures <35 psi. The differences in flow rates of different solutions for three- and five-valve pumps at 20 Hz actuation were caused by incomplete valve sealing due to the increase in fluid viscosity when the ACN content was decreased. Three-valve pump flow rates at 10 Hz actuation for different solutions did not change significantly because membrane dynamic deflection was slower than the actuation rate. Moreover, the use of thinned (80-100-μm-thick) COC and narrower (200-μm-wide) through holes decreased the dead volume so the COC reservoir filled in less than 1 min (140 nL/min). The trident fluidic channel design (Figure 6.1A) was dropped from the SPE module in these studies on integration with the separation module to simplify the fabrication. This simpler design lacked multiple inlets which required solution replacement in the single inlet reservoir.

Table 6.1 Three- and five-valve peristaltic pump solution flow rates at different actuation frequencies.

Solution	20 Hz operation	10 Hz operation
Three valves		
ACN	121 nL/min	*
50% ACN+ 50% Buffer	56 nL/min	*
30% ACN+ 70% Buffer	40 nL/min	*
Buffer	30 nL/min	*
Five valves		
90% ACN + 10% buffer	331 nL/min	135-140 nL/min
50% ACN+ 50% Buffer	276 nL/min	135-140 nL/min
30% ACN+ 70% Buffer	207 nL/min	135-140 nL/min
Buffer	165 nL/min	135-140 nL/min

* Solution flow rate at 10 Hz actuation for the three-valve pump was not measured because flow was very slow at 20 Hz operation. Each value given is the average of two measurements done in the same device.

In Figure 6.6A, background-subtracted fluorescence intensities of FITC and ALF on a C8 monolith as a function of retention/elution conditions are plotted. Fluorescence on the monolith for ALF retention was higher for the initial 2 min, probably because the ALF fluorescence quantum yield is higher than for FITC.[22] After 5 min of loading, the signal from FITC retained on the column exceeded that for ALF, likely because FITC is more hydrophobic and thus more retained than ALF. As a result of this hydrophobicity difference, FITC was retained on the column, while most

134

of the ALF eluted during the buffer rinse. After rinsing the column with 30% ACN, the ALF intensity decreased slightly, but did not decrease much more upon rinsing with solutions composed of higher ACN percentages. In contrast, the retained FITC intensity gradually decreased on increasing the ACN content in the eluent.

FITC-labeled Fer retention and elution was also studied on a C8 monolith. As shown in Figure 6.6B, the monolith fluorescence intensity increased as the Fer loading time changed from 3 to 5 min. Longer Fer loading resulted in retention of more Fer on the column due to the hydrophobic interaction between Fer and the C8 functional groups. Buffer, 30% ACN, and 50% ACN rinses had a small effect on the column fluorescence because Fer was strongly retained. However, the column fluorescence decreased significantly when the monolith was rinsed with 90 and 100% ACN. The high organic content of the 90-100% ACN eluent reduced non-polar interactions between Fer and the C8 functional groups and released the retained Fer. From this study of dye and Fer retention/elution on C8 monoliths, I concluded that ALF would be a good molecule for on-chip Fer labeling. Additionally, ALF conjugates are more photostable and provide a higher fluorescence quantum yield than FITC, further supporting this choice.[22] Rinsing the column with eluent containing up to 50% ACN elutes most of the ALF without affecting Fer retention; thus, the elution of on-chip labeled Fer in 90% ACN can be done with minimal free dye.
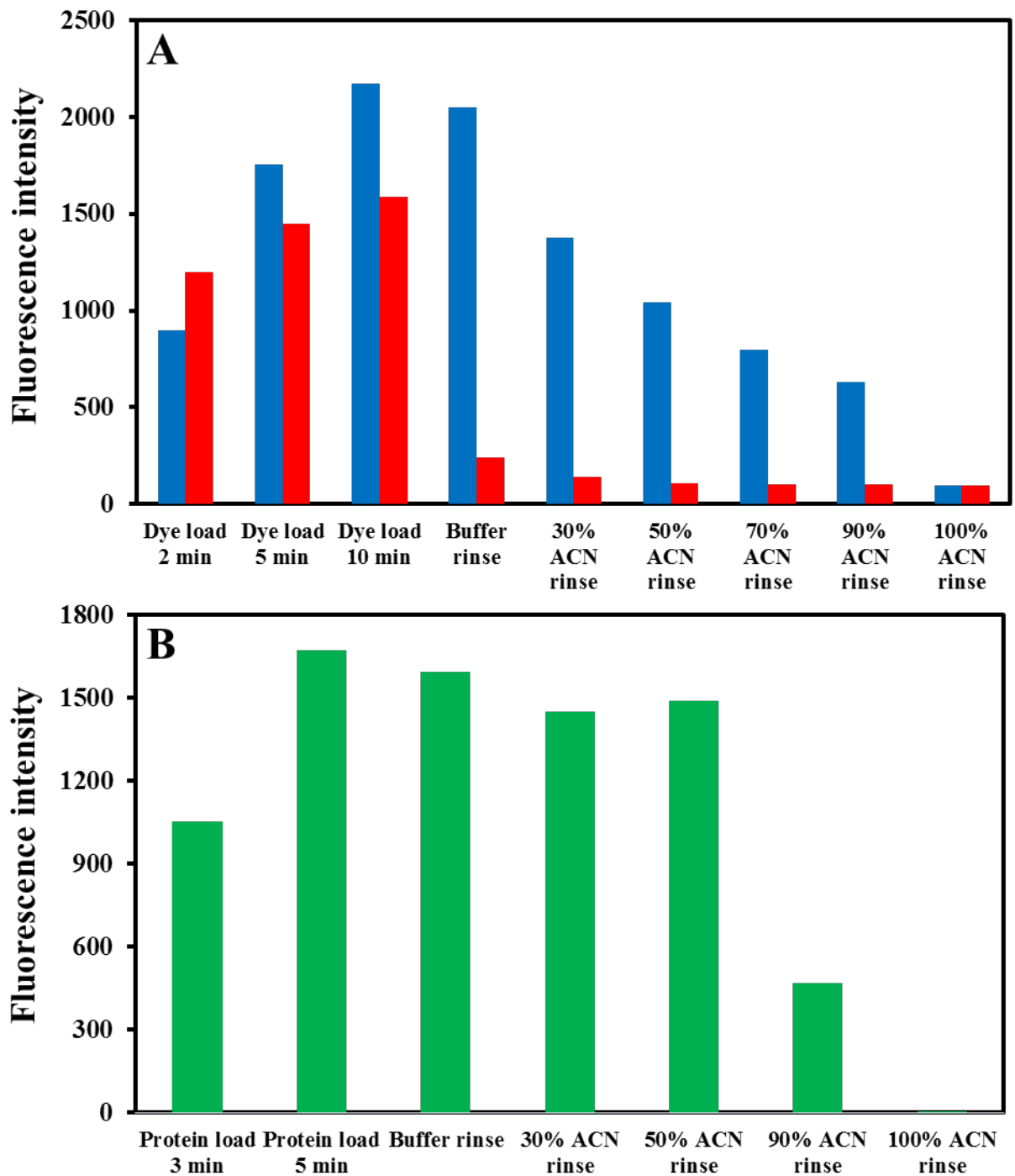
Figure 6.6 Evaluation of dye and Fer retention/elution in a C8 monolith in an SPE unit. (A) Background-subtracted fluorescent intensity on a C8 monolith for retention and elution of ALF (red) and FITC (blue). (B) Background-subtracted fluorescent intensity of prelabeled Fer on a C8 monolith under conditions for retention and elution.

Prelabeled Fer was loaded onto a C8 monolith using three- and five-valve peristaltic pumps in integrated devices (Figure 6.3C). Fluorescence images on the C8 monolith at different stages of the process are shown in Figure 6.7A. Loading of the labeled Fer on the C8 monolith increased fluorescence signal, while elution of the retained Fer from the monolith in 90% ACN lowered the monolith fluorescence. Fer eluted in 90% ACN using a five-valve peristaltic pump (blue trace in Figure 6.7B) resulted in a narrower, taller peak with a faster elution time. On the other hand, the Fer peak was broadened and eluted later when a three-valve pump (red trace in Figure 6.7B) was used. The faster flow rate produced by the five-valve pump compared to the three-valve pump (Table 6.1) reduced the longitudinal dispersion of the Fer band before its detection at the intersection. Narrower, taller peaks will allow capture of more of the eluted Fer at the intersection with a higher concentration, which should result in better separation in the μCE module. The noise in the peaks in Figure 6.7B is due to pulsatile flow of the peristaltic pump where photobleaching occurs during the time between actuations.
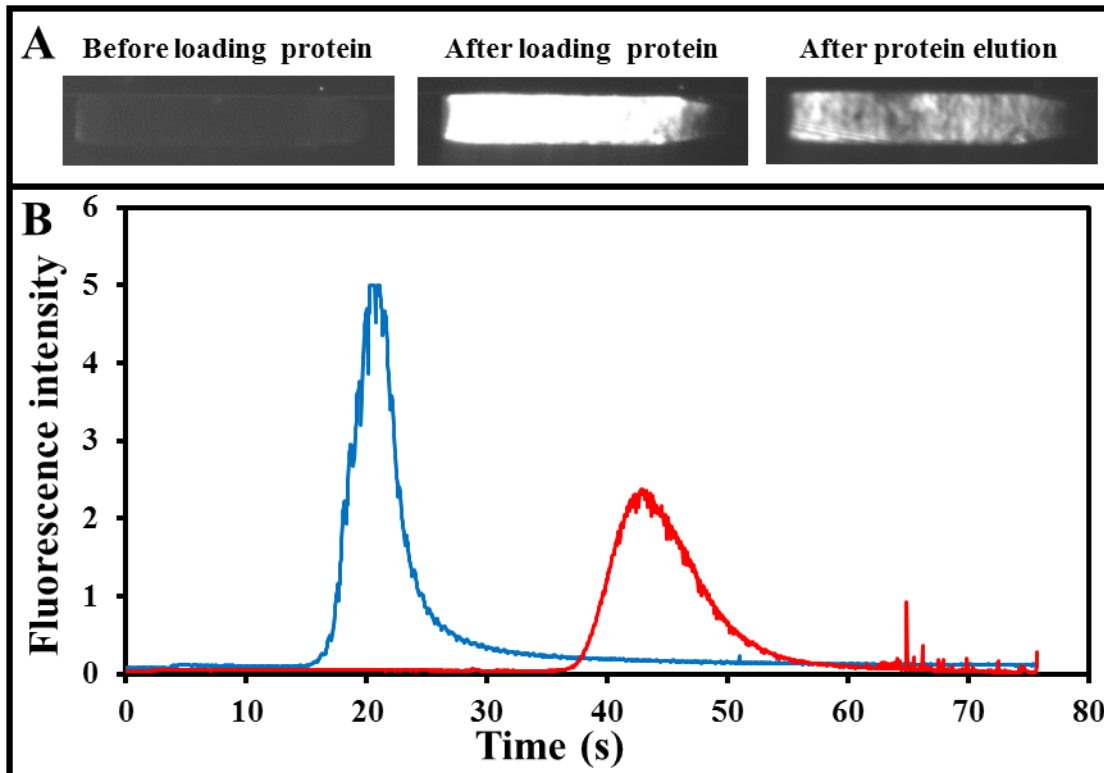
Figure 6.7 Fer retention and elution on a C8 monolith. (A) C8 monolith CCD images of fluorescence (left) before, (middle) after loading Fer, and (right) after a 90% ACN rinse using a five-valve pump. (B) Plots showing PMT detection (at the separation unit's intersection) of prelabeled Fer eluted in 90% ACN from the C8 monolith. One and two hundred nM Fer retention and elution were performed using (red) three- and (blue) five-valve peristaltic pumps, respectively.

Sample prepared in the SPE module is transported to the separation module in high ACN content eluent. Therefore, I evaluated the effects of ACN in the injected sample on separation quality using a model molecule (FITC). In Figure 6.8, FITC peak height increased and peak width decreased as the amount of ACN in the injected sample solution increased. Moreover, having ACN in the sample solution reduced the peak migration time by 40%. The presence of ACN in the sample plug lowered the conductivity and resulted in sample stacking, which produced narrower peaks, shorter migration times, and an increase in peak heights.
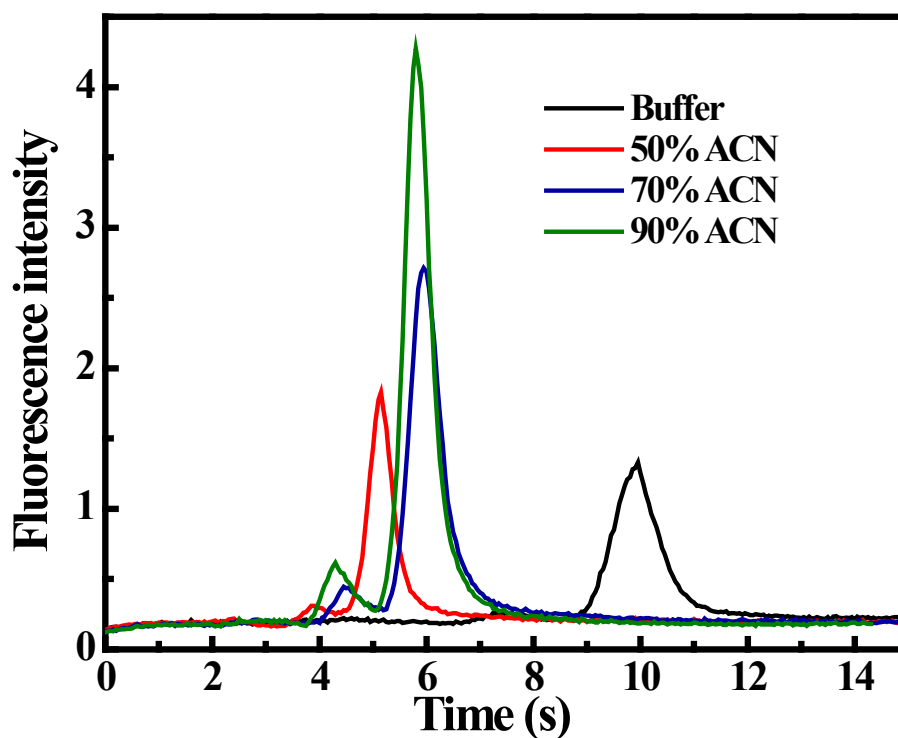
Figure 6.8 Microchip electropherograms showing differences in peak shape and migration of 40 nM FITC in different concentrations of ACN in the injected solution.

The enrichment capability of the SPE module was evaluated using labeled Fer. Fluorescent images on a C8 monolith were recorded under different Fer enrichment conditions (Figure 6.9A). Fluorescence became brighter as the Fer loading time increased, due to an increase in the number of Fer molecules captured. For quantitative comparison, monolith fluorescence was calculated from these images as described in Section 6.3.2 (see Figure 6.9B). Fluorescence increased steeply for the first 4 min and then gradually until 8 min; after 8 min the fluorescence reached a plateau. The rapid increase in fluorescence intensity at the beginning of Fer loading resulted from the availability of a large number of C8 functional groups to capture Fer. Over time, the number of available surface functional groups decreased due to retained Fer, leading to a more gradual

increase in Fer retention. From 8-10 min, almost all the available sites were occupied by retained Fer (i.e., column saturation), so further retention was limited. A buffer rinse had almost no effect on monolith fluorescence because Fer was strongly retained on the C8 column. However, monolith fluorescence significantly decreased on rinsing the monolith with 90% and 100% ACN. Increased organic content in the eluent displaced the Fer molecules from the C8 functional groups. I also quantified Fer enrichment on the C8 monolith using fluorescence intensity measurements. The fluorescence of 100 nM Fer in a channel of the same dimensions but lacking monolith was measured as described in Section 6.3.2. The ratio of Fer fluorescence on the monolith after the buffer rinse step to that in the channel lacking a monolith showed that Fer was enriched ~80-fold on the C8 column. Such sample enrichment can help in improving detection limits.
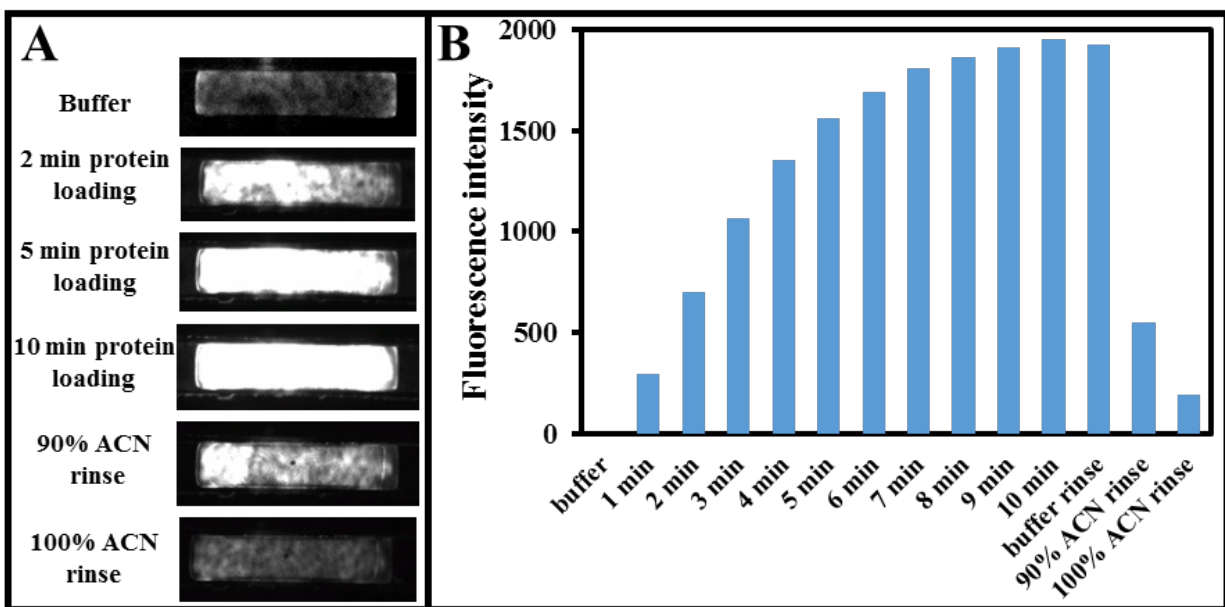
Figure 6.9 Fer retention with time in a C8 monolith. (A) Fluorescent CCD images under different conditions of Fer retention or elution. (B) Plot showing fluorescent intensity on a C8 monolith with different loading times and after elution.

I next demonstrated extraction, enrichment, and elution coupled to electrophoretic separation in an integrated device. Labeled analyte was captured on the monolith, eluted in 90% ACN into the injection intersection, and then injected and separated by µCE. Figure 6.10A shows separation of 100 nM Fer after on-chip enrichment; Figure 6.10B shows 100 nM Fer separation without enrichment. The Fer peak height increased ~70x after enrichment. Fer enrichment in the electrophoretic separation was very close to the 80x enrichment factor calculated using monolith fluorescence. The enriched Fer peak migration time was faster compared to the one for Fer without enrichment because detection was performed close to the injector. Moreover, the presence of ACN in the enriched Fer plug decreased the migration time as shown in Figure 6.8. A mixture of FA and GGYR was also enriched on a C8 column, eluted, injected, and separated by µCE similar to Fer. Figure 6.10C shows separation of FA and GGYR after on-chip enrichment; Figure 6.10D

shows FA and GGYR separation without enrichment. The FA and GGYR peaks increased approximately 3- and 11-fold after enrichment, respectively. FA and GGYR peptides are smaller than Fer, are not as hydrophobic, and are less retained, resulting in lower enrichment. Overall, the integrated device showed promising results for peptide and protein enrichment for electrophoretic separation.
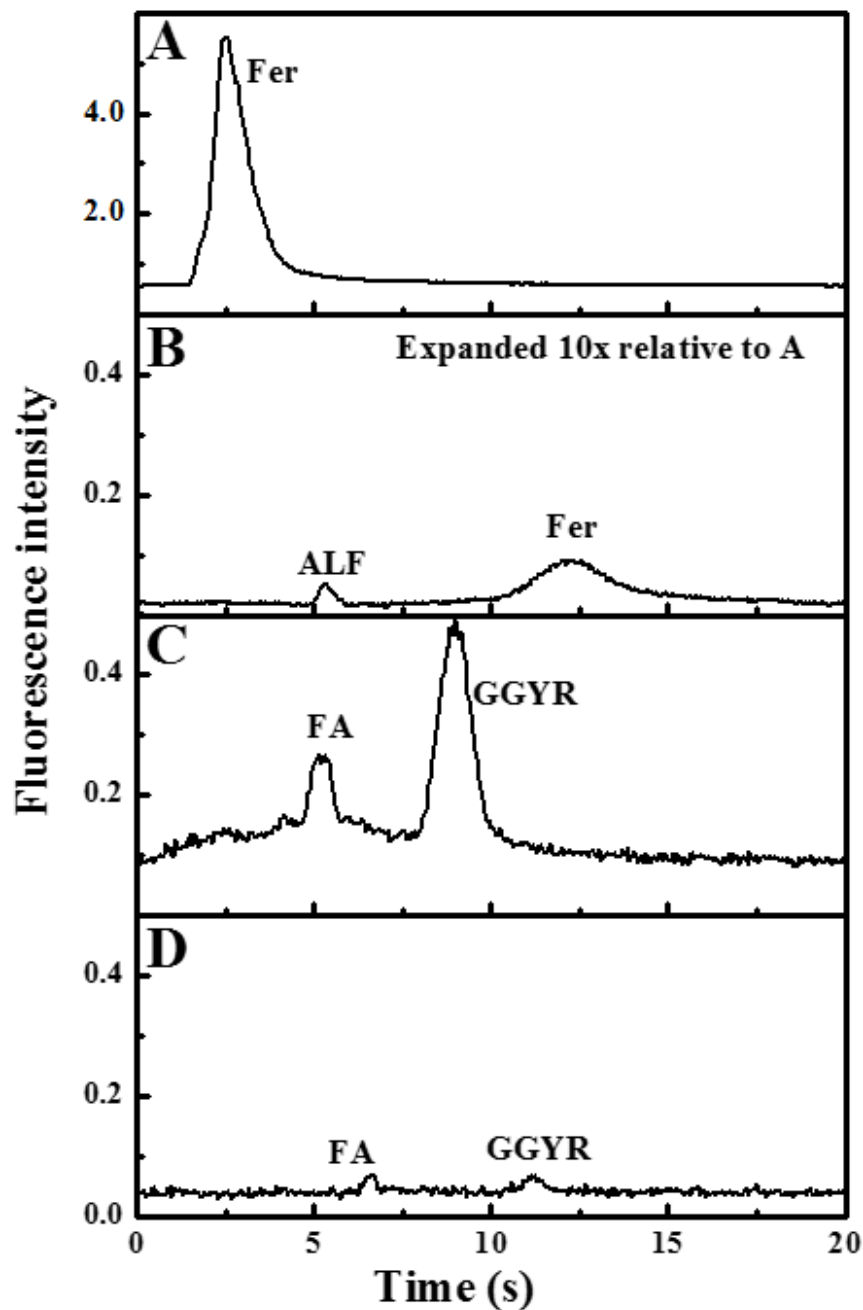
Figure 6.10 Microchip electropherograms showing the effects of on-chip sample enrichment. (A) Electrophoretic separation of Fer (100 nM) with enrichment on a C8 monolith and (B) without enrichment. (C) Electrophoretic separation of a mixture of two model peptides, FA and GGYR (both 500 nM), with enrichment on a C8 monolith and (D) without enrichment.

On-chip Fer labeling with FITC and ALF was evaluated in an integrated device. Figure 6.11A shows fluorescence images of a monolith with or without retained Fer during various steps of on-chip labeling using 1 µM FITC. Monolith fluorescence was measured as described in Section 6.3.2 and plotted as function of labeling conditions (Figure 6.11B). The monolith fluorescence intensities with or without Fer were almost the same after loading FITC. However, on rinsing the column with buffer and eluent with 50% organic content, fluorescence on monoliths without Fer loaded decreased more compared to ones with loaded Fer. The retained Fer on the monolith reacted with FITC covalently, which reduced the elution of FITC and resulted in higher fluorescence signal compared to a column without Fer. The intensity differences on these columns confirmed the labeling of Fer.
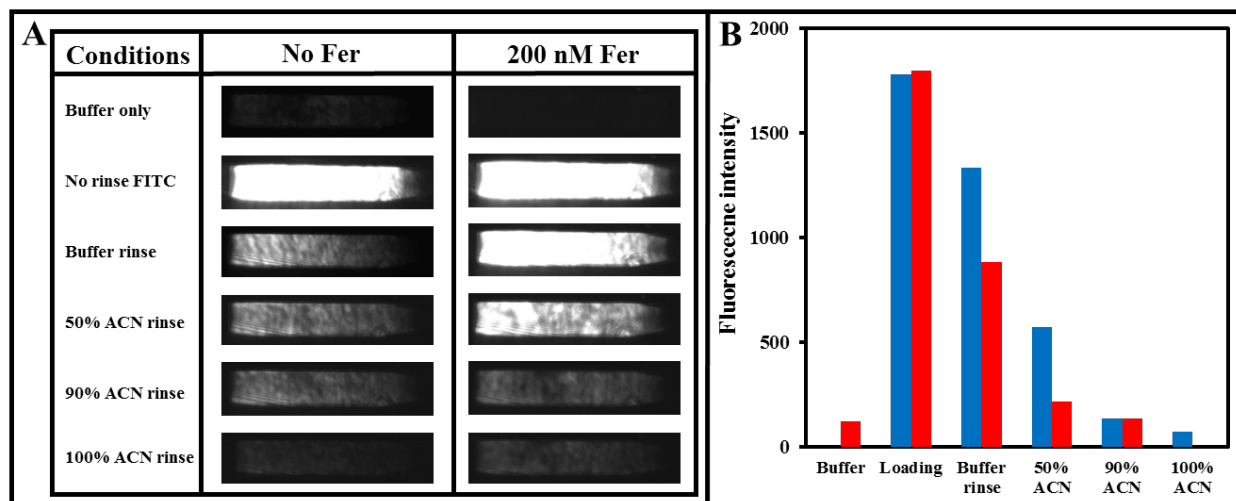
Figure 6.11 On-chip labeling of 200 nM Fer using 1 µM FITC. (A) CCD images of fluorescence on the C8 monolith under different conditions of labeling. (B) Fluorescent intensity measurements on the C8 monolith during the FITC labeling process for columns having (blue) 200 nM Fer or (red) no Fer loaded.

Fer was also labeled with ALF in an on-chip monolith, and the eluted band was detected at the intersection using LIF, as described in Section 6.3.5. Figure 6.12 shows the fluorescent bands

eluted in 90% ACN from a monolith with 1 µM Fer loaded (black trace) or no Fer loaded (red trace). A much larger peak resulted from the elution of labeled Fer, compared to when no Fer was loaded and only ALF retained after the rinse was eluted. In future studies, either a lower ALF concentration should be used or the column should be rinsed longer after the labeling reaction to limit the amount of interfering unreacted ALF.
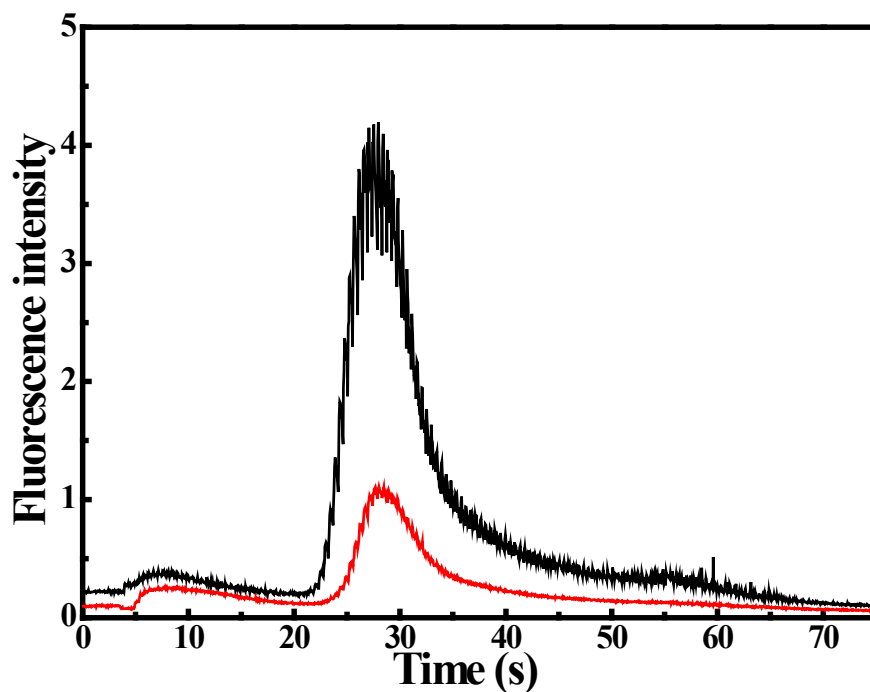
Figure 6.12 PMT detection of fluorescence from pressure-based elution of 30 µM ALF 488 loaded on a C8 monolith in the absence of Fer (red), and of 1 µM Fer labeled on-chip with 30 µM ALF 488 (black).

Finally, Fer was labeled on-chip using ALF, and then the labeled Fer was separated in the separation module to demonstrate successful integration of SPE, labeling and electrophoresis. Figure 6.13A-B shows monolith fluorescence images and average intensity measurements under different on-chip Fer labeling conditions. Here, the column was rinsed longer (5 min) with BCB and 30% ACN than in Figure 6.12 to remove more of the unreacted ALF. After labeling of 1 µM

Fer on-chip with 20 µM ALF, the labeled Fer was eluted in 90% ACN into the separation module and separated as shown in Figure 6.13C, resulting in a relatively narrow peak for the on-chip labeled Fer. The shorter incubation time (25 min) compared to off-chip labeling (24 h) possibly resulted in labeling of fewer amine groups on Fer (see Chapter 4.4) which led to a narrower peak. The small co-eluting peak could be one of the Fer isoforms formed during labeling. Moreover, peak tailing was caused by protein adsorption and could be reduced by increasing the HPC concentration in the µCE buffer. Additionally, detection was done 3 mm from the injector, and a band eluted in 90% ACN was injected, both of which can also result in narrower peaks. This study is the first demonstration of integrating pressure-loaded on-chip SPE, fluorescence labeling, elution, and electrophoretic separation on a single microfluidic-based platform.
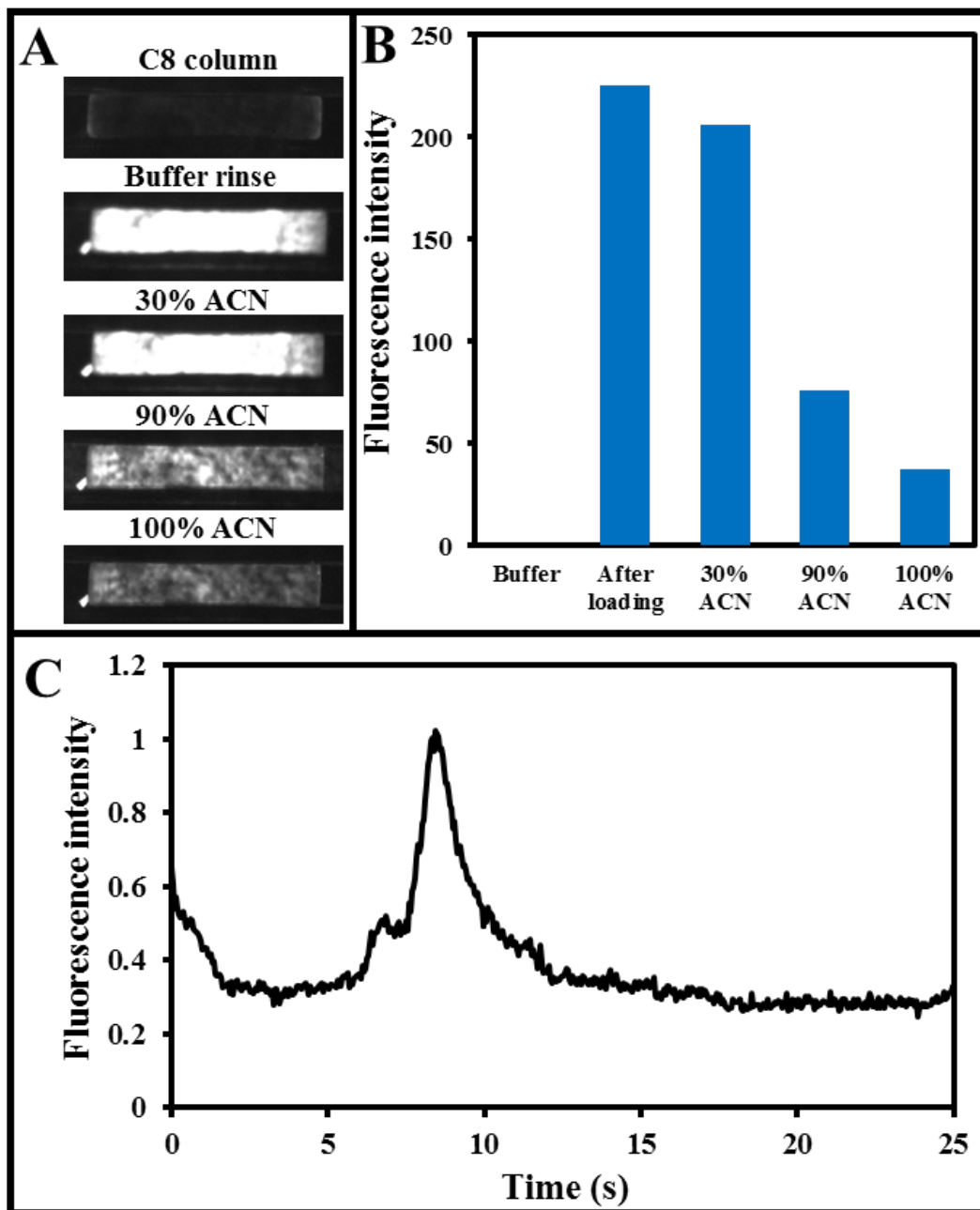
Figure 6.13 On-chip retention, labeling, elution and electrophoretic separation of 1 µM Fer in an integrated device. (A) C8 monolith fluorescence images during different steps of on-chip labeling and elution. (B) C8 monolith background-subtracted fluorescence measurements during on-chip labeling and elution. (C) Electropherogram of on-chip labeled Fer eluted from the monolith in 90% ACN, captured in the injection intersection and then separated.

6.5 REFERENCES

1.   Carasek, E.; Merib, J., Membrane-based microextraction techniques in analytical chemistry: A review. *Anal. Chim. Acta* **2015**, *880*, 8-25.

2.   Nollet, L. M. L.; Toldra, F., *Handbook of Food Analysis*. 3rd ed.; CRC Press: **2015**; p 74-75.

3.   Vas, G.; Vékey, K., Solid-phase microextraction: a powerful sample preparation tool prior to mass spectrometric analysis. *J. Mass Spectrom.* **2004,** *39*, 233-254.

4.   Pawliszyn, J., Sample Preparation: Quo Vadis? *Anal. Chem.* **2003,** *75*, 2543-2558.

5.   Ulrich, S., Solid-phase microextraction in biomedical analysis. *J. Chromatogr. A* **2000,** *902*, 167-194.

6.   Majors, R., Sample Preparation Fundamentals for Chromatography. Agilent Technologies, Mississauga, ON, Canada: **2013**.

7.   Nováková, L.; Vlčková, H., A review of current trends and advances in modern bio-analytical methods: Chromatography and sample preparation. *Anal. Chim. Acta* **2009,** *656*, 8-35.

8.   Paegel, B. M.; Blazej, R. G.; Mathies, R. A., Microfluidic devices for DNA sequencing: sample preparation and electrophoretic analysis. *Curr. Opin. Biotechnol.* **2003,** *14*, 42-50.

9.   Whitesides, G. M., The origins and the future of microfluidics. *Nature* **2006,** *442*, 368-373.

10.   Thorsen, T.; Maerkl, S. J.; Quake, S. R., Microfluidic large-scale integration. *Science* **2002,** *298*, 580-584.

11.   Boyaci, E.; Rodríguez-Lafuente, Á.; Gorynski, K.; Mirnaghi, F.; Souza-Silva, É. A.; Hein, D.; Pawliszyn, J., Sample preparation with solid phase microextraction and exhaustive extraction approaches: Comparison for challenging cases. *Anal. Chim. Acta* **2015,** *873*, 14-30.

12. Juhascik, M. P.; Jenkins, A. J., Comparison of liquid/liquid and solid-phase extraction for alkaline drugs. *J. Chromatogr. Sci.* **2009,** *47*, 553-557.

13. Hennion, M.-C., Solid-phase extraction: method development, sorbents, and coupling with liquid chromatography. *J. Chromatogr. A* **1999,** *856*, 3-54.

14. Yu, C.; Davey, M. H.; Svec, F.; Fréchet, J. M. J., Monolithic Porous Polymer for On-Chip Solid-Phase Extraction and Preconcentration Prepared by Photoinitiated in Situ Polymerization within a Microfluidic Device. *Anal. Chem.* **2001,** *73*, 5088-5096.

15. Ramsey, J. D.; Collins, G. E., Integrated Microfluidic Device for Solid-Phase Extraction Coupled to Micellar Electrokinetic Chromatography Separation. *Anal. Chem.* **2005,** *77*, 6664-6670.

16. Foote, R. S.; Khandurina, J.; Jacobson, S. C.; Ramsey, J. M., Preconcentration of proteins on microfluidic devices using porous silica membranes. *Anal. Chem.* **2005,** *77*, 57-63.

17. Long, Z.; Shen, Z.; Wu, D.; Qin, J.; Lin, B., Integrated multilayer microfluidic device with a nanoporous membrane interconnect for online coupling of solid-phase extraction to microchip electrophoresis. *Lab Chip* **2007,** *7*, 1819-1824.

18. Kang, Q. S.; Li, Y.; Xu, J. Q.; Su, L. J.; Li, Y. T.; Huang, W. H., Polymer monolith-integrated multilayer poly (dimethylsiloxane) microchip for online microextraction and capillary electrophoresis. *Electrophoresis* **2010,** *31*, 3028-3034.

19. Weigl, B. H.; Bardell, R. L.; Cabrera, C. R., Lab-on-a-chip for drug development. *Adv. Drug Deliver. Rev.* **2003,** *55*, 349-377.

20. Zhang, L.; Yin, X.; Fang, Z., Negative pressure pinched sample injection for microchip-based electrophoresis. *Lab Chip* **2006,** *6*, 258-264.

21.   Fiorini, G. S.; Chiu, D. T., Disposable microfluidic devices: fabrication, function, and application. *Biotechniques* **2005,** *38*, 429-446.

22.   Panchuk-Voloshina, N.; Haugland, R. P.; Bishop-Stewart, J.; Bhalgat, M. K.; Millard, P. J.; Mao, F.; Leung, W.-Y.; Haugland, R. P., Alexa dyes, a series of new fluorescent dyes that yield exceptionally bright, photostable conjugates. *J. Histochem. Cytochem.* **1999,** *47*, 1179-1188.

7. CONCLUSIONS AND FUTURE WORK

7.1 CONCLUSIONS

7.1.1 Thin-film microfabricated nanofluidic arrays for size-selective protein fractionation

A nanosieving system was developed and tested for size-selective protein fractionation. I modified previous fabrication procedures to make devices more reproducibly and with channel heights down to 15 nm. These improvements enabled me to study the effects of protein size and concentration on distribution between a height step and the nanochannel exit. The protein distribution at a nanoscale opening depended on protein diameter and opening size: as the protein diameter increased from 3.5 to 17 nm for devices having the same height step, an increase in the trapped/total (T/t) ratio was obtained, until height steps were much larger than the protein diameter. For some proteins, the highest concentrations led to an increase in the T/t ratio relative to lower concentrations. I also helped in developing a model, predicting the trapping behavior of rigid spherical particles at height steps, which provided good correlation with my experimental data. Moreover, I demonstrated that changes in buffer ionic strength altered the protein trapping behavior, because of changes in the electric double layer thickness. This effect could be further explored to tune the effective opening size of fixed height step nanochannels for size-dependent trapping of different size molecules. These results lay the experimental and theoretical foundation for separating proteins of different sizes in nanosieving systems.

7.1.2 Increasing protein signal using heat-treated thin-film microfabricated nanochannels

In Chapter 3, a heat-treatment method was developed to reduce protein interactions with SiO_2 and Ta_2O_5 surfaces. Decreased surface interactions resulted in improved signal from hemoglobin and catalase at the exits of 100-nm-tall SiO_2 and Ta_2O_5 nanochannels. Ta_2O_5

nanochannels showed a more consistent and greater increase in protein signal after heat treatment compared to SiO_2 channels. As existing methods to reduce non-specific protein adsorption are problematic with nanochannels, this method can support the development of nanofluidic-based systems for protein analysis. This work could also be extended to other nanochannel materials such as Al_2O_3 and Si_3N_4 to explore heat treatment effects on protein signal in these systems.

7.1.3 Assessment of off-chip fluorescent labeling of preterm birth biomarkers and separation using capillary and microchip electrophoresis

A fluorescent dye labeling procedure was developed for preterm birth (PTB) peptide biomarkers, and labeling was assessed using conventional capillary electrophoresis. An improvement in labeling was observed on denaturing the peptides and using heat to increase reaction kinetics. Experiments with ferritin (Fer) showed Alexa Fluor 488 5-tetrafluorophenyl ester (ALF) is a better label than fluorescein isothiocyanate (FITC). However, labeling for longer reaction times broadened the Fer peak in microchip electropherograms. Mixtures of PTB biomarkers were also separated in a polymethylmethacrylate device. FITC-labeled peptide 2 and 3 showed similar migration times in microchip electrophoresis (µCE), but several options are available to change their migration times and improve the separation. Overall, this study is useful for the on-chip labeling and separation of PTB biomarkers in an integrated device.

7.1.4 Design and fabrication of an integrated pump and valve solid-phase extraction and microchip electrophoresis system

A fabrication process was developed to make multiple-layer solid-phase extraction (SPE) and µCE devices. On-chip pneumatic valves and a peristaltic pump were formed in an elastomeric material to enable pressure-actuated sample manipulation. Furthermore, SPE and µCE were

integrated on a single microchip device to enable automation. In the integrated design, the thermoplastic layer thickness and hole diameter were reduced to decrease dead volume.

7.1.5 Evaluation of an integrated microfluidic solid-phase extraction and separation module

In Chapter 6, the successful integration of SPE, fluorescence labeling, elution and μCE in pressure-controlled integrated microdevice was demonstrated. Fluidic and control channel dimensions were optimized to actuate valves with <35 psi and produce reasonable flow rates. Both three- and five-valve pumps were evaluated, and better flow rates were obtained with five-valve pumps. Studies of retention/elution of Fer and dyes established that ALF is a better option for on-chip labeling of Fer because the dye is mostly eluted with an aqueous buffer rinse. A five-valve pump eluted Fer from a C8 monolith in a narrower peak compared to a three-valve pump. Fer was enriched 80-fold on a C8 monolith in an integrated device, and showed 70-fold enrichment in μCE. On the other hand, peptides were enriched only 3-10 fold, much less than Fer, due to their lower hydrophobicity. Fer labeling with FITC and ALF was tested; a significant amount of FITC was retained on the column, which could hinder the use of high FITC-to-protein ratios. On the other hand, much less ALF was retained on the monolith even at higher ALF concentrations. Finally, successful demonstration of an integrated device was accomplished for on-chip retention, labeling, elution, and separation of a PTB biomarker (Fer). Overall, this study lays the foundation for devices integrating SPE, fluorescence labeling, elution and μCE for PTB biomarker analysis.

7.2 FUTURE WORK

7.2.1 Automation of an integrated microfluidic SPE and μCE module

In Chapters 5-6, I showed the fabrication and operation of an integrated SPE and μCE device. However, device operation was not fully automated because it required manual

replacement of all solutions in a single inlet reservoir. Figure 7.1 shows proposed designs of an integrated system that can be tested for automated device operation. There are five essential solutions required to perform SPE and fluorescent labeling on a chip: analyte, dye, rinsing buffer, dye eluent, and labeled analyte eluent. Therefore, five inlet reservoirs are needed to automate the process. Figure 7.1A shows a device design in which five inlet channels merge into a fluidic channel at a single point. My initial SPE design in Figure 6.1A had a problem with bubble formation at the channel junction during operation, perhaps due to the convergence of several channels at one point. Therefore, I propose an alternative design in Figure 7.1B, in which the inlet channels do not meet at a single point, but merge into a fluidic channel with a small (50 µm) distance between connection points.
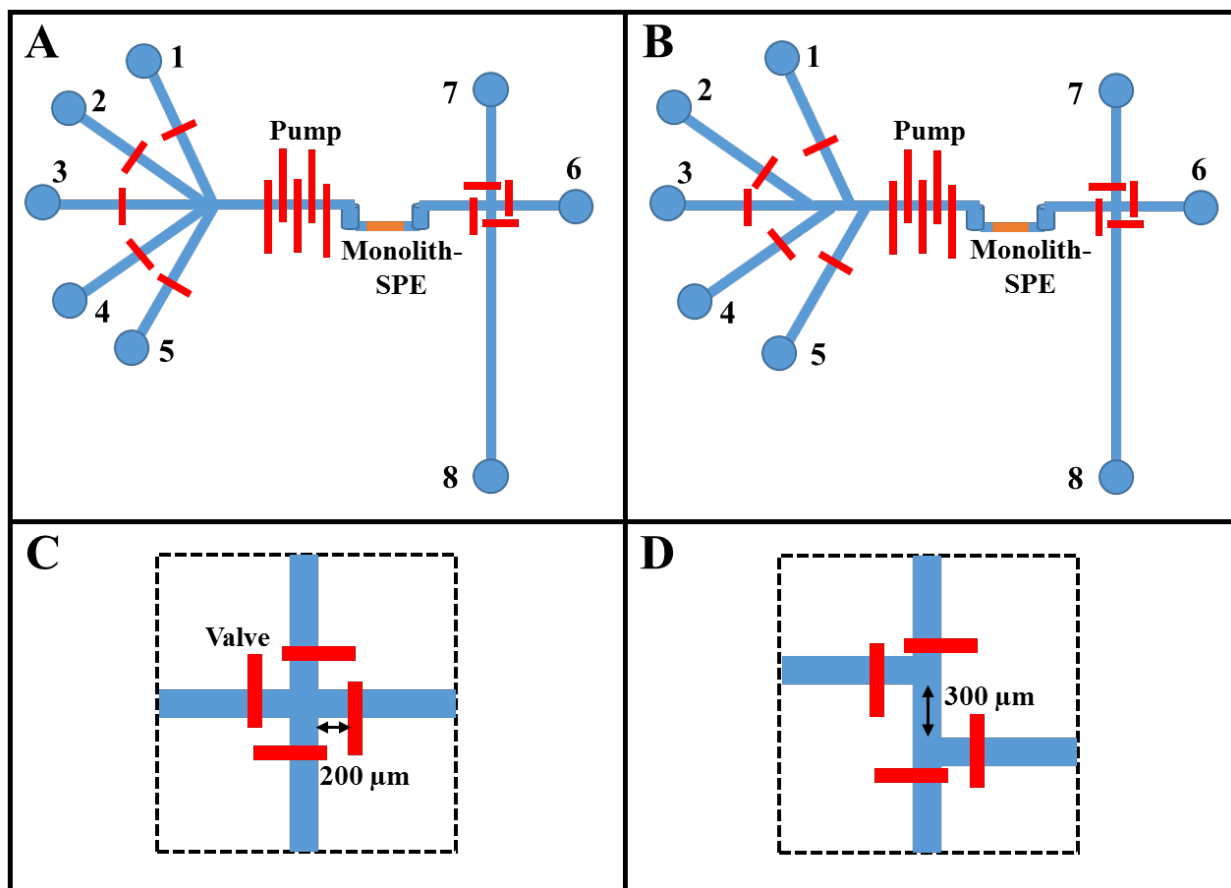
Figure 7.1 Designs for automation of an integrated SPE and μCE device. (A) Five pneumatically valved channels converging at a common point in a fluidic channel. (B) Four pneumatically valved channels merging into a single channel with a 50-μm distance between merging points. (C) Simple-cross injection intersection with 200-μm valve spacing. (D) Double-T injection intersection with 300-μm offset. Reservoirs are, 1: labeled analyte eluent, 2: dye eluent, 3: rinsing buffer, 4: sample, 5: dye, 6: sample waste, 7: running buffer, and 8: separation waste.

In a pressure-actuated integrated device, the intersection geometry and valve spacing govern the efficient loading of sample. There are two different intersection designs that can be tested to capture the sample plug. My colleague used a simple-cross geometry (shown in Figure 7.1C) and found that a 200-μm valve distance from the intersection produced the best μCE signal for peptide separations in pressure-driven devices.[1] However, in that study, a continuous source of

155

sample was available and long injection times (>30 s) were possible, which affected the plug volume injected into the separation channel for different valve spacings. In an integrated SPE device, only a limited volume of sample (~25 nL) is eluted from the monolith, with a ~7 mm width. Such a small sample cannot be injected for >15 s, and with a simple-cross configuration and 300 μm valve spacing (~4 nL), the entire eluted band cannot be captured unless it has less than ~500 μm width. The sample band could be narrowed by reducing dead volumes and using 100% ACN to elute the labeled sample. In addition, a double-T intersection (Figure 7.1D) could be used to capture more of the eluted sample band by adjusting the offset length to match the eluted band length. The use of a double-T intersection geometry could lower the separation efficiency because a longer sample plug would be injected. However, the presence of eluting solvent in the injected sample should cause sample stacking as shown in Chapter 6.4, which could compensate for the loss in efficiency due to the injected plug length.

7.2.2 Automation of an integrated immunoaffinity and μCE module

Similar to the integrated SPE and μCE platform, a microdevice can be fabricated integrating immunoaffinity extraction and μCE. Optimal device design parameters from Figure 7.1 can be adapted for automated operation, although for this description, I refer to a device design similar to Figure 7.1A. Figure 7.2 shows an integrated immunoaffinity extraction and μCE device design with multiple inlet channels to flow different solutions for automated operation. In a previous study, retained sample was eluted at low pH (2-3),[2] which can cause quenching of some fluorescent dyes. Therefore, to raise the pH of sample eluting from the monolith, I have designed an intersecting channel after the monolith, as shown in Figure 7.2. Using a three-valve peristaltic pump, a basic solution can flow into the fluidic channel with the eluting sample and raise the pH to restore fluorescence. This will facilitate fluorescence imaging, which is especially useful in

troubleshooting and optimizing device operation. Sample pH neutralization should not be needed in the final integrated device that combines immunoaffinity extraction with SPE and µCE because the eluted sample plug will be captured in the SPE module and eluted in a more neutral pH buffer.
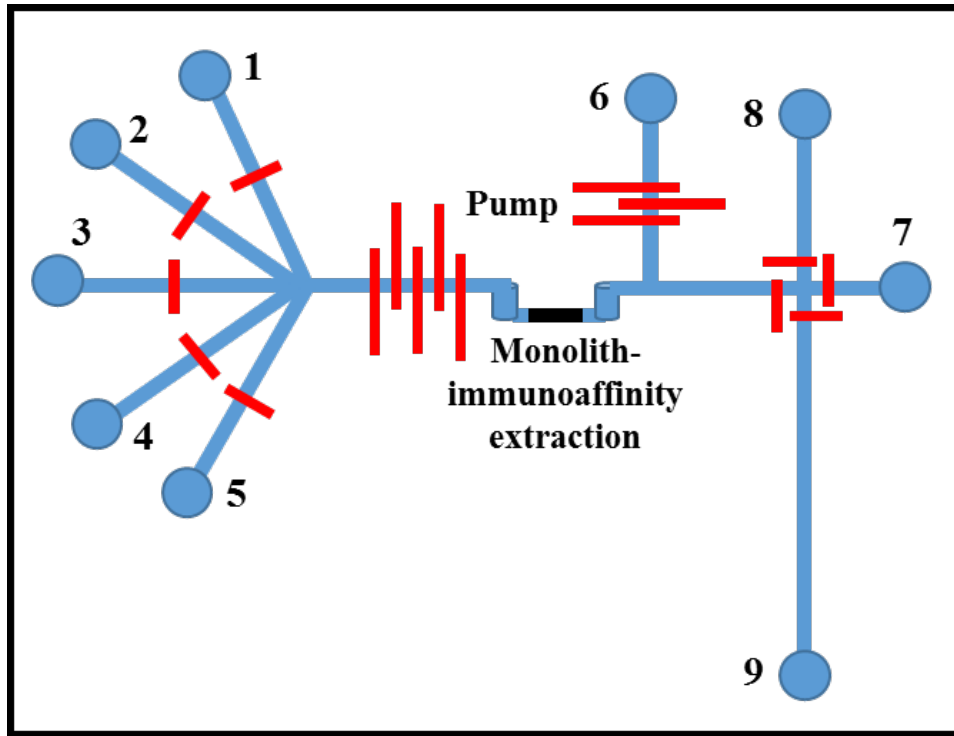

Figure 7.2 Immunoaffinity extraction module coupled with µCE. Reservoirs are, 1: antibody, 2: sample, 3: wash buffer, 4: eluent, 5: blocking buffer, 6: titration solution, 7: sample waste, 8: running buffer, and 9: separation waste.

7.2.3 Integrated device for PTB biomarker analysis

Once the design, fabrication and operation of the integrated devices in Figure 7.1 and 7.2 are optimized, all three modules (immunoaffinity extraction, SPE, and µCE) will be integrated on a single platform, as shown in Figure 7.3. The final integrated device should be able to take a raw clinical sample in and provide PTB biomarker concentrations as the output. PTB biomarkers retained and purified in the immunoaffinity extraction module will be eluted and captured in the

SPE module, where those molecules will be labeled, eluted, and separated as described in Chapter 6.3.6. Signal from peaks in the µCE separation will be used to determine the concentrations of PTB biomarkers in serum samples, which will help in predicting the risk for a PTB. This early diagnosis should help in initiating therapeutic interventions to delay delivery.
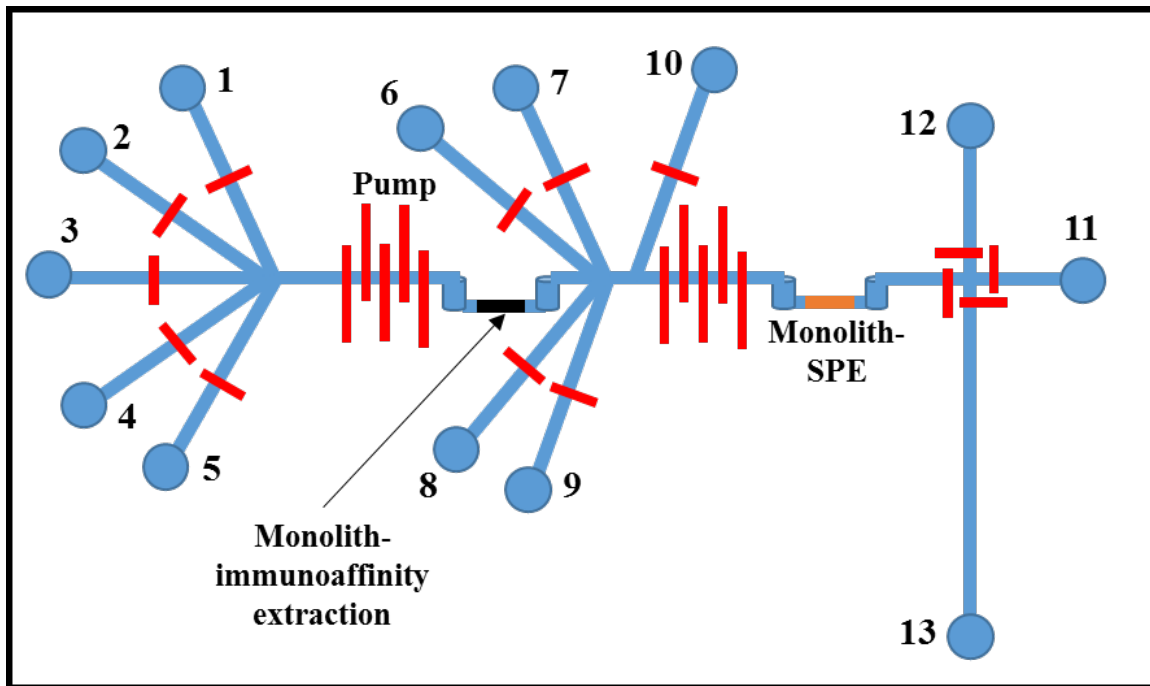

Figure 7.3 Schematic showing integration of immunoaffinity extraction, SPE, and µCE modules on a single microfluidic platform. Reservoirs are, 1: antibody, 2: sample, 3: wash buffer, 4: eluent, 5: blocking buffer, 6: labeled sample eluent, 7: dye eluent, 8: rinsing buffer, 9: dye, 10: immunoaffinity waste, 11: sample waste, 12: running buffer, and 13: separation waste.

The integrated system described offers a platform for rapid and sensitive analysis of PTB biomarkers, which should help in the diagnosis of PTB weeks before contractions begin. The application of this system is not limited to only PTB biomarkers, but can also be extended to analyze for many important clinical cancer or other disease biomarkers. Such an integrated system

would be a significant development in analytical chemistry, truly demonstrating a micro total analysis system.

7.3 REFERENCES

1.   Sahore, V.; Kumar, S.; Rogers, C. I.; Jensen, J.; Sonker, M.; Woolley, A. T., Pressure-Actuated Microfluidic Devices for Electrophoretic Separation of Pre-Term Birth Biomarkers (in preparation). *Anal. Bioanal. Chem.* **2015**.

2.   Yang, W.; Yu, M.; Sun, X.; Woolley, A. T., Microdevices integrating affinity columns and capillary electrophoresis for multibiomarker analysis in human serum. *Lab Chip* **2010,** *10*, 2527-2533.